

Electronic Supplementary Information for

Dye-Sensitized Solar Cells based on Fe *N*-heterocyclic Carbene Photosensitizers with Improved Rod-like Push-Pull Functionality

Linnea Lindh^{1,2†}, Olga Gordivska^{3†}, Samuel Persson^{3†}, Hannes Michaels^{4,5†}, Hao Fan³, Pavel Chábera¹, Nils W. Rosemann^{1,3}, Arvind Kumar Gupta³, Iacopo Benesperi^{3,5}, Jens Uhlig¹, Om Prakash³, Esmail Sheibani³, Kasper S. Kjaer¹, Gerrit Boschloo⁴, Arkady Yartsev¹, Marina Freitag^{5,4*}, Reiner Lomoth^{4*}, Petter Persson^{2*}, Kenneth Wärnmark^{3*}.

¹ Department of Chemical Physics, Lund University, Box 124, SE-22100 Lund, Sweden

² Theoretical Chemistry Department, Chemistry Department, Lund University, Box 124, SE-22100 Lund, Sweden

³ Centre for Analysis and Synthesis, Department of Chemistry, Lund University, Box 124, SE-22100 Lund, Sweden

⁴ Department of Chemistry – Angstrom Laboratory, Uppsala University, Box 523, SE-75120 Uppsala, Sweden

⁵ School of Natural and Environmental Science, Bedson Building, Newcastle University, NE1 7RU Newcastle upon Tyne, UK

†These authors contributed equally to this work

*Corresponding authors

Table of Contents

1. Synthesis and Structure Identification.....	2
2. X-ray Diffraction Crystallography	25
3. Steady-State Absorption Spectroscopy	40
4. Electrochemistry and Spectroelectrochemistry	41
5. Quantum Chemical Calculations.....	44
6. fs-Transient Absorption Spectroscopy	47
7. ns-Transient Absorption Spectroscopy	52
8. Half-Cell Fabrication.....	54
9. Solar Cell Fabrication.....	55
10. Solar Cell Characterisation.....	55
References	57

1. Synthesis and Structure Identification

General

All commercial reagents and solvents were used as received, unless otherwise stated. 4-Amino-2,6-dibromopyridine was purchased from Apollo Scientific. K_2CO_3 , *n*-BuOH and HCl (aq) was purchased from Sigma-Aldrich. 4-Bromotoluene and 4-bromoanisole were purchased from Acros Organics. CuI, NaOt-Bu, $Pd_2(dba)_3$, 2-dicyclohexylphosphino-2',4',6'-triisopropylbiphenyl, 2-(dicyclohexylphosphino)biphenyl, tetrabutylammonium bromide (TBAB), NH_4PF_6 and KPF_6 were purchased from Sigma-Aldrich and stored in desiccators. Imidazole and L-proline were purchased from Acros Organics and stored in desiccator. KOt-Bu (THF solution) was purchased from Sigma-Aldrich in septa-fitted bottles and stored in refrigerator. Methyl triflate was purchased from AlphaAeser, stored under Argon in a septa-fitted bottle, in refrigerator. Anhydrous iron(II) bromide was purchased from Sigma-Aldrich and stored and weighed under argon in a glovebox. Dry toluene was collected from dry solvent dispenser (MBRAUN SPS-800) and stored over activated 3 Å MS. Dry DMF, dry DMSO and dry acetone were purchased in septa-fitted bottles from Acros Organics. Dry 1,2-dichloroethane was purchased in septa-fitted bottles from Sigma-Aldrich. 1,1'-(4-carboxypyridine-2,6-diyl)bis(3-methylimidazolium) hexafluorophosphate ($[cpbmiH_2](PF_6)_2$) was synthesized according to literature procedure.^[S1] Reactions run at room temperature (rt) are in the range of 20-23 °C. Metal heating mantels were used to achieve required reaction temperatures. Flash column chromatography (\varnothing x h) was carried out on silica gel (60 Å, 230-400 mesh, purchased from Sigma-Aldrich) or acidic alumina gel (activated, acidic, Brockmann I, purchased from Sigma-Aldrich), using reagent-grade eluents. Analytical thin-layer chromatography (TLC) was carried out on TLC Silica gel 60 F254 and visualized with a UV-lamp (254 nm). 1H NMR and ^{13}C NMR spectra were recorded at rt on a Bruker Avance II spectrometer at 400.1 MHz and 100.6 MHz, respectively. The spectra were recorded in $CDCl_3$, $DMSO-d_6$ or CD_3CN and the residual solvent signals (7.26/77.16; 2.50/39.52; 1.94/118.26 ppm, respectively) were used as reference. Chemical shifts (δ) are expressed in parts per million (ppm) and coupling constants (J) are reported in Hertz (Hz). The following abbreviations are used to indicate apparent multiplicities: s, singlet; br, broad; d, doublet; dd, doublet of doublets; dq, doublet of quartets; t, triplet; td, triplet of doublets, q, quartet, m, multiplet. Melting points were measured using a Stuart melting point apparatus SMP3 and were corrected against 3,5-dinitrobenzoic acid (mp 205 °C^[S2]). IR transmittance spectra were recorded on a Bruker-ALPHA II FT-IR Spectrometer and reported in cm^{-1} with the following abbreviations used to report relative signal strength: w, weak; m, medium; s, strong; vw, very weak; vs, very strong; and br, broad. High resolution mass spectroscopy was carried out using a Waters - XEVO-G2 QTOF spectrometer employing electrospray ionization and run in positive mode. Elemental analyses were performed by A. Kolbe, Mikroanalytisches Laboratorium, Germany.

4-Amino-2,6-di(imidazol-1-yl)pyridine (2). 4-Amino-2,6-dibromopyridine (**1**) (2.50 g, 9.92 mmol), imidazole (2.06 g, 30.3 mmol), L-proline (0.23 g, 2.0 mmol), CuI (0.38 g, 2.0 mmol), and K_2CO_3 (6.93 g, 50.1 mmol) were suspended in DMSO (12.5 mL) under N_2 . The resulting mixture was heated at 140 °C and left stirring for 48 h. After cooling to rt, the resulting mixture was diluted with water (250 mL). The resulting reaction mixture was extracted with EtOAc:*n*-BuOH (9:1) (4 x 250 mL). The combined organic phases were washed with brine (3 x 600 mL) and evaporated to dryness *in vacuo*. The resulting off-white solid was collected on a glass filter (#4) and washed with water (3 x 5 mL), yielding **2** (1.30 g, 58%) as an off-white solid after drying at rt *in vacuo*. R_f = 0.28 (CH_2Cl_2 : CH_3OH (9:1)); Mp: 211 °C dec; 1H NMR (400.1 MHz, $DMSO-d_6$): δ = 8.51 (apparent t, J = 1.2 Hz, 2H, Im-H2), 7.85 (apparent t, J = 1.4 Hz, 2H, Im-H5), 7.10 (apparent t, J = 1.2 Hz, 2H, Im-H4), 6.71 (s, 2H, -NH₂), 6.68 (s, 2H, Py-H3) ppm; ^{13}C NMR (100.6 MHz, $DMSO-d_6$): δ = 159.2, 148.5, 135.2, 129.9, 116.7, 94.4 ppm; HRMS-ESI: m/z $[M+H]^+$ calcd for $C_{11}H_{11}N_6$: 227.1045; found 227.1042; Anal. Calcd for $C_{11}H_{10}N_6$: C 58.40, H 4.46, N 37.15. Found: C 58.52, H 4.49, N 36.92.

2,6-Di(imidazol-1-yl)-4-(di-*p*-tolylamino)pyridine (3). 4-Amino-2,6-di(imidazol-1-yl)pyridine (**2**) (51 mg, 0.23 mmol), fresh NaOt-Bu (65 mg, 0.68 mmol), Pd₂(dba)₃ (11 mg, 0.012 mmol) and 4-bromotoluene (158 mg, 0.925 mmol) were dissolved in dry, degassed toluene (4 mL) under N₂. 2-Dicyclohexylphosphino-2',4',6'-triisopropylbiphenyl (21 mg, 0.044 mmol) dissolved in dry, degassed toluene (1 mL), was added dropwise to the solution over 1 min and the resulting mixture was refluxed under stirring for 5 days. After cooling to rt, the reaction mixture was filtered on a glass filter (#3), washed with several portions of toluene and the filtrate was evaporated to dryness *in vacuo*. The resulting brown solid was purified by silica gel chromatography (2.5 x 25 cm, CH₂Cl₂:CH₃OH (95:5)), yielding **3** (25 mg, 28%) as an off-white solid. *R*_f = 0.45 (CH₂Cl₂:CH₃OH (94:6)); Mp: 238-240 °C; ¹H NMR (400.1 MHz, DMSO-*d*₆): δ = 8.48 (s, 2H, Im-H2), 7.77 (s, 2H, Im-H5), 7.30-7.23(m, 4H, Tol-H3), 7.23-7.17(m, 4H, Tol-H2), 7.05 (s, 2H, Im-H4), 6.67 (s, 2H, Py-H3), 2.33 (s, 6H, Ph-CH₃) ppm; ¹³C NMR (100.6 MHz, DMSO-*d*₆) δ 158.3, 148.6, 141.7, 135.9, 135.5, 130.7, 130.0, 126.7, 116.9, 97.2, 20.6 ppm; HRMS-ESI: m/z [M+H]⁺ calcd for C₂₅H₂₃N₆: 407.1979; found 407.1986; Anal. Calcd for C₁₁H₁₀N₆ · 0.2 H₂O: C 73.22, H 5.51, N 20.49. Found: C 73.20, H 5.46, N 20.51.

2,6-Di(imidazol-1-yl)-4-(di-*p*-anisylamino)pyridine (4). 4-Amino-2,6-di(imidazol-1-yl)pyridine (**2**) (934 mg, 4.13 mmol), fresh NaOt-Bu (1192 mg, 12.40 mmol), Pd₂(dba)₃ (190 mg, 0.207 mmol) and 2-(dicyclohexylphosphino)biphenyl (145 mg, 0.414 mmol) were dissolved in dry, degassed toluene (225 mL) under N₂. 4-Bromoanisole (2.1 mL, 17 mmol) was added to the reaction mixture. The resulting mixture was refluxed under stirring for 5 days. After cooling to rt, the reaction mixture was filtered on a glass filter (#3), washed with several portions of toluene and the filtrate was evaporated to dryness *in vacuo*. The resulting brown solid was purified by silica gel chromatography (3.5 x 25 cm, CH₂Cl₂:CH₃OH (97:3 → 90:10)), yielding **4** (495 mg, 27%) as an off-white solid. *R*_f = 0.39 (CH₂Cl₂:CH₃OH (94:6)); Mp: 221-222 °C; ¹H NMR (400.1 MHz, CDCl₃): δ = 8.17 (apparent t, *J*=1.1, 2H, Im-H2), 7.44 (apparent t, *J*=1.4, 2H, Im-H5), 7.24-7.17 (m, 4H, anisyl-H2), 7.13 (apparent dd, *J*=1.5, 0.9 Hz, 2H, Im-H4), 6.93-7.00 (m, 4H, anisyl-H3), 6.46 (s, 2H, Py-H3), 3.85 (s, 6H, Ph-O-CH₃) ppm; ¹³C NMR (100.6 MHz, CDCl₃): δ = 159.0, 158.5, 149.3, 136.9, 135.2, 130.6, 128.5, 116.4, 115.6, 96.4, 55.7 ppm; HRMS-ESI: m/z [M+H]⁺ calcd for C₂₅H₂₃N₆O₂: 439.1877; found 439.1880; Anal. Calcd for C₂₅H₂₂N₆O₂ · 0.8 H₂O: C 66.30, H 5.25, N 18.56. Found: C 66.34, H 5.04, N 18.34.

1,1'-(4-(Di-*p*-tolylamino)pyridine-2,6-diyl)bis(3-methylimidazolium) bis(hexafluorophosphate) ([dtapbmiH₂](PF₆)₂). 2,6-Di(imidazol-1-yl)-4-(di-*p*-tolylamino)pyridine (**3**) (72 mg, 0.18 mmol) was suspended in dry 1,2-dichloroethane (8.5 mL) in a pressure vessel under argon and the resulting mixture was cooled to 0 °C. To the mixture was added methyl triflate (0.12 mL, 1.1 mmol) dropwise over 5 min and the vessel was sealed with a screwcap. The resulting mixture was heated to 95 °C under stirring for 17 h. After cooling to rt, the reaction mixture was evaporated to dryness *in vacuo* and the residue was dissolved in dry acetone (3 mL). To the resulting solution was added TBAB (300 mg, 2 mmol). The resulting precipitate was collected on a glass filter (#4). The precipitate was dissolved in water (10 mL) and to the resulting solution was added NH₄PF₆ (400 mg, 2 mmol). The so-formed precipitate was collected on a glass filter (#3) and washed with water (3 mL) to give the product as an off-white solid. The product was dissolved in a minimum amount of acetonitrile and Et₂O was allowed to slowly diffuse into the solution to yield [dtapbmiH₂](PF₆)₂ (67 mg, 52%) as off-white needles. *R*_f = 0.42 (acetone:water:KNO₃ (sat. aq.) (40:7:1)); Mp: 213 °C dec; ¹H NMR (400.1 MHz, CD₃CN): δ = 9.34 – 9.20 (m, 2H, Im-H2), 7.93 (apparent t, *J* = 1.9 Hz, 2H, Im-H5), 7.49 (apparent t, *J* = 1.9 Hz, 2H, Im-H4), 7.36-7.31 (m, 4H, Tol-H3), 7.27-7.22 (m, 4H, Tol-H2), 6.88 (s, 2H, Py-H3), 3.93 (s, 6H, Im-CH₃), 2.39 (s, 6H, Ph-CH₃) ppm. ¹³C NMR (100.6 MHz, CD₃CN): δ = 160.5, 147.4, 141.9, 138.9, 136.2, 132.0, 127.9, 125.6, 120.3, 100.6, 37.4, 21.1 ppm. HRMS-ESI: m/z [M + PF₆]⁺ calcd for C₂₇H₂₈F₆N₆P: 581.2012; found 581.2015; Anal. Calcd for C₂₇H₂₈F₁₂N₆P₆: C 44.64, H 3.88 N 11.57. Found: C 44.80, H 3.89, N 11.43.

1,1'-(4-(Di-*p*-anisylamino)pyridine-2,6-diyl)bis(3-methylimidazolium) bis(hexafluorophosphate) ([daapbmiH₂](PF₆)₂). 2,6-Di(imidazol-1-yl)-4-(di-*p*-anisylamino)pyridine (**4**) (203 mg, 0.463 mmol) was suspended in dry 1,2-dichloroethane (20 mL) in pressure vessel under argon and the resulting mixture was cooled to 0 °C. To the mixture was added methyl triflate (0.32 mL, 2.8 mmol) dropwise

over 10 min and the vessel was sealed with a screwcap. The resulting mixture was heated to 95 °C and stirred for 21 h. After cooling to rt, the reaction mixture was evaporated to dryness *in vacuo* and the residue was dissolved in dry acetone (15 mL). To the resulting solution was added TBAB (500 mg, 3 mmol). The resulting precipitate was collected on a glass filter (#3). The precipitate was dissolved in water (15 mL) and to the resulting solution was added NH₄PF₆ (400 mg, 2 mmol). The so-formed precipitate was collected on a glass filter (#3) and washed with water (5 mL) to give the product as an off-white solid. The product was dissolved in a minimum amount of acetonitrile and Et₂O was allowed to slowly diffuse into the solution to yield crystals. The crystallization was performed twice to give **[daapbmiH₂](PF₆)₂** (124 mg, 35%) as off-white needles. *R_f* = 0.42 (acetone:water:KNO₃ (sat. aq.) (40:7:1)); Mp: 232 °C dec; ¹H NMR (400.1 MHz, CD₃CN): δ = 9.19 (apparent td, *J* = 1.5, 0.6 Hz, 2H, Im-H2), 7.95 (apparent t, *J* = 2.0 Hz, 2H, Im-H5), 7.49 (apparent t, *J* = 1.9 Hz, 2H, Im-H4), 7.37 – 7.28 (m, 4H, anisyl-H2), 7.11 – 7.02 (m, 4H, anisyl-H3), 6.82 (s, 2H, Py-H3), 3.93 (s, 6H, Im-CH₃), 3.83 (s, 6H, Ph-O-CH₃) ppm; ¹³C NMR (100.6 MHz, CD₃CN): δ = 161.2, 160.2, 147.4, 137.2, 136.2, 129.6, 125.7, 120.4, 116.8, 100.0, 56.4, 37.5 ppm; HRMS-ESI: *m/z* [M + PF₆]⁺ calcd for C₂₇H₂₈F₆N₆O₂P: 613.1910; found 613.1925; Anal. Calcd for C₂₇H₂₈F₁₂N₆O₂P₂: C 42.76, H 3.72, N 11.08. Found: C 42.61, H 3.64, N 11.13.

(1,1'-(4-Carboxypyridine-2,6-diyl)bis(3-methylimidazol-2-ylidene))(1,1'-(4-(di-*p*-tolylamino)pyridine-2,6-diyl)bis(3-methylimidazol-2-ylidene))iron(II) bis(hexafluorophosphate) ([Fe(cpbmi)(dtapbmi)](PF₆)₂). A mixture of 1,1'-(4-(di-*p*-tolylamino)pyridine-2,6-diyl)bis(3-methylimidazolium) bis(hexafluorophosphate) (**[dtapbmiH₂](PF₆)₂**) (151 mg, 0.208 mmol) and 1,1'-(4-carboxypyridine-2,6-diyl)bis(3-methylimidazolium) bis(hexafluorophosphate) (**[cpbmiH₂](PF₆)₂**) (118 mg, 0.205 mmol) was dried *in vacuo* at 80 °C for 24 h. The solid was allowed to cool to rt under N₂, suspended in dry DMF (4 mL) and cooled to 0 °C. KO*t*-Bu (THF, 1 M, 1.3 mL, 1.3 mmol) was added dropwise to the suspension at 0 °C, over 10 min. The resulting red solution was stirred for 15 min. Anhydrous FeBr₂ (45 mg, 0.21 mmol) dissolved in dry DMF (1 mL) was added dropwise to the solution at 0 °C, over 2 min. Upon complete addition, the reaction was allowed to reach rt over 1 h, under stirring. The reaction mixture was diluted with EtOAc (50 mL) and extracted with water (3 x 50 mL), at which point the aqueous phase became almost colourless. The combined red aqueous phases were acidified with HCl (aq., 6 M, 1.5 mL) to pH = 1. To the resulting aqueous solution was added KPF₆ (500 mg, 3 mmol). The so-formed red precipitate was collected on a glass filter (#4) and washed with water (3 x 5 mL) and then Et₂O (5 mL). The crude product was further purified by acidic alumina gel chromatography (3.5 x 16 cm, MeCN:H₂O (1:0 → 3:1)). The desired fractions were combined and MeCN was evaporated *in vacuo*. The resulting aqueous solution was acidified by HCl (aq., 6 M, 6 mL) to pH = 1 and to it was added KPF₆ (200 mg, 1 mmol). The resulting precipitate was collected on a glass filter (#4), carefully rinsed with ice cold water until the filtrate became slightly orange and dried *in vacuo* at 40 °C to yield **([Fe(cpbmi)(dtapbmi)](PF₆)₂)** (35 mg, 16%) as a dark red solid. *R_f* = 0.40 (acetone:water:KNO₃ (sat. aq.) (30:7:1)); Mp: >174 °C dec; ¹H NMR (400.1 MHz, CD₃CN) δ = 8.23 (s, 2H, acid-Py-H3), 8.15 (d, *J* = 2.1 Hz, 2H, acid-Im-H5), 7.70 (d, *J* = 2.1 Hz, 2H, aniline-Im-5H), 7.37 – 7.32 (m, 4H, Tol-H3), 7.32 – 7.26 (m, 4H, Tol-H2), 7.06 (d, *J* = 2.1 Hz, 2H, acid-Im-H4), 7.00 (s, 2H, aniline-Py-H3), 6.85 (d, *J* = 2.1 Hz, 2H, aniline-Im-H4), 2.78 (s, 6H, acid-Im-CH₃), 2.41 (s, 6H, Ph-CH₃), 2.39 (s, 6H, aniline-Im-CH₃) ppm; ¹³C NMR (100.6 MHz, CD₃CN) δ = 201.3, 200.9, 165.5, 158.9, 156.1, 153.6, 142.8, 138.2, 131.8, 128.1, 128.1, 127.4, 127.0, 117.4, 117.1, 104.9, 94.7, 35.7, 35.5, 21.1 ppm; IR $\tilde{\nu}_{\text{max}}$: 1724 (w), 1480.71 (w), 1263.59 (w), 1235.81 (w), 829.22 (s), 683.22 (w), 555.20 (s) cm⁻¹; HRMS-ESI: *m/z* [M + PF₆]⁺ calcd for C₄₁H₃₉F₆FeN₁₁O₂P: 918.2274; found 918.2284; Anal. Calcd for C₄₁H₃₉F₁₂FeN₁₁O₂P₂ · 1.3 H₂O: C 45.30, H 3.86, N 14.17. Found: C 45.25, H 3.81, N 14.18.

(1,1'-(4-(Di-*p*-anisylamino)pyridine-2,6-diyl)bis(3-methylimidazol-2-ylidene))(1,1'-(4-carboxypyridine-2,6-diyl)bis(3-methylimidazol-2-ylidene))iron(II) bis(hexafluorophosphate) ([Fe(cpbmi)(daapbmi)](PF₆)₂). A mixture of 1,1'-(4-(di-*p*-anisylamino)pyridine-2,6-diyl)bis(3-methylimidazolium) bis(hexafluorophosphate) (**[daapbmiH₂](PF₆)₂**) (384 mg, 0.506 mmol) and 1,1'-(4-carboxypyridine-2,6-diyl)bis(3-methylimidazolium) bis(hexafluorophosphate) (**[cpbmiH₂](PF₆)₂**) (291.3 mg, 0.5064 mmol) was dried *in vacuo* at 70°, over night. The solid was allowed to cool to rt under N₂, suspended in dry DMF (4 mL) and cooled to 0 °C. KO*t*-Bu (THF, 1 M, 3.1 mL, 3.1 mmol)

was added dropwise to the suspension at 0 °C, over 10 min. The resulting red solution was stirred for 15 min. Anhydrous FeBr₂ (110 mg, 0.51 mmol) dissolved in dry DMF (2 mL) was added dropwise to the solution at 0 °C, over 2 min. Upon complete addition, the reaction was allowed to warm to rt over 1 h, under stirring. The reaction mixture was diluted with EtOAc (100 mL) and extracted with water (3 x 100 mL), at which point the aqueous phase became almost colourless. The combined red aqueous phases were acidified with HCl (aq., 6 M, 3 mL) to pH = 1. To the resulting aqueous solution was added KPF₆ (sat. aq., 20 mL). The so-formed red precipitate was collected on a glass filter (#4) and washed with water (3 x 5 mL) and then Et₂O (5 mL). The crude product was further purified by acidic alumina gel chromatography (3.5 x 17 cm, MeCN:H₂O (1:0 → 3:1 → 1:1)). The desired fractions were combined and MeCN was evaporated *in vacuo*. The resulting aqueous solution was acidified by HCl (aq., 6 M, 12 mL) to pH = 1 and to it was added KPF₆ (sat. aq., 70 mL). The resulting precipitate was collected on a glass filter (#4), carefully rinsed with ice cold water until the filtrate became slightly orange and dried *in vacuo* at 40 °C to yield **[Fe(cpbmi)(daapbmi)](PF₆)₂** (65 mg, 11%) as a dark red solid. *R_f* = 0.36 (acetone:water:KNO₃ (sat. aq.) (30:7:1)); Mp: >163 °C dec; ¹H NMR (400.1 MHz, CD₃CN): δ = 8.22 (s, 2H, acid-Py-H3), 8.15 (d, *J* = 2.1 Hz, 2H, acid-Im-H5), 7.72 (d, *J* = 2.2 Hz, 2H, aniline-Im-H5), 7.41 - 7.34 (m, 4H, anisyl-H2), 7.11 - 7.04 (m, 6H, anisyl-H3 and acid-Im-H4), 6.91 (s, 2H, aniline-Py-H3), 6.85 (d, *J* = 2.2 Hz, 2H, aniline-Im-H4), 3.84 (s, 6H, Ph-O-CH₃), 2.77 (s, 6H, acid-Im-CH₃), 2.38 (s, 6H, aniline-Im-CH₃) ppm; ¹³C NMR (100.6 MHz, CD₃CN) δ = 201.4, 201.0, 165.4, 159.7, 159.6, 156.1, 153.5, 138.1, 138.0, 129.7, 127.4, 127.0, 117.4, 117.1, 116.5, 104.8, 93.8, 56.3, 35.7, 35.5 ppm; IR $\tilde{\nu}_{\text{max}}$: 1636.26(w), 1505.73(w), 1482.15(w), 1266.12(w), 835.43 (s), 685.55 (w), 556.40 (s) cm⁻¹; HRMS-ESI: *m/z* [M + PF₆]⁺ calcd for C₄₁H₃₉F₆FeN₁₁O₄P: 950.2172; found 950.2185; Anal. Calcd for C₄₁H₃₉F₁₂FeN₁₁O₄P₂ · 2.15 H₂O: C 43.41, H 3.85, N 13.58. Found C 43.51, H 3.47, N 13.21.

Bis(1,1'-(4-(di-*p*-tolylamino)pyridine-2,6-diyl)bis(3-methylimidazol-2-ylidene))iron(II) bis(hexafluorophosphate) ([Fe(dtapbmi)₂](PF₆)₂). 1,1'-(4-(Di-*p*-tolylamino)pyridine-2,6-diyl)bis(3-methylimidazolium) bis(hexafluorophosphate) (115 mg, 0.158 mmol) ([dtapbmiH₂](PF₆)₂) was dried *in vacuo* at 80 °C for 18 h. The solid was allowed to cool to rt under N₂, suspended in dry DMF (3.4 mL) and cooled to 0 °C. To the suspension was added KO^{*t*}-Bu (THF, 1 M, 0.4 mL, 0.4 mmol) dropwise at 0 °C, over 5 min and the reaction was stirred for 20 min. To the resulting solution, anhydrous FeBr₂ (17 mg, 0.078 mmol), dissolved in dry DMF (0.5 mL) was slowly added at 0 °C, over 1 min. The resulting mixture was stirred for 15 min at 0 °C. The reaction was allowed to warm to rt under stirring for 1 h. The reaction mixture was cooled to 0 °C and to it was added NH₄PF₆ (871 mg, 5.34 mmol, aq., 20 mL). The resulting orange precipitate was collected on a glass filter (#4) and washed with Et₂O (4 x 2.5 mL). The resulting precipitate was dissolved in MeCN (20 mL) and the resulting solution was filtered through a plug of neutral alumina (4 x 2 cm) and the plug was washed with MeCN (40 mL). The resulting filtrate was evaporated to dryness *in vacuo* and the residue was dissolved in a minimum amount of MeCN and recrystallized by slow diffusion of Et₂O. The recrystallization was repeated twice, yielding **[Fe(dtapbmi)₂](PF₆)₂** (30 mg, 31%) as orange crystals. *R_f* = 0.40 (CH₂Cl₂:CH₃OH (96:4)); Mp: >189 °C dec; ¹H NMR (400.1 MHz, CD₃CN): δ = 7.69 (d, *J* = 2.2 Hz, 4H, Im-H5), 7.35 – 7.29 (m, 8H, Tol-H3), 7.28 – 7.22 (m, 8H, Tol-H2), 6.95 (s, 4H, Py-H3), 6.91 (d, *J* = 2.2 Hz, 4H, Im-H4), 2.67 (s, 12H, Im-CH₃), 2.40 (s, 12H, Ph-CH₃) ppm; ¹³C NMR (100.6 MHz, CD₃CN) δ = 203.4, 157.8, 154.4, 143.1, 137.9, 131.8, 127.9, 126.7, 116.8, 94.6, 35.6, 21.1 ppm; HRMS-ESI: *m/z* [M + PF₆]⁺ calcd for C₅₄H₅₂F₆FeN₁₂O₄P: 1069.3429; found: 1069.3429; Anal. Calcd for C₅₄H₅₂F₁₂FeN₁₂P₂ · 0.9 H₂O: C 52.68, H 4.42, N 13.65. Found: C 52.89, H 4.45, N 13.44.

Bis(1,1'-(4-(di-*p*-anisylamino)pyridine-2,6-diyl)bis(3-methylimidazol-2-ylidene))iron(II) bis(hexafluorophosphate) ([Fe(daapbmi)₂](PF₆)₂) (method 1). 1,1'-(4-(Di-*p*-anisylamino)pyridine-2,6-diyl)bis(3-methylimidazolium) bis(hexafluorophosphate) ([daapbmiH₂](PF₆)₂) (0.190 g, 0.251 mmol) was dried *in vacuo* at 80 °C overnight. The solid was allowed to cool to rt under N₂, suspended in dry THF (5 mL) and cooled to -78 °C. To the suspension was added KO*t*-Bu (THF, 1 M, 0.55 mL, 0.55 mmol) dropwise over 10 min and the resulting reaction mixture was stirred for 30 min, at -78 °C. The cooling bath was removed and anhydrous FeBr₂ (27 mg, 0.13 mmol), dissolved in dry THF (10 mL), was added to the reaction mixture. The resulting mixture was stirred for 24 h, at rt. The reaction mixture was filtered using a plug of celite (1 x 3) and the collected solid on the celite plug was washed with MeCN (30 mL). The collected filtrate was passed through a glass filter (#4) and rinsed with MeCN (30 mL). The resulting filtrate was evaporated to dryness *in vacuo* and the resulting yellow-brown residue was dissolved in a minimum amount of MeCN and reprecipitated with diethyl ether (50 mL). The so-formed yellowish precipitate was purified by silica gel chromatography (2 x 20 cm, acetone:H₂O:KNO₃ (sat. aq.) (10:3:1)). To the desired fractions was added KPF₆ (200 mg, 1 mmol, aq., 20 mL), affording a dark yellow-brown solid. The dark yellow-brown solid was dissolved in a minimum amount of MeCN:MeNO₂ (3:1) and crystallized by slow diffusion of dry diethyl ether in the dark, to yield [Fe(daapbmi)₂](PF₆)₂ (41 mg, 30%) as dark yellow-brown crystals. *R*_f = 0.40 (CH₂Cl₂:CH₃OH (96:4)); Mp: >189 °C dec; ¹H NMR (400.1 MHz, CD₃CN): δ = 7.70 (d, *J* = 2.3 Hz, 4H, Im-H5), 7.40-7.28 (m, 8H, anisyl-H2), 7.11-7.01 (m, 8H, anisyl-H3), 6.90 (d, *J* = 2.2 Hz, 4H, Im-H4), 6.85 (s, 4H, Py-H3), 3.84 (s, 12H, Ph-O-CH₃), 2.66 (s, 12H, Im-CH₃) ppm; ¹³C NMR (100.6 MHz, CD₃CN) δ = 203.6, 159.6, 158.4, 154.3, 138.3, 129.6, 126.6, 116.8, 116.5, 93.5, 56.2, 35.6 ppm; ESI-HRMS (*m/z*): [M + PF₆]⁺ calcd for (C₅₄H₅₂F₆FeN₁₂O₄FeP)⁺, 1133.3226; found, 1133.3225; Anal. Calcd for C₅₄H₅₂F₁₂FeN₁₂O₄P₂ · 1.0 H₂O: C 50.01, H 4.20, N 12.96. Found C 49.96, H 4.09, N 12.89.

Bis(1,1'-(4-(di-*p*-anisylamino)pyridine-2,6-diyl)bis(3-methylimidazol-2-ylidene))iron(II) bis(hexafluorophosphate) ([Fe(daapbmi)₂](PF₆)₂) (method 2). 1,1'-(4-(Di-*p*-anisylamino)pyridine-2,6-diyl)bis(3-methylimidazolium) bis(hexafluorophosphate) (150 mg, 0.198 mmol) ([daapbmiH₂](PF₆)₂) was dried *in vacuo* at 80 °C for 19 h. The solid was allowed to reach rt under N₂, suspended in dry DMF (4.4 mL) and cooled to 0 °C. To the suspension was added KO*t*-Bu (THF, 1 M, 0.5 mL, 0.5 mmol) dropwise at 0 °C, over 6 min and the reaction was stirred for 30 min. To the resulting solution was anhydrous FeBr₂ (21.8 mg, 0.101 mmol), dissolved in dry DMF (0.6 mL), slowly added at 0 °C, over 1 min. The resulting mixture was stirred for 15 min at 0 °C. The reaction was allowed to warm to rt and stirred for a further 1 h. The reaction mixture was cooled to 0 °C and NH₄PF₆ (1.28 g, 7.85 mmol, aq., 30 mL) was added. The resulting orange precipitate was collected on a glass filter (#4), washed with water (3 x 10 mL) and then Et₂O (3 x 10 mL). The resulting precipitate was dissolved in MeCN (30 mL) and the resulting solution was filtered through a plug of neutral alumina (5 x 2 cm) and the plug was washed with MeCN (50 mL). The resulting filtrate was evaporated to dryness *in vacuo* and the residue was dissolved in a minimum amount of MeCN and recrystallized by slow diffusion of Et₂O. Recrystallization was repeated twice, yielding [Fe(daapbmi)₂](PF₆)₂ (66 mg, 53%) as orange crystals. *R*_f = 0.40 (CH₂Cl₂:CH₃OH (96:4)); Mp: >189 °C dec; ¹H NMR (400.1 MHz, CD₃CN): δ = 7.70 (d, *J* = 2.3 Hz, 4H, Im-H5), 7.40-7.28 (m, 8H, anisyl-H2), 7.11-7.01 (m, 8H, anisyl-H3), 6.90 (d, *J* = 2.2 Hz, 4H, Im-H4), 6.85 (s, 4H, Py-H3), 3.84 (s, 12H, Ph-O-CH₃), 2.66 (s, 12H, Im-CH₃) ppm; ¹³C NMR (100.6 MHz, CD₃CN) δ = 203.6, 159.6, 158.4, 154.3, 138.3, 129.6, 126.6, 116.8, 116.5, 93.5, 56.2, 35.6 ppm; ESI-HRMS (*m/z*): [M + PF₆]⁺ calcd for (C₅₄H₅₂F₆FeN₁₂O₄FeP)⁺, 1133.3226; found, 1133.3225; Anal. Calcd for C₅₄H₅₂F₁₂FeN₁₂O₄P₂ · 1.6 H₂O: C 49.60, H 4.25, N 12.85. Found C 49.37, H 4.01, N 12.77.

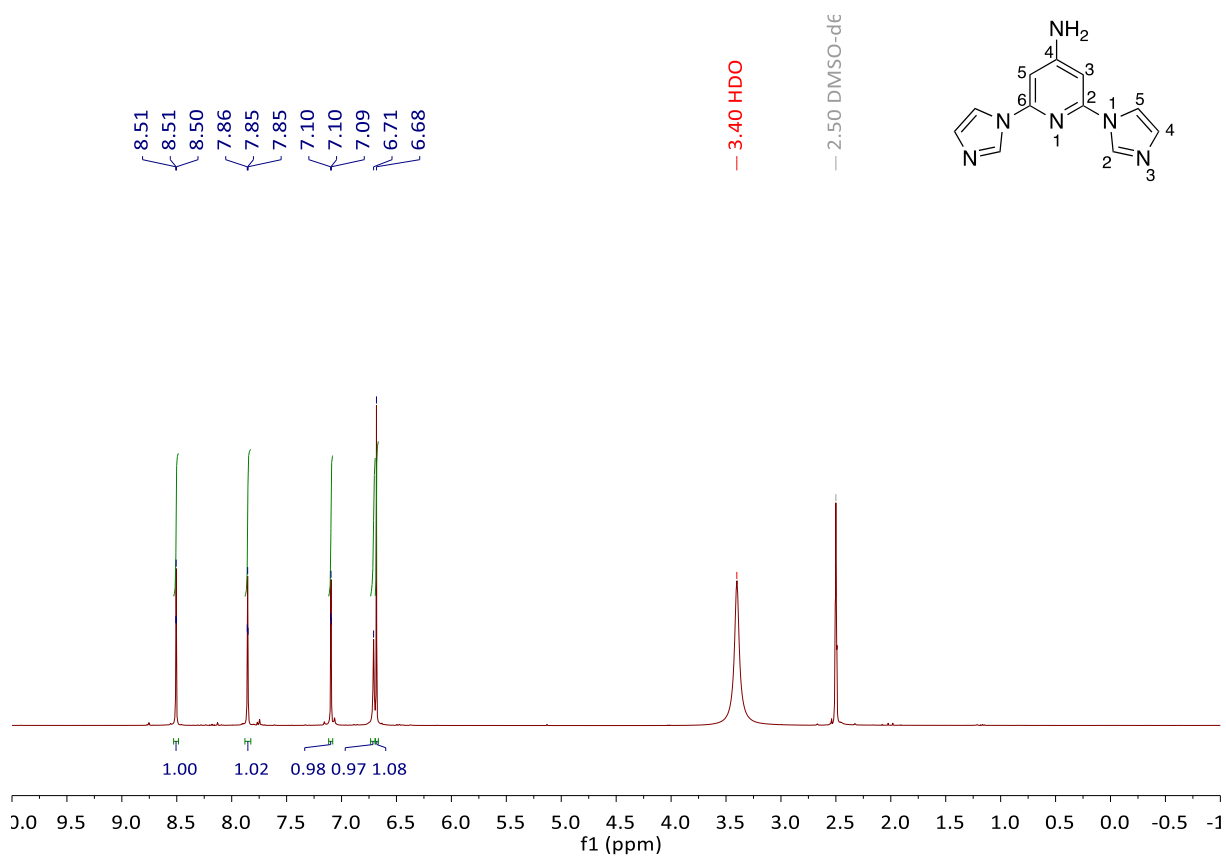


Figure S1. $^1\text{H NMR}$ (DMSO- d_6) spectrum of 4-amino-2,6-di(imidazol-1-yl)pyridine (2).

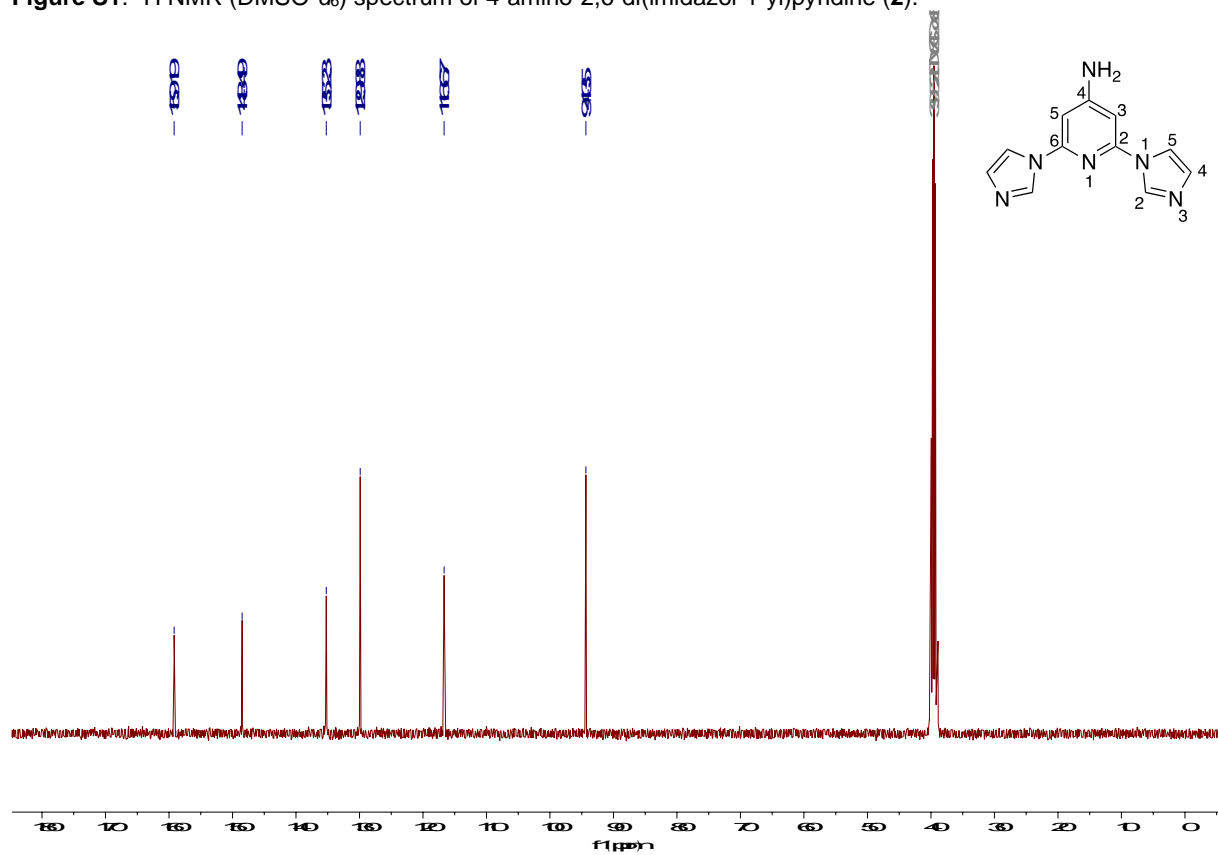


Figure S2. $^{13}\text{C NMR}$ (DMSO- d_6) spectrum of 4-amino-2,6-di(imidazol-1-yl)pyridine (2).

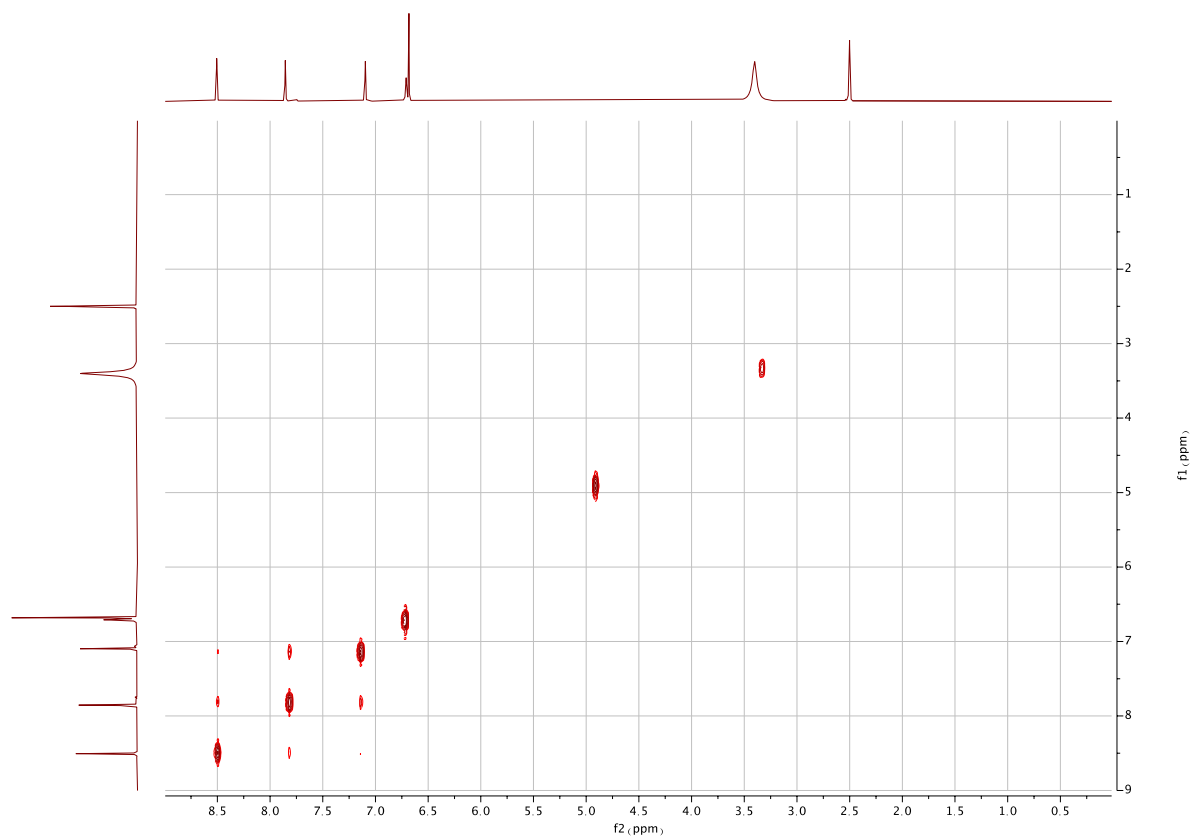


Figure S3. COSY NMR (DMSO- d_6) spectrum of 4-amino-2,6-di(imidazol-1-yl)pyridine (**2**).

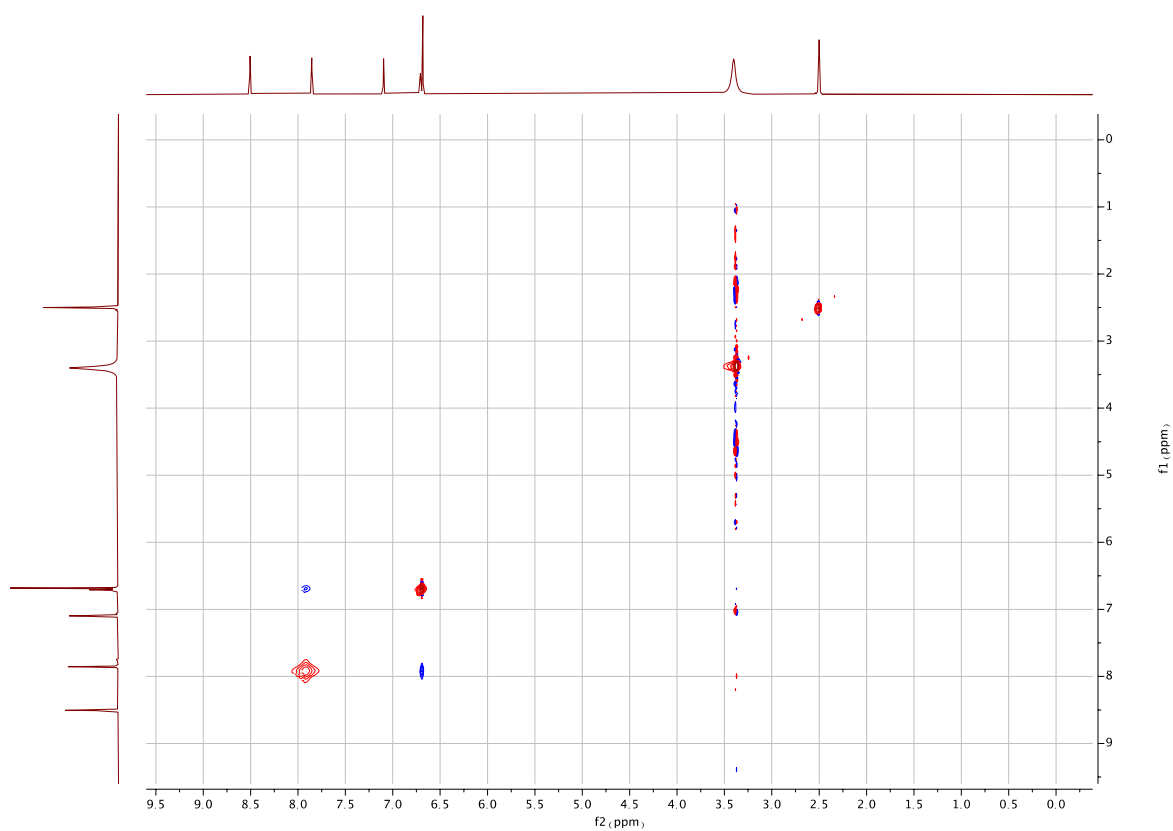


Figure S4. NOESY NMR (DMSO- d_6) spectrum of 4-amino-2,6-di(imidazol-1-yl)pyridine (**2**).

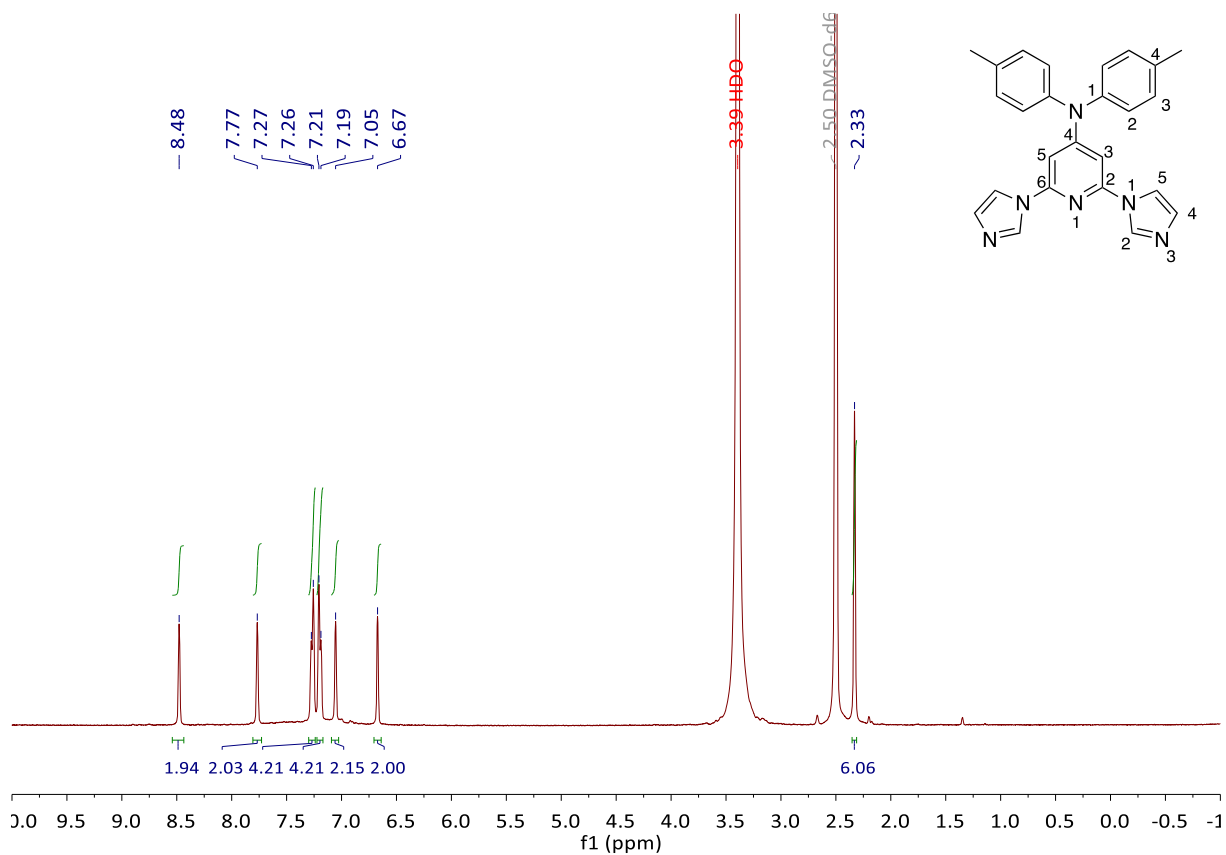


Figure S5. $^1\text{H NMR}$ (DMSO- d_6) spectrum of 2,6-di(imidazol-1-yl)-4-(di-*p*-tolylamino)pyridine (3).

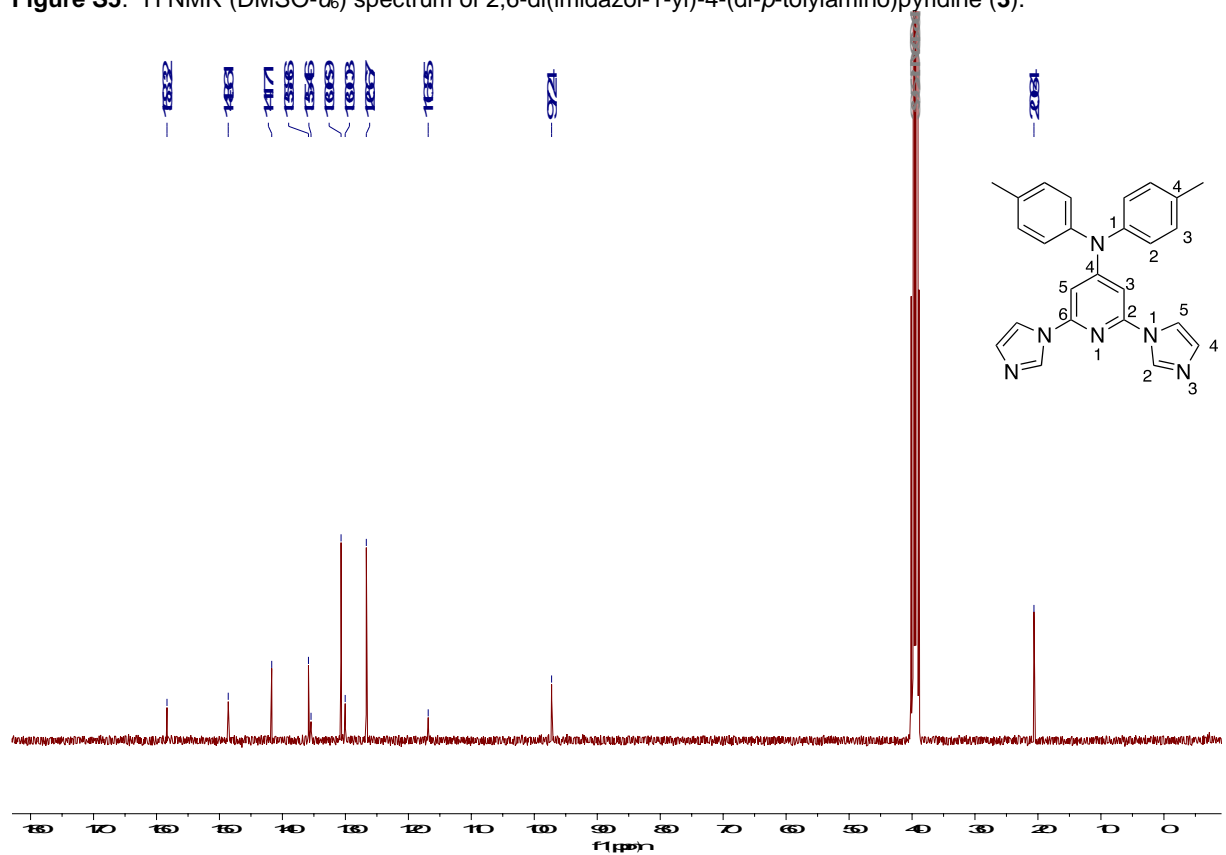


Figure S6. $^{13}\text{C NMR}$ (DMSO- d_6) spectrum of 2,6-di(imidazol-1-yl)-4-(di-*p*-tolylamino)pyridine (3).

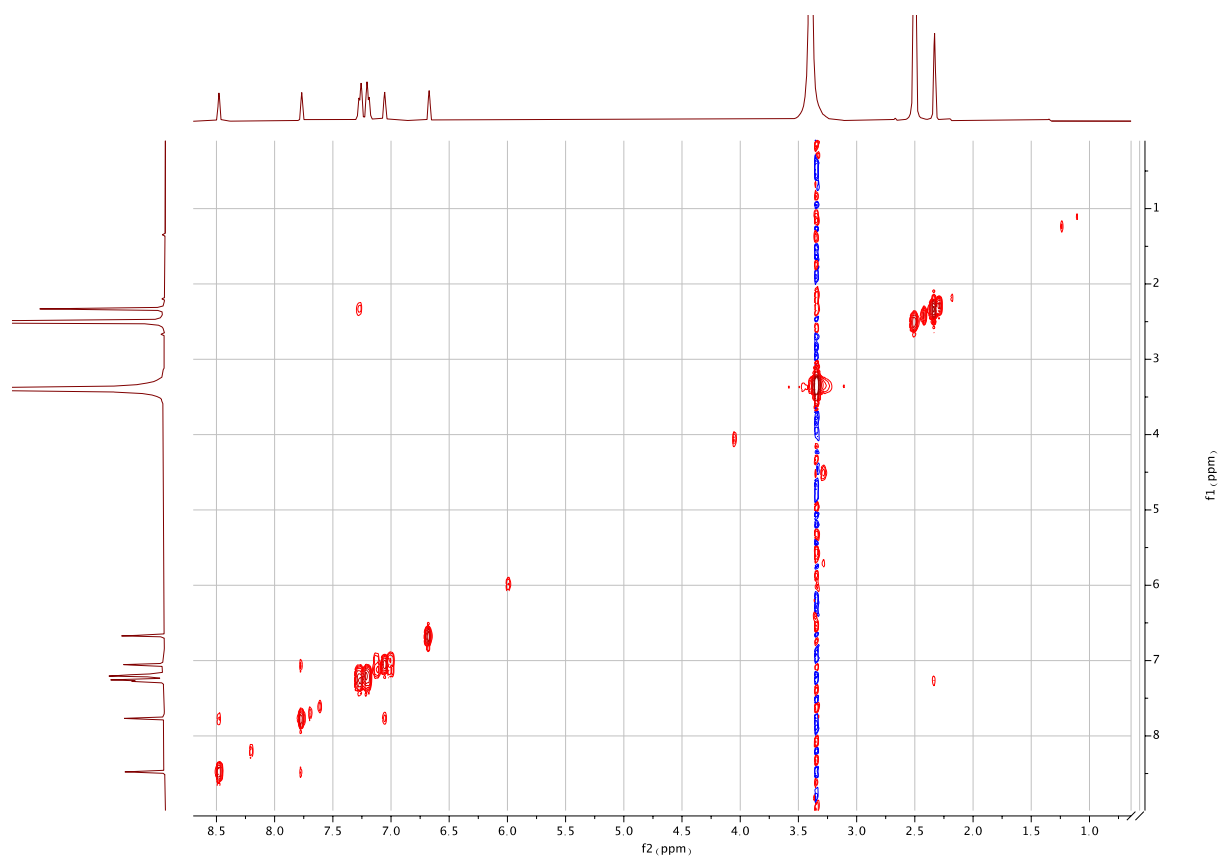


Figure S7. COSY NMR (DMSO- d_6) spectrum of 2,6-di(imidazol-1-yl)-4-(di-*p*-tolylamino)pyridine (**3**).

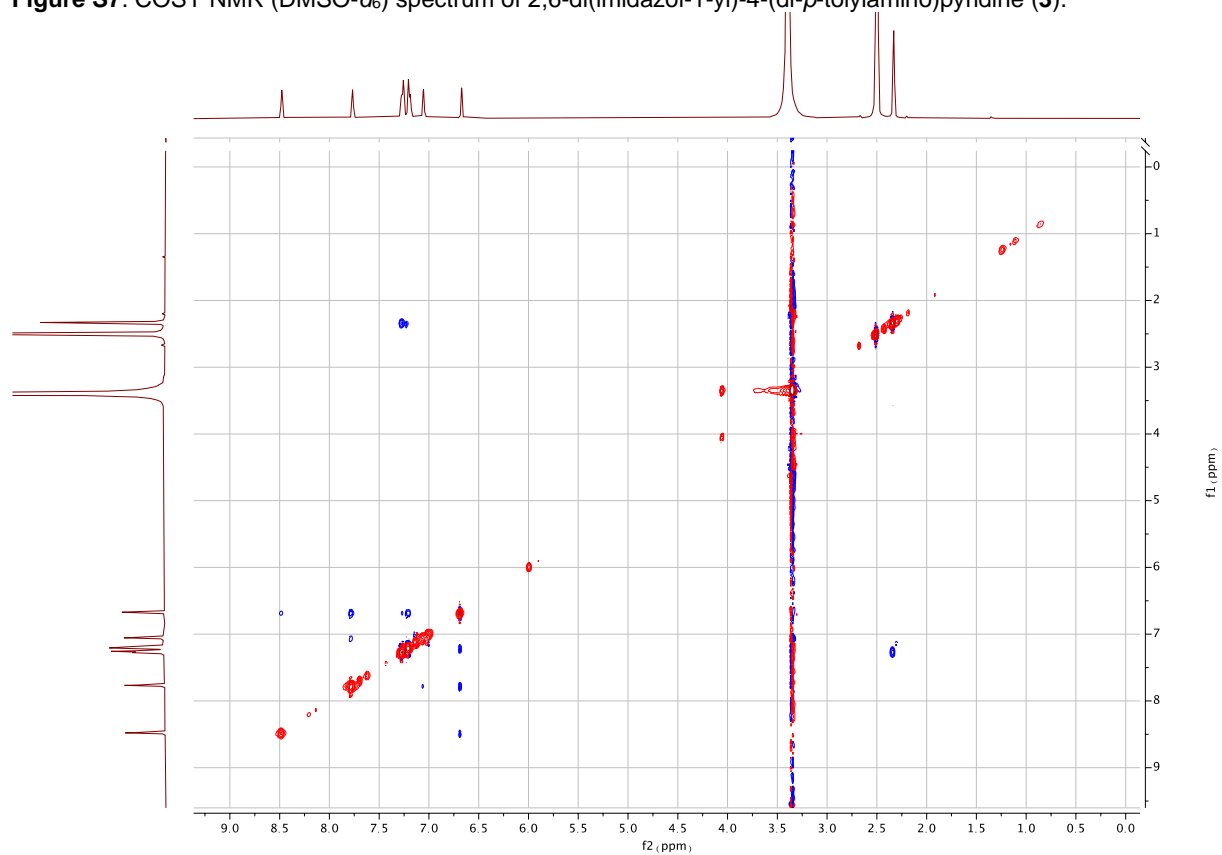


Figure S8. NOESY NMR (DMSO- d_6) spectrum of 2,6-di(imidazol-1-yl)-4-(di-*p*-tolylamino)pyridine (**3**).

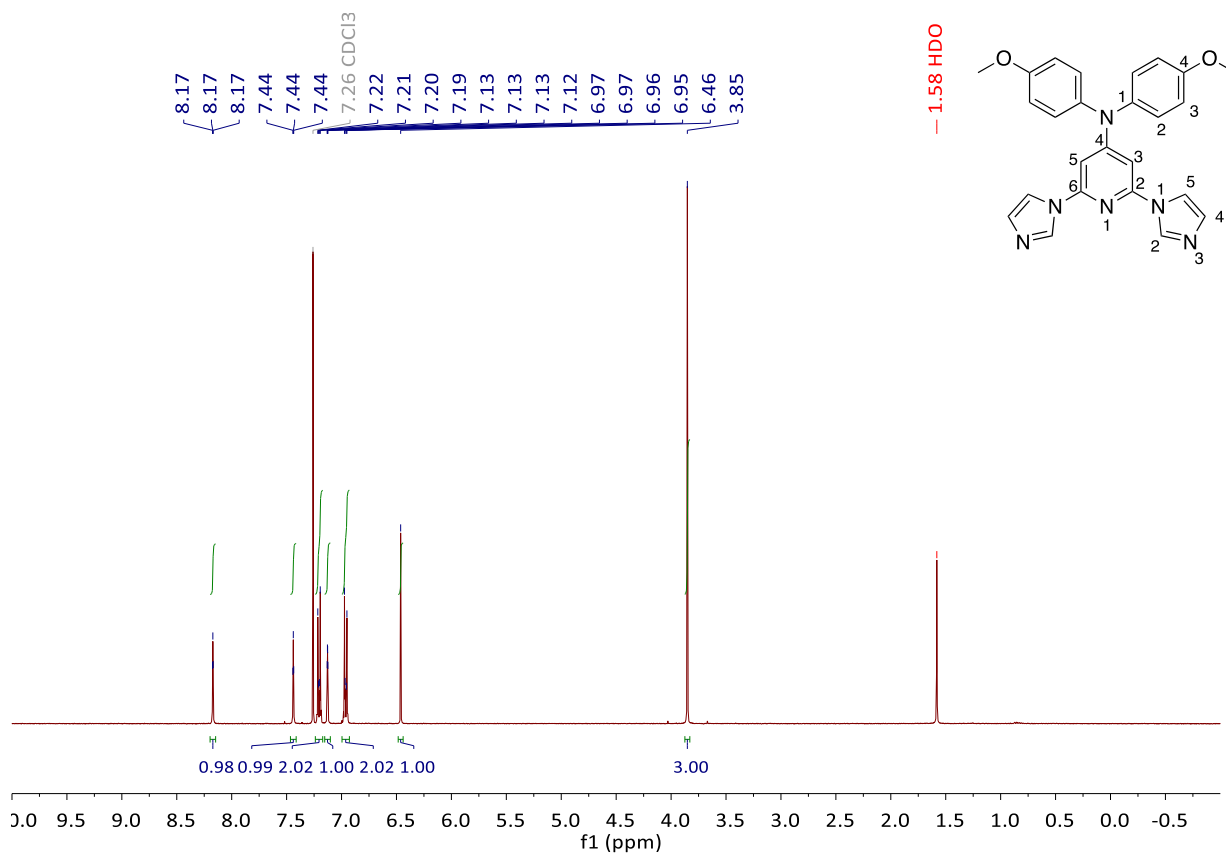


Figure S9. ¹H NMR (CDCl₃) spectrum of 2,6-di(imidazol-1-yl)-4-(di-*p*-anisylamino)pyridine (4).

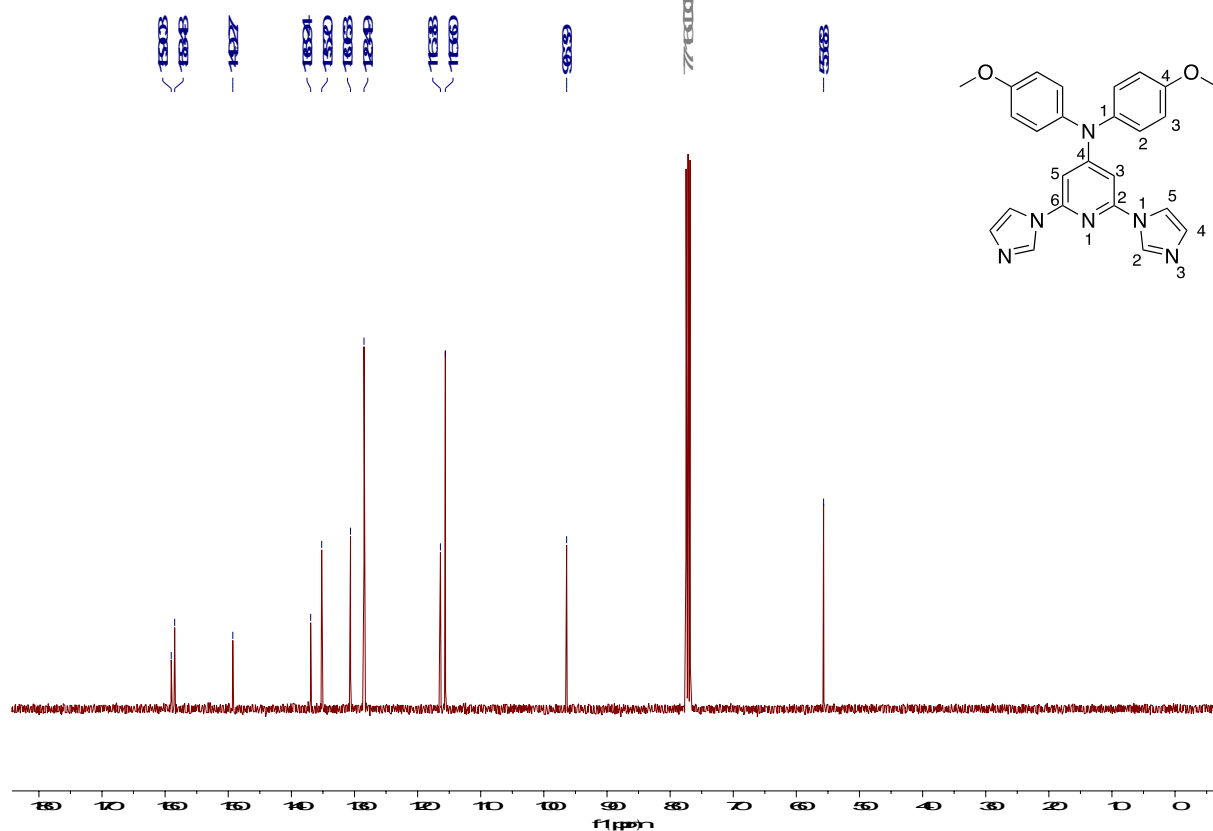


Figure S10. ¹³C NMR (CDCl₃) spectrum of 2,6-di(imidazol-1-yl)-4-(di-*p*-anisylamino)pyridine (4).

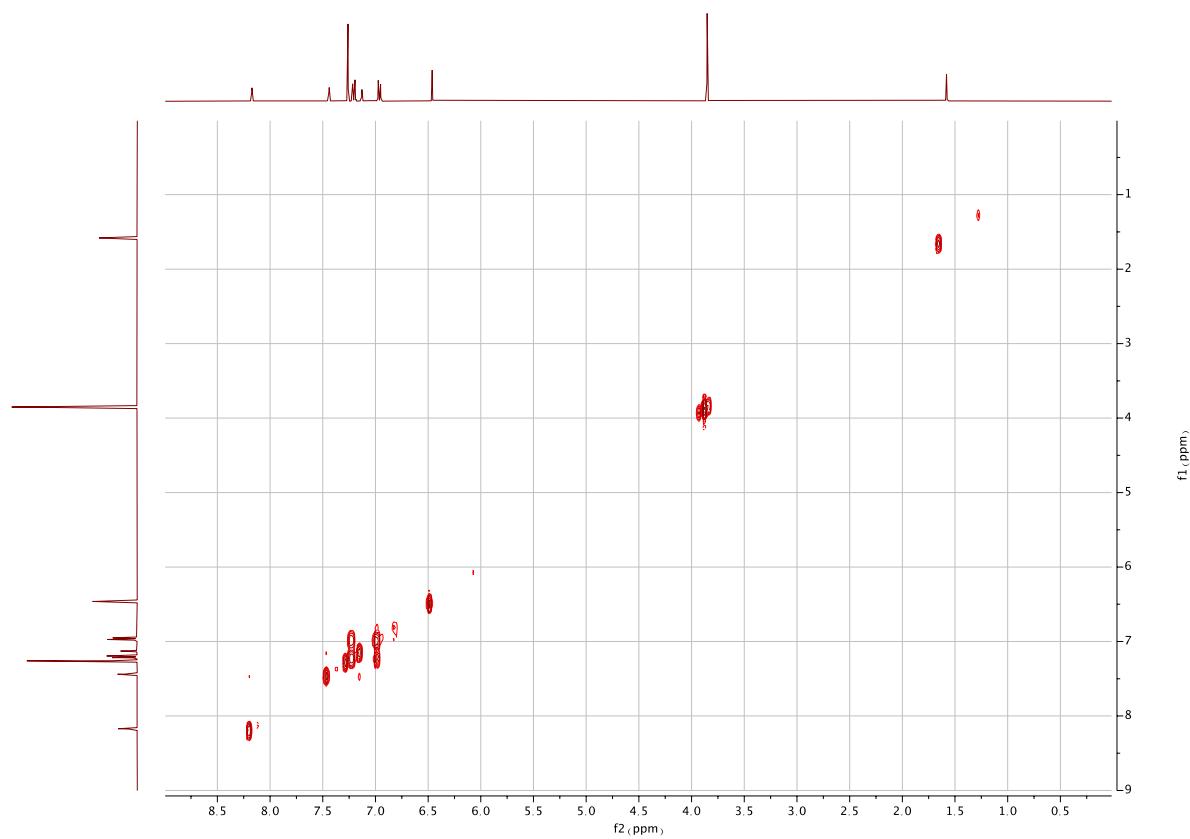


Figure S11. COSY NMR (CDCl_3) spectrum of 2,6-di(imidazol-1-yl)-4-(di-*p*-anisylamino)pyridine (**4**).

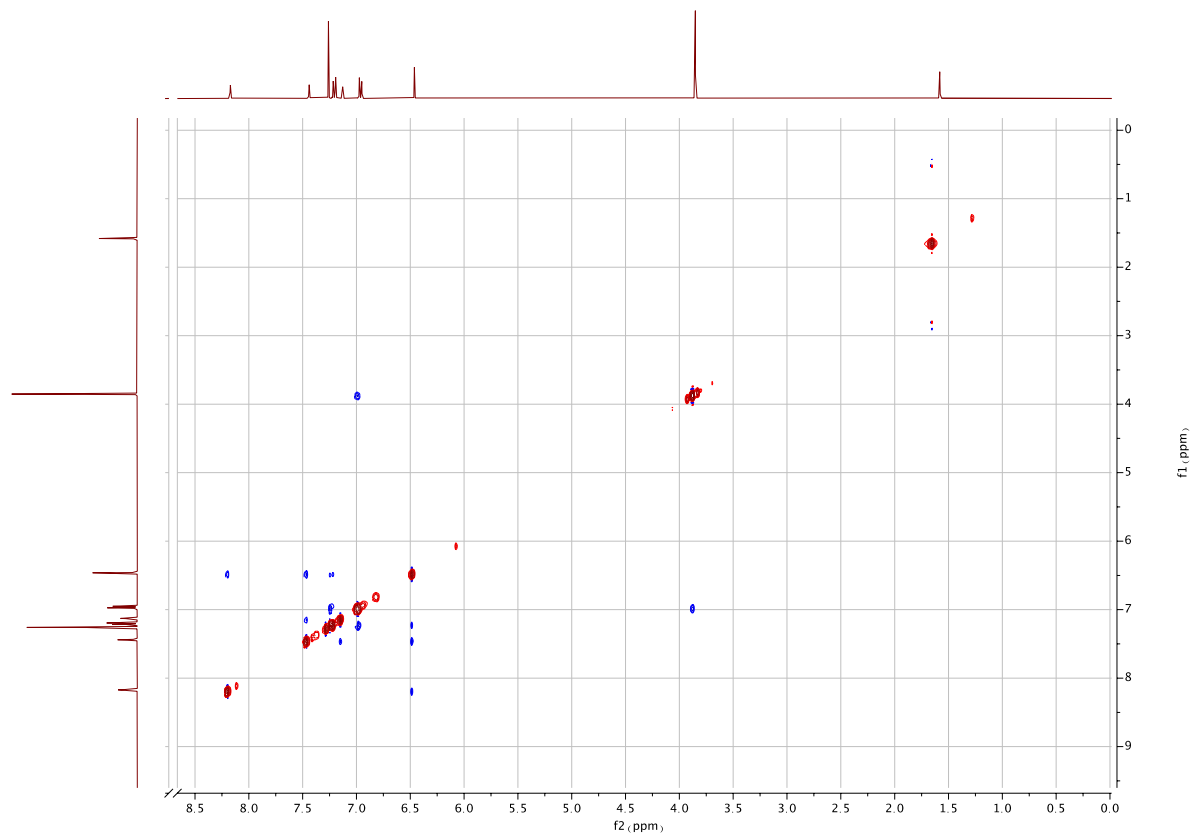


Figure S12. NOESY NMR (CDCl_3) spectrum of 2,6-di(imidazol-1-yl)-4-(di-*p*-anisylamino)pyridine (**4**).

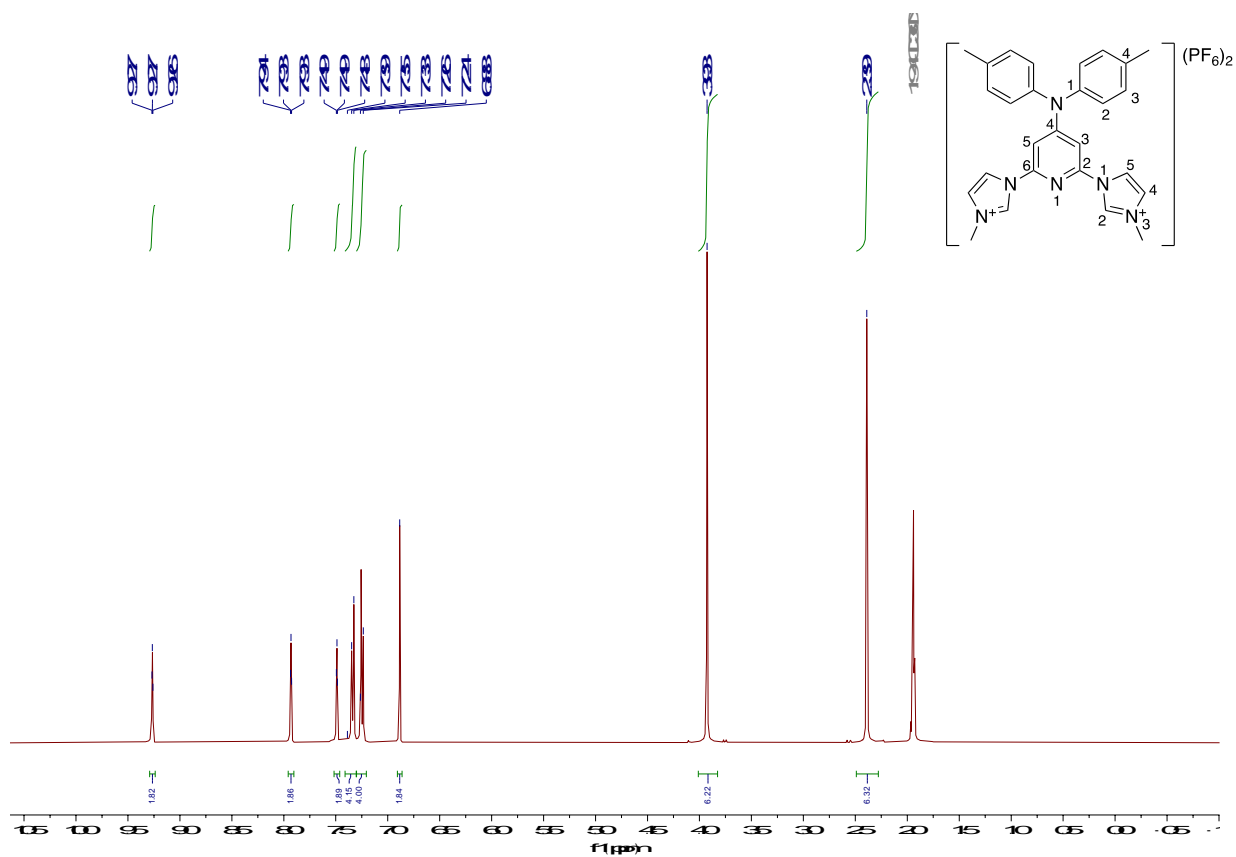


Figure S13. ^1H NMR (CD_3CN) spectrum of 1,1'-(4-(di-*p*-tolylamino)pyridine-2,6-diyl)bis(3-methylimidazolium) bis(hexafluorophosphate) (**[dtapbmiH₂](PF₆)₂**).

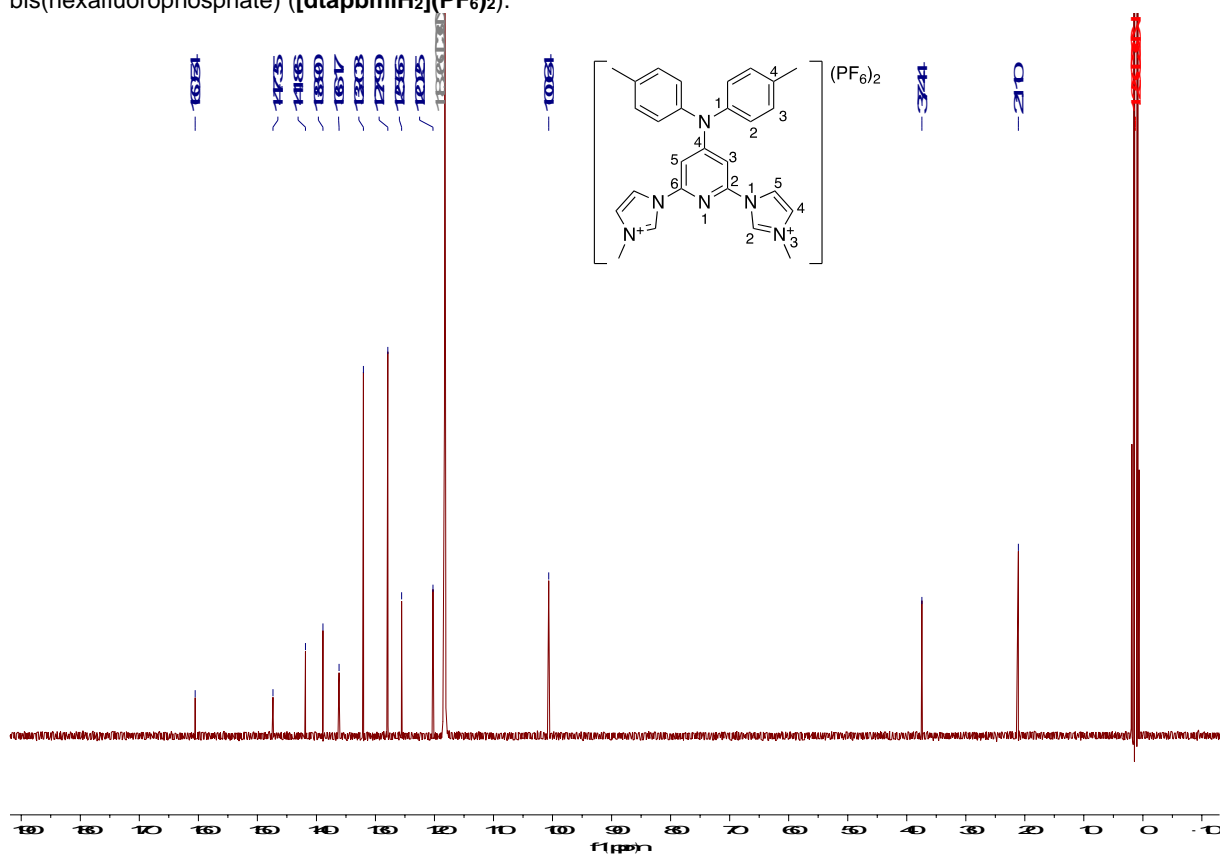


Figure S14. ^{13}C NMR (CD_3CN) spectrum of 1,1'-(4-(di-*p*-tolylamino)pyridine-2,6-diyl)bis(3-methylimidazolium) bis(hexafluorophosphate) (**[dtapbmiH₂](PF₆)₂**).

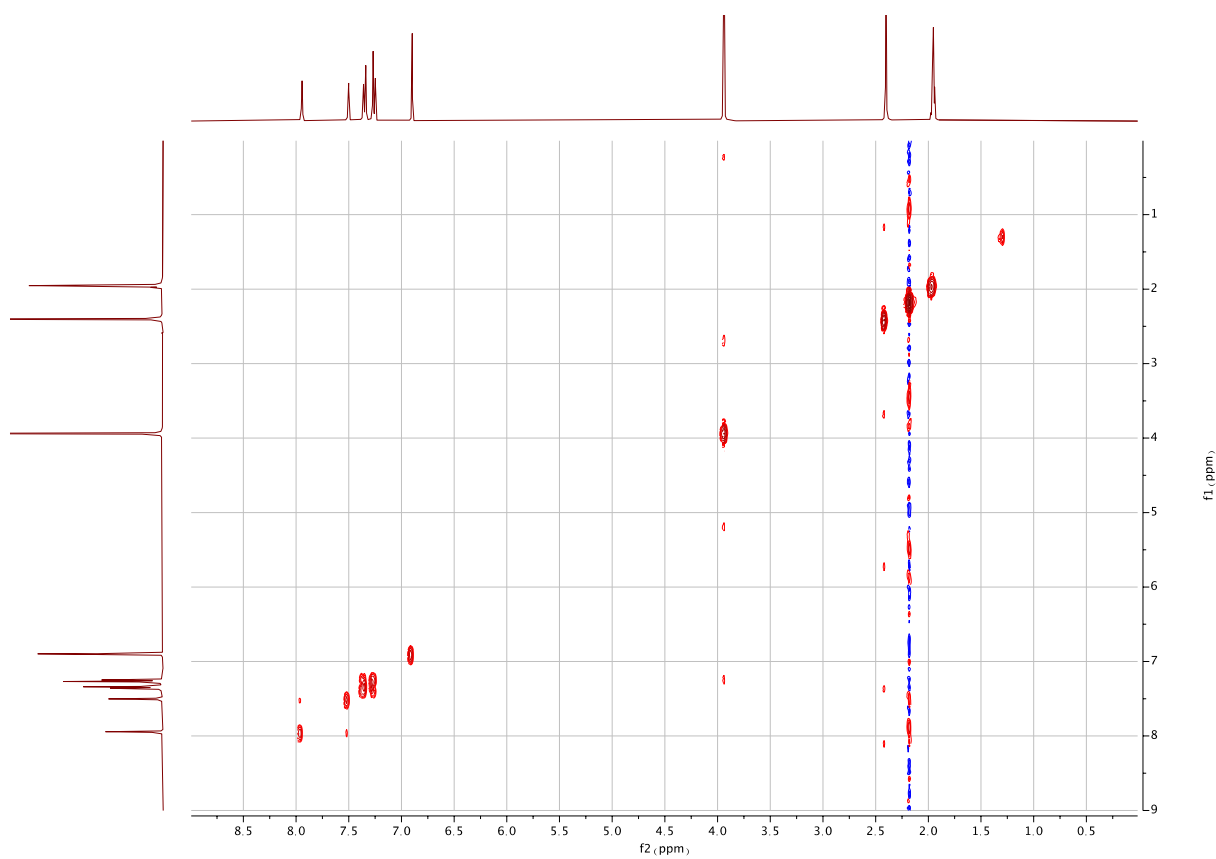


Figure S15. COSY NMR (CD_3CN) spectrum of 1,1'-(4-(di-*p*-tolylamino)pyridine-2,6-diyl)bis(3-methylimidazolium) bis(hexafluorophosphate) ($[\text{dtapbmiH}_2](\text{PF}_6)_2$).

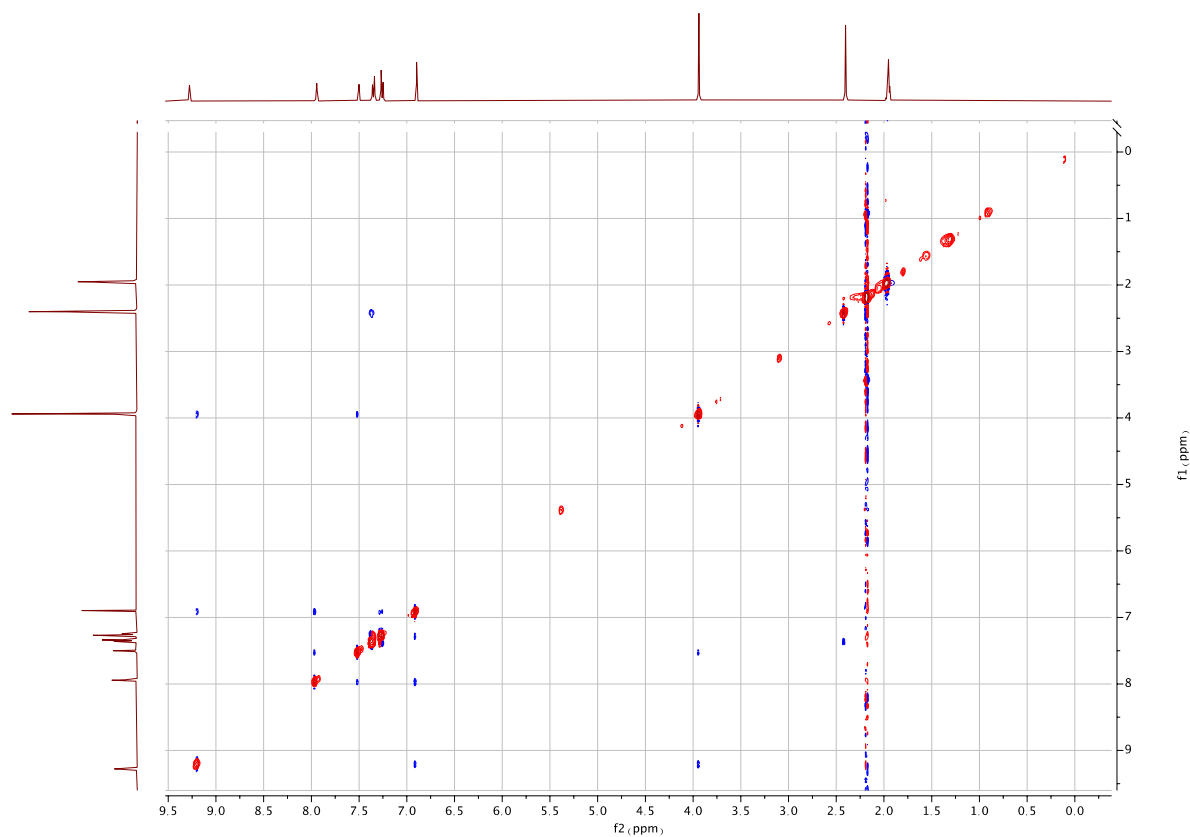


Figure S16. NOESY NMR (CD_3CN) spectrum of 1,1'-(4-(di-*p*-tolylamino)pyridine-2,6-diyl)bis(3-methylimidazolium) bis(hexafluorophosphate) ($[\text{dtapbmiH}_2](\text{PF}_6)_2$).

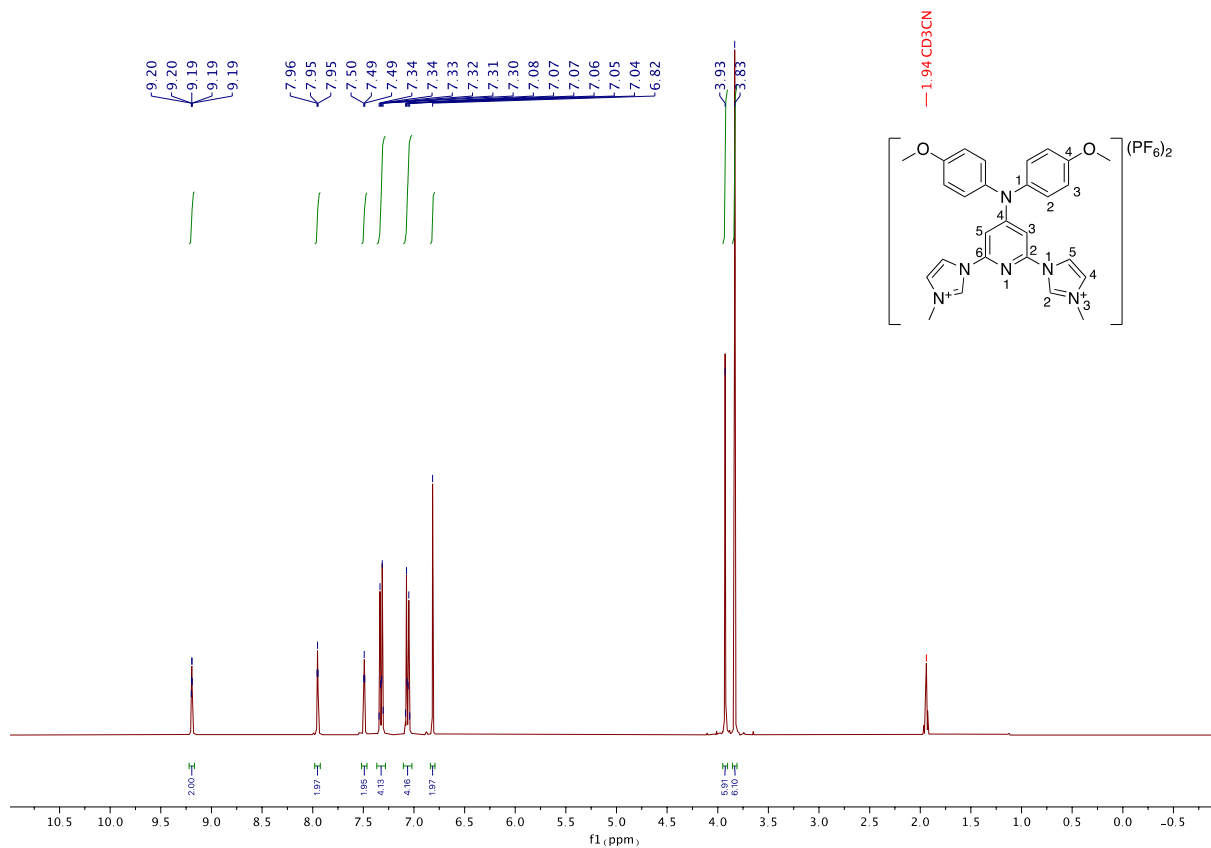


Figure S17. ¹H NMR (CD₃CN) spectrum of 1,1'-(4-(di-*p*-anisylamino)pyridine-2,6-diyl)bis(3-methylimidazolium) bis(hexafluorophosphate) ([daapbmiH₂](PF₆)₂).

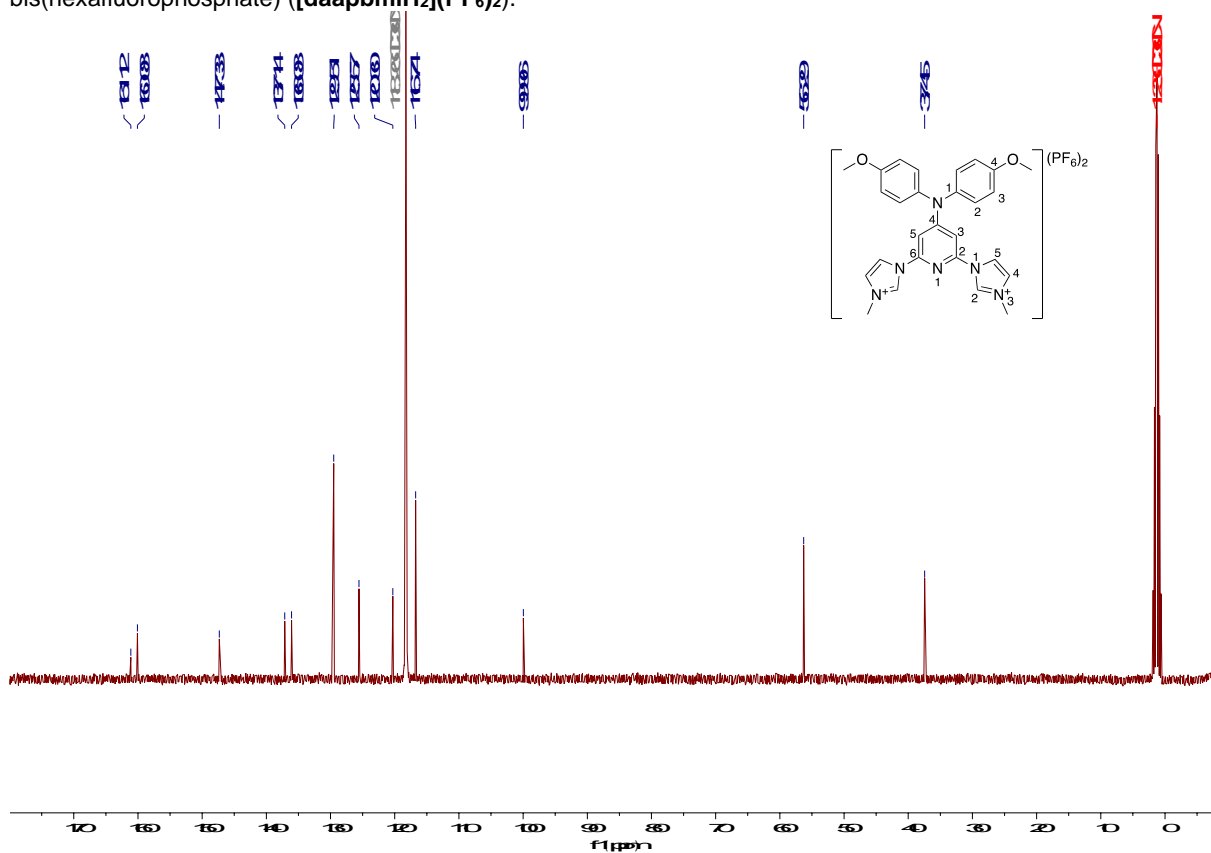


Figure S18. ¹³C NMR (CD₃CN) spectrum of 1,1'-(4-(di-*p*-anisylamino)pyridine-2,6-diyl)bis(3-methylimidazolium) bis(hexafluorophosphate) ([daapbmiH₂](PF₆)₂).

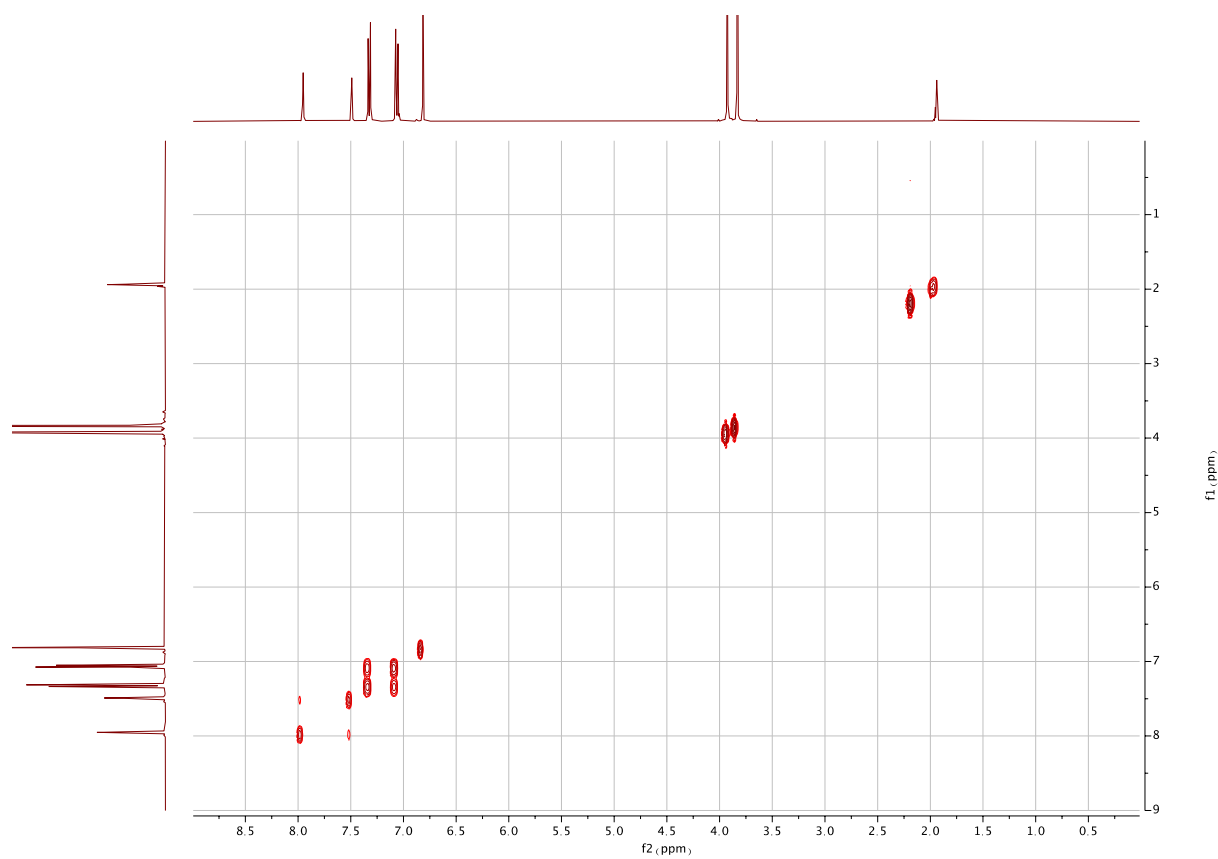


Figure S19. COSY NMR (CD_3CN) spectrum of 1,1'-(4-(di-*p*-anisylamino)pyridine-2,6-diyl)bis(3-methylimidazolium) bis(hexafluorophosphate) (**[daapbmiH₂](PF₆)₂**).

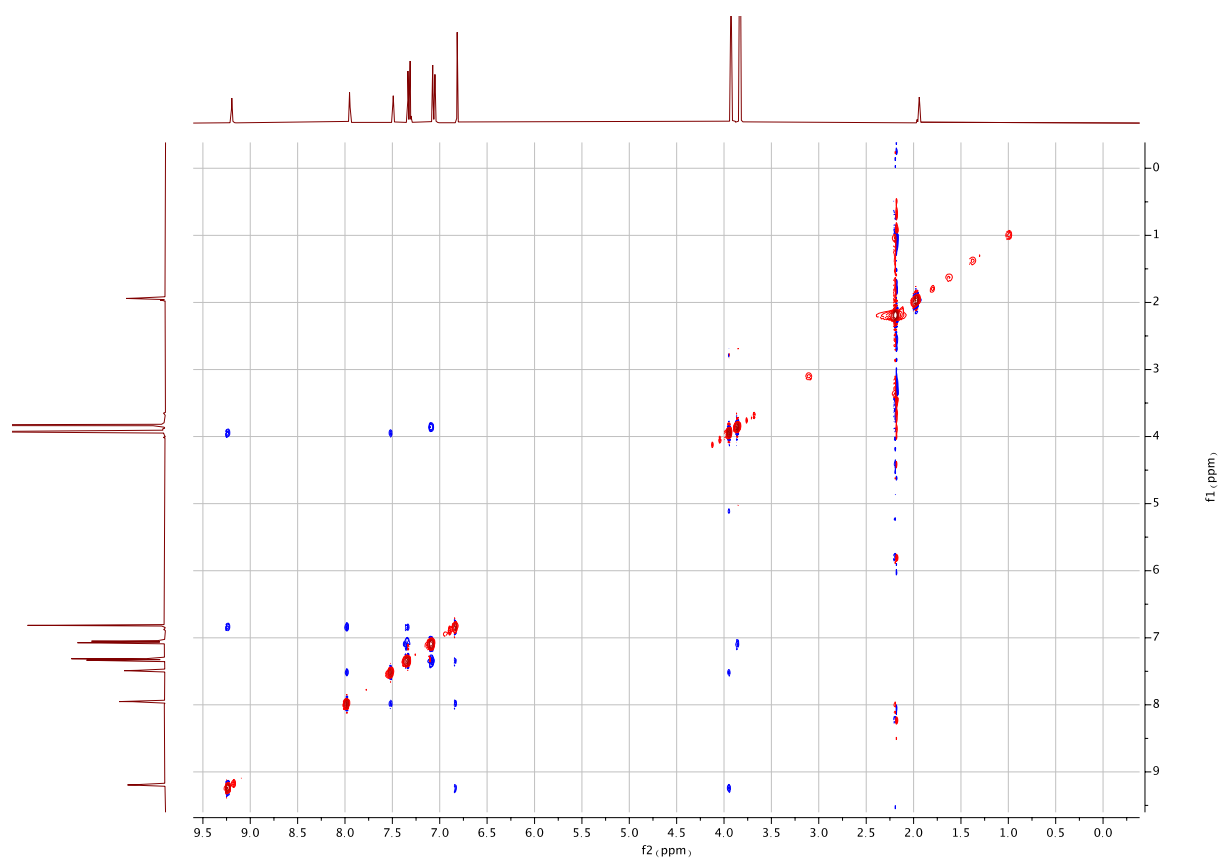


Figure S20. NOESY NMR (CD_3CN) spectrum of 1,1'-(4-(di-*p*-anisylamino)pyridine-2,6-diyl)bis(3-methylimidazolium) bis(hexafluorophosphate) (**[daapbmiH₂](PF₆)₂**).

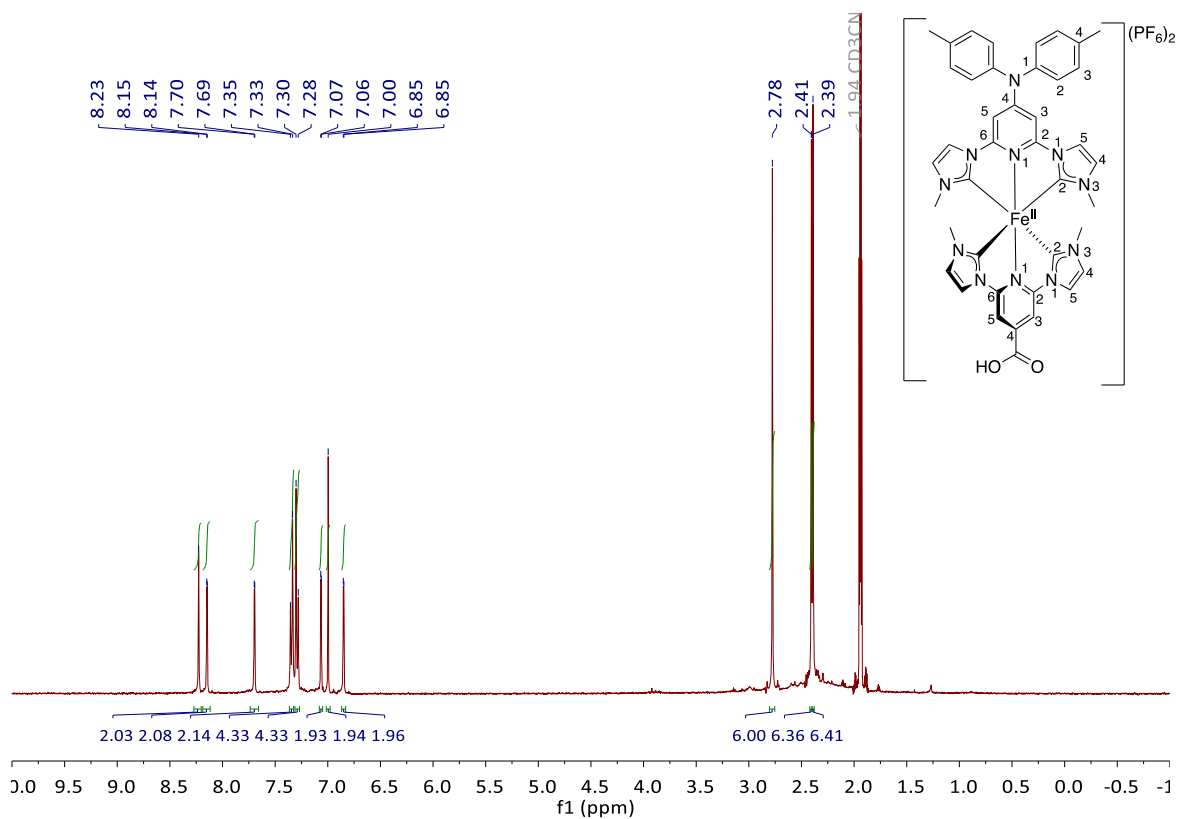


Figure S21. ^1H NMR (CD_3CN) spectrum of (1,1'-(4-carboxypyridine-2,6-diyl)bis(3-methylimidazol-2-ylidene))(1,1'-(4-(di-*p*-tolylamino)pyridine-2,6-diyl)bis(3-methylimidazol-2-ylidene))iron(II) bis(hexafluorophosphate) ($[\text{Fe}(\text{cpbmi})(\text{dtapbmi})](\text{PF}_6)_2$).

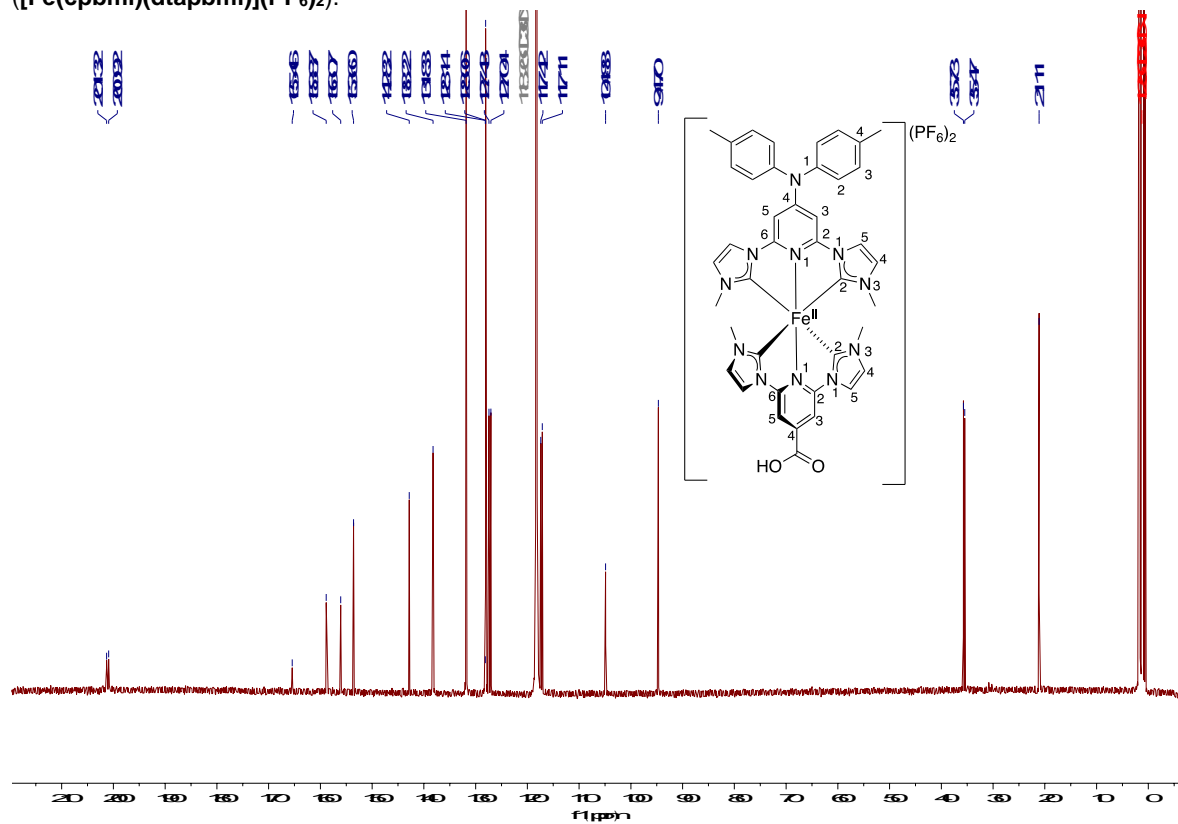


Figure S22. ^{13}C NMR (CD_3CN) spectrum of (1,1'-(4-carboxypyridine-2,6-diyl)bis(3-methylimidazol-2-ylidene))(1,1'-(4-(di-*p*-tolylamino)pyridine-2,6-diyl)bis(3-methylimidazol-2-ylidene))iron(II) bis(hexafluorophosphate) ($[\text{Fe}(\text{cpbmi})(\text{dtapbmi})](\text{PF}_6)_2$).

$[\text{Fe}(\text{cpbmi})(\text{dtapbmi})](\text{PF}_6)_2$.

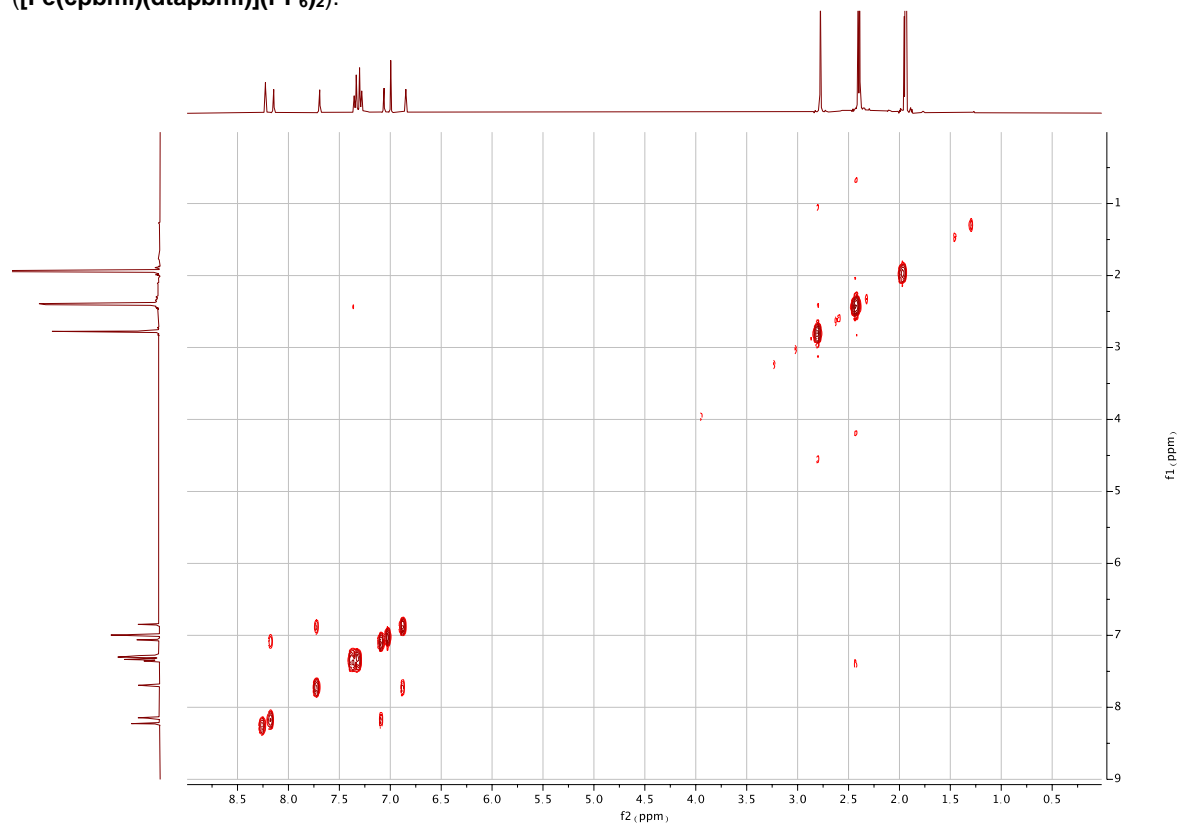


Figure S23. COSY NMR (CD_3CN) spectrum of (1,1'-(4-carboxypyridine-2,6-diyl)bis(3-methylimidazol-2-ylidene))(1,1'-(4-(di-*p*-tolylamino)pyridine-2,6-diyl)bis(3-methylimidazol-2-ylidene))iron(II) bis(hexafluorophosphate) ($[\text{Fe}(\text{cpbmi})(\text{dtapbmi})](\text{PF}_6)_2$).

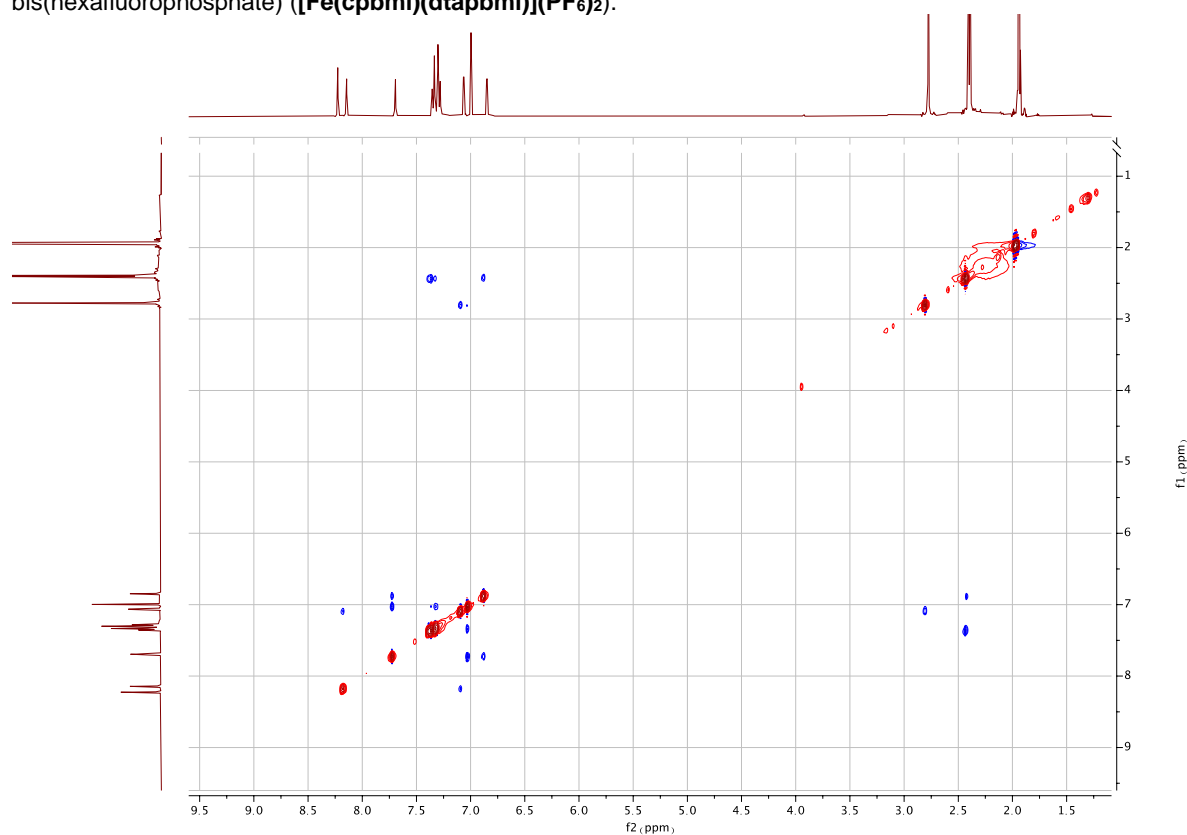


Figure S24. NOESY NMR (CD_3CN) spectrum of (1,1'-(4-carboxypyridine-2,6-diyl)bis(3-methylimidazol-2-ylidene))(1,1'-(4-(di-*p*-tolylamino)pyridine-2,6-diyl)bis(3-methylimidazol-2-ylidene))iron(II) bis(hexafluorophosphate) ($[\text{Fe}(\text{cpbmi})(\text{dtapbmi})](\text{PF}_6)_2$).

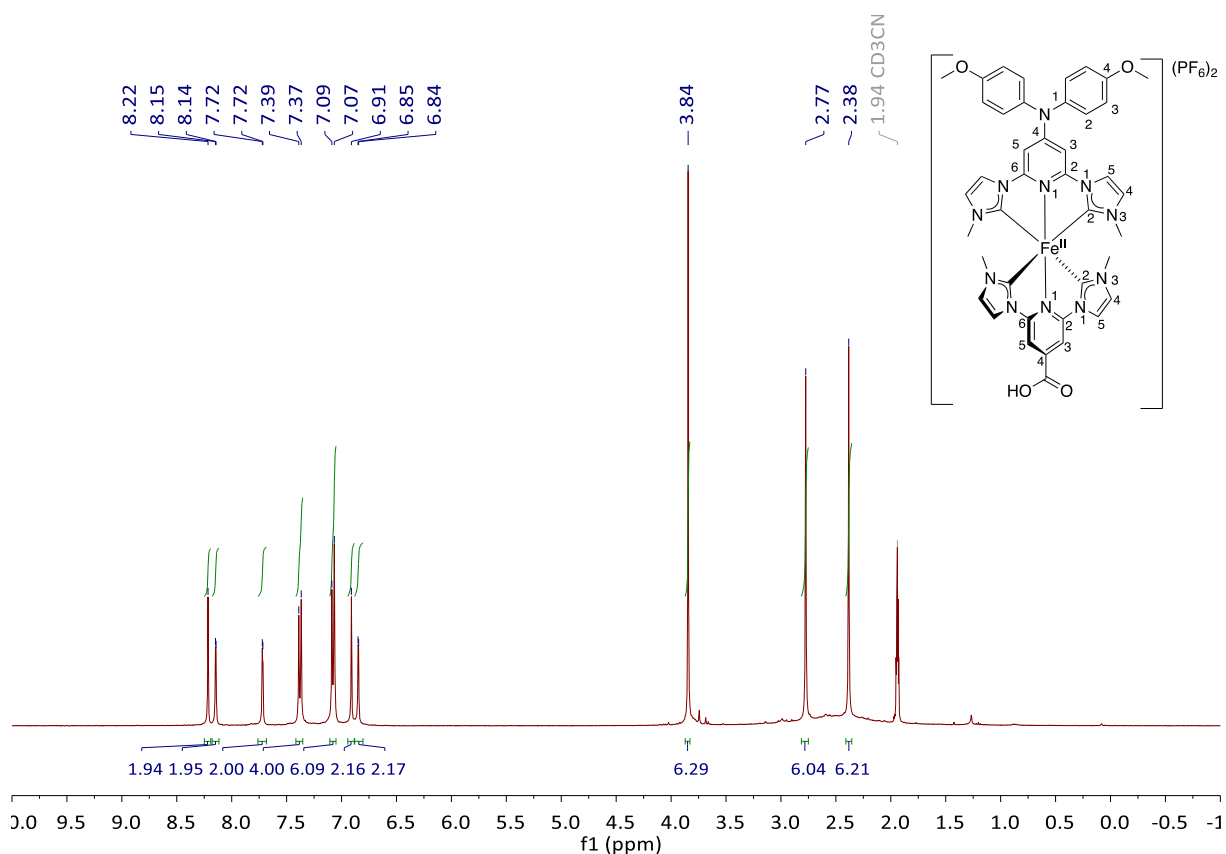


Figure S25. ^1H NMR (CD₃CN) spectrum of (1,1'-(4-(di-*p*-anisylamino)pyridine-2,6-diyl)bis(3-methylimidazol-2-ylidene)) (1,1'-(4-carboxypyridine-2,6-diyl)bis(3-methylimidazol-2-ylidene))iron(II) bis(hexafluorophosphate) $[(\text{Fe}(\text{cpbmi})(\text{daapbmi}))(\text{PF}_6)_2]$.

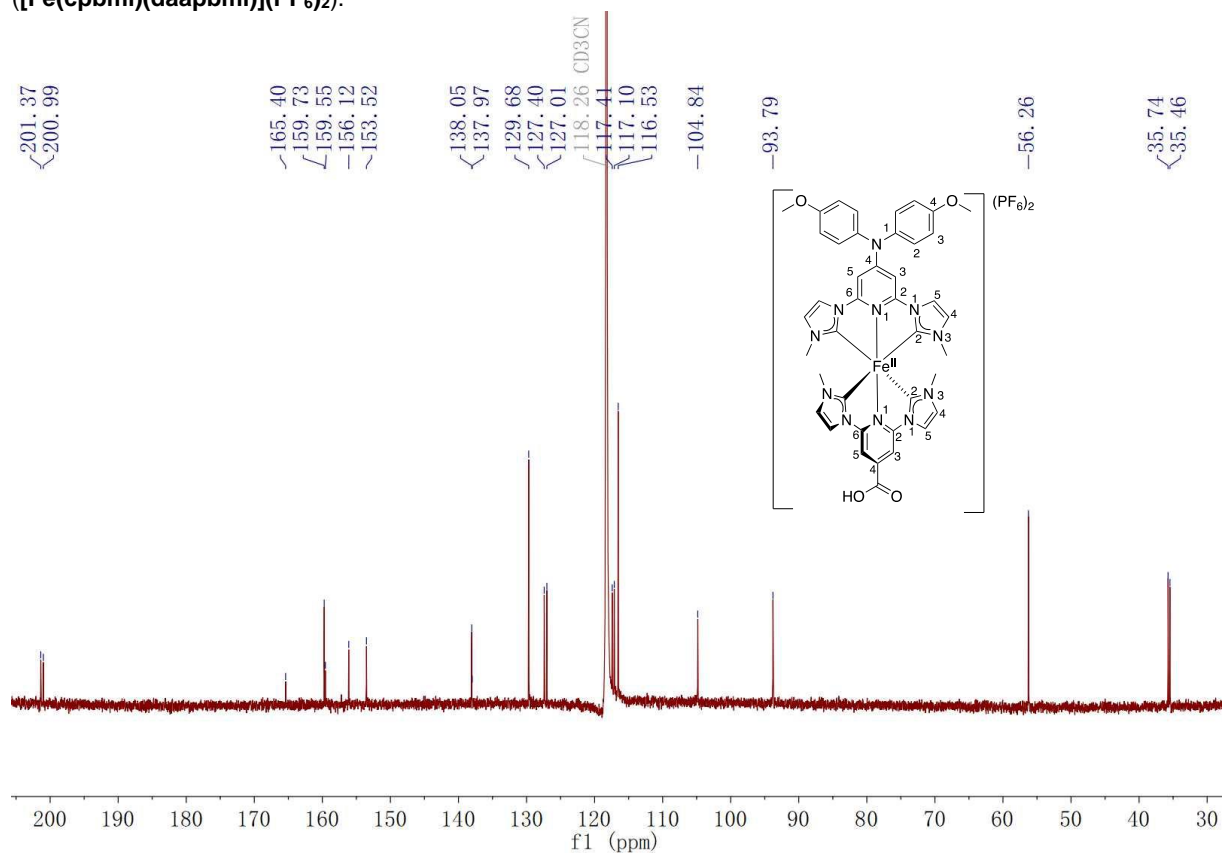


Figure S26. ^{13}C NMR (CD₃CN) spectrum of (1,1'-(4-(di-*p*-anisylamino)pyridine-2,6-diyl)bis(3-methylimidazol-2-ylidene)) (1,1'-(4-carboxypyridine-2,6-diyl)bis(3-methylimidazol-2-ylidene))iron(II) bis(hexafluorophosphate) $[(\text{Fe}(\text{cpbmi})(\text{daapbmi}))(\text{PF}_6)_2]$.

$[\text{Fe}(\text{cpbmi})(\text{daapbmi})](\text{PF}_6)_2$.

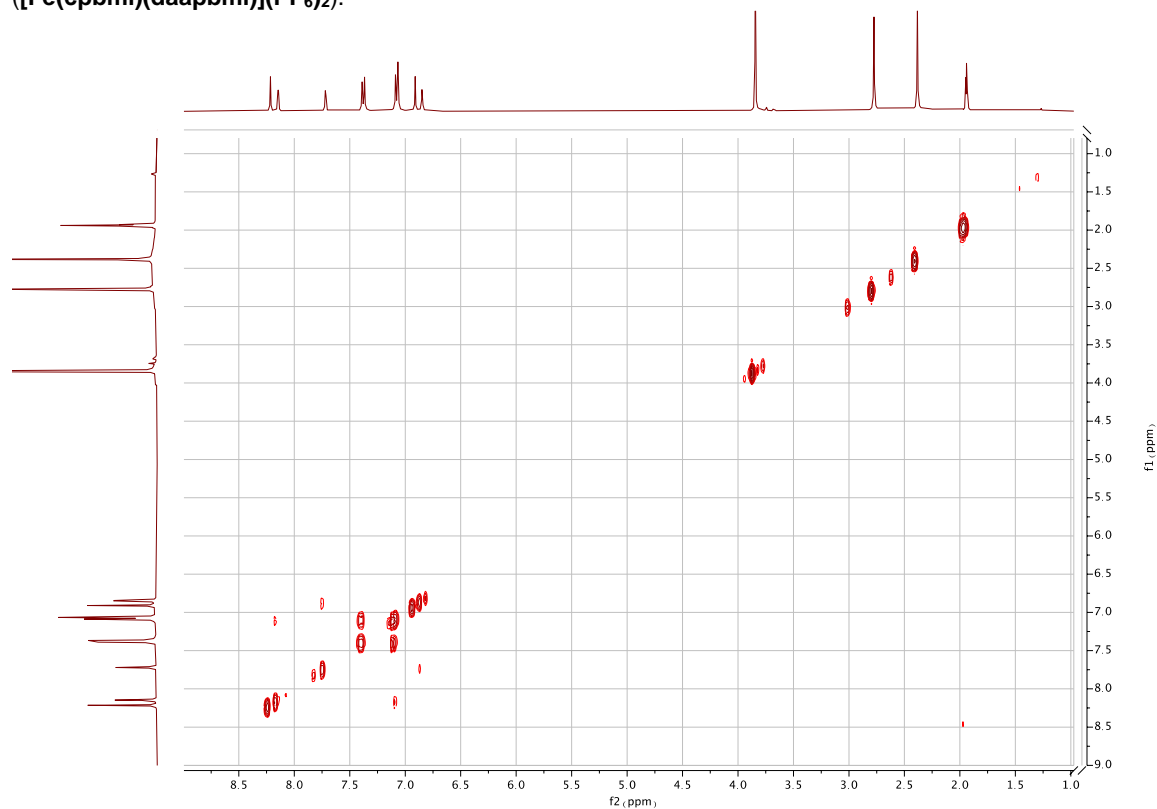


Figure S27. COSY NMR (CD_3CN) spectrum of (1,1'-(4-(di-*p*-anisylamino)pyridine-2,6-diyl)bis(3-methylimidazol-2-ylidene)) (1,1'-(4-carboxypyridine-2,6-diyl)bis(3-methylimidazol-2-ylidene))iron(II) bis(hexafluorophosphate) $[\text{Fe}(\text{cpbmi})(\text{daapbmi})](\text{PF}_6)_2$.

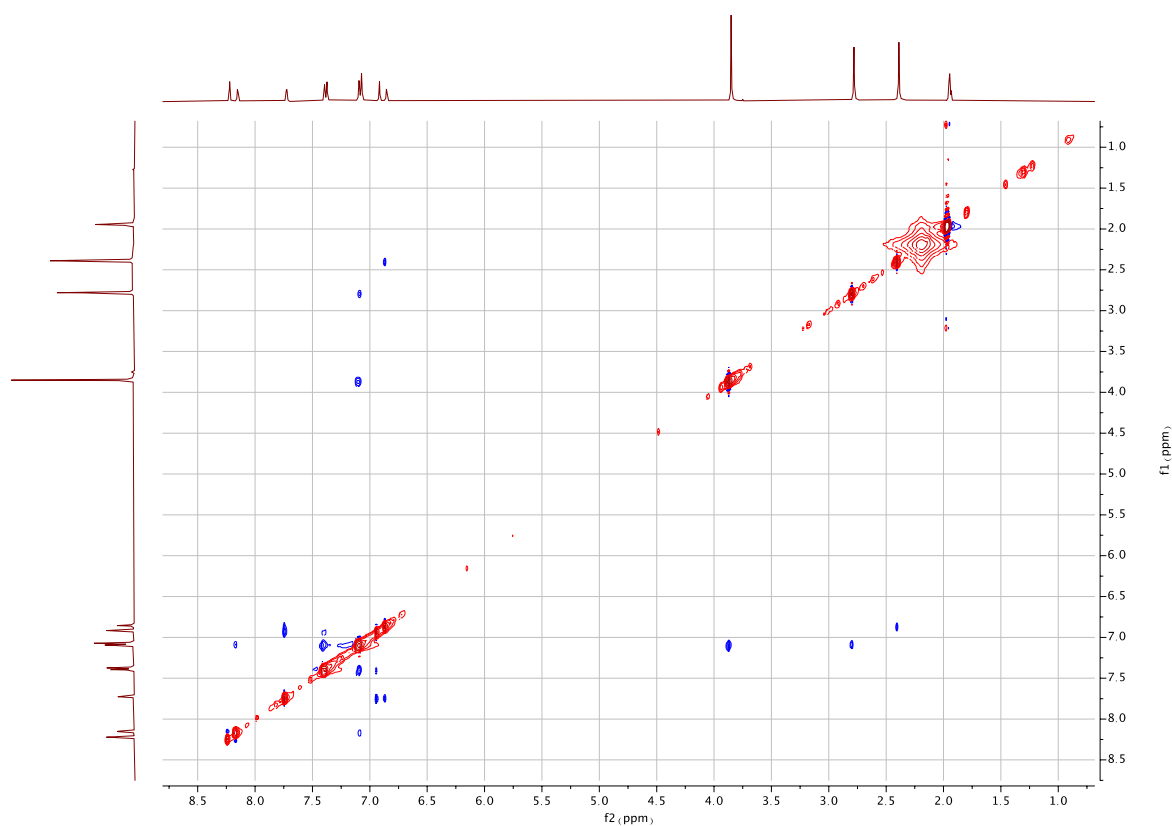


Figure S28. NOSEY NMR (CD_3CN) spectrum of (1,1'-(4-(di-*p*-anisylamino)pyridine-2,6-diyl)bis(3-methylimidazol-2-ylidene)) (1,1'-(4-carboxypyridine-2,6-diyl)bis(3-methylimidazol-2-ylidene))iron(II) bis(hexafluorophosphate) $[\text{Fe}(\text{cpbmi})(\text{daapbmi})](\text{PF}_6)_2$.

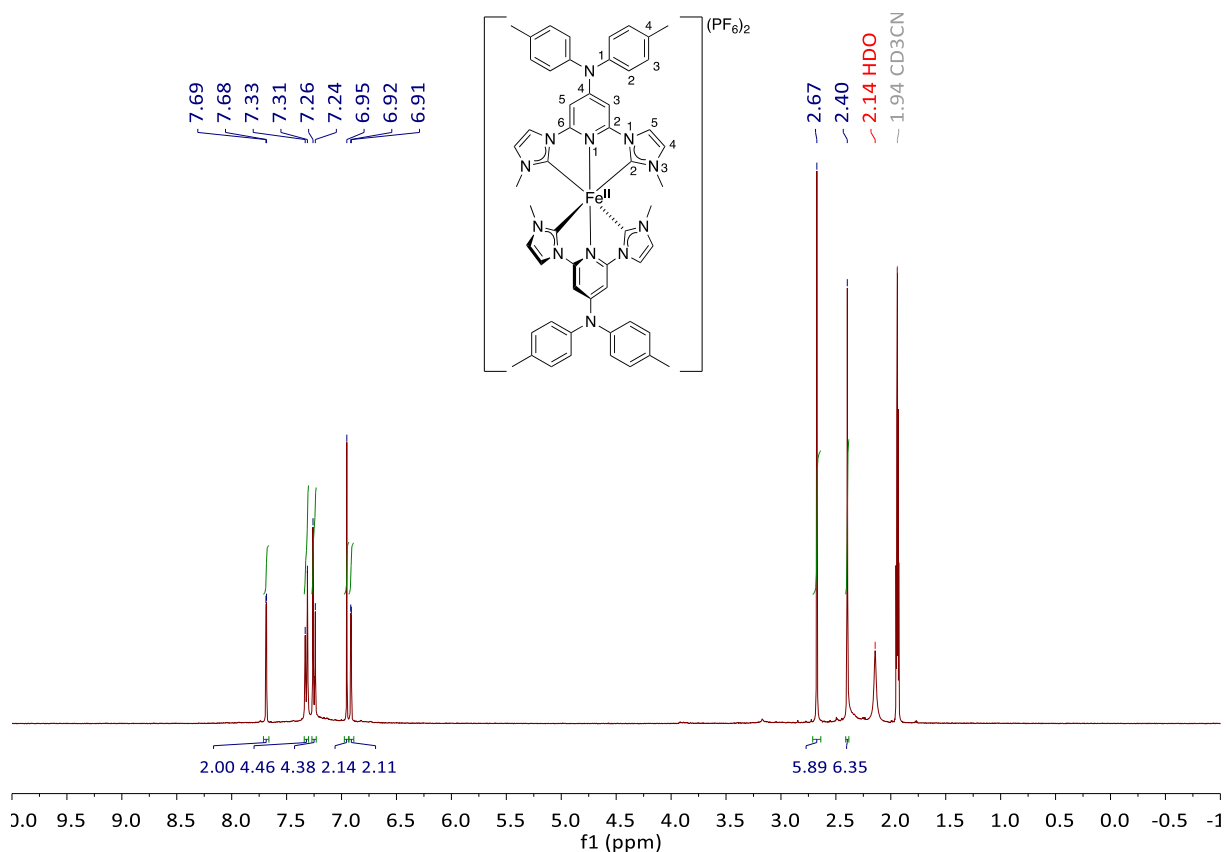


Figure S29. ^1H NMR (CD_3CN) spectrum of bis(1,1'-(4-(di-*p*-tolylamino)pyridine-2,6-diyl)bis(3-methylimidazol-2-ylidene))iron(II) bis(hexafluorophosphate) ($[\text{Fe}(\text{dtapbmi})_2](\text{PF}_6)_2$).

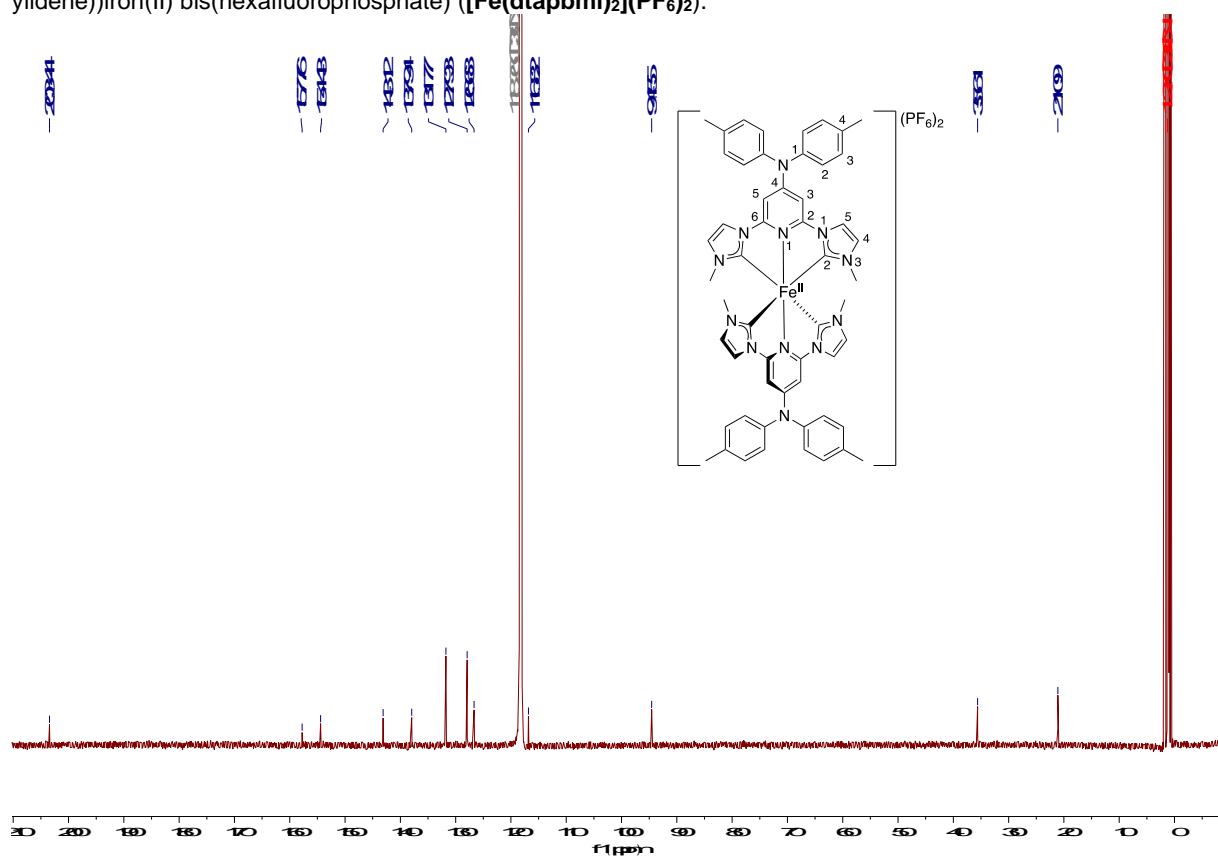


Figure S30. ^{13}C NMR (CD_3CN) spectrum of bis(1,1'-(4-(di-*p*-tolylamino)pyridine-2,6-diyl)bis(3-methylimidazol-2-

ylidene))iron(II)

bis(hexafluorophosphate)

$[\text{Fe}(\text{dtapbmi})_2](\text{PF}_6)_2$.

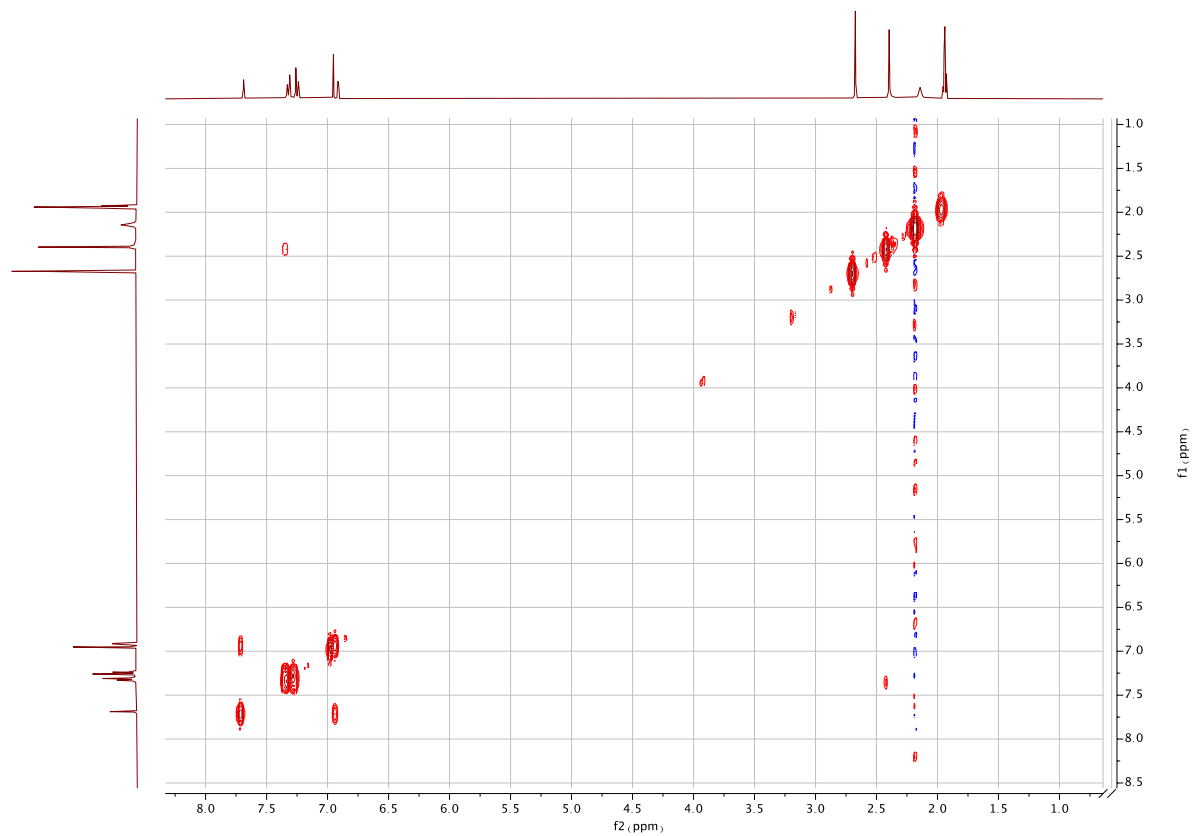


Figure S31. COSY NMR (CD_3CN) spectrum of bis(1,1'-(4-(di-*p*-tolylamino)pyridine-2,6-diyl)bis(3-methylimidazol-2-ylidene))iron(II) bis(hexafluorophosphate) ($[\text{Fe}(\text{dtapbmi})_2](\text{PF}_6)_2$).

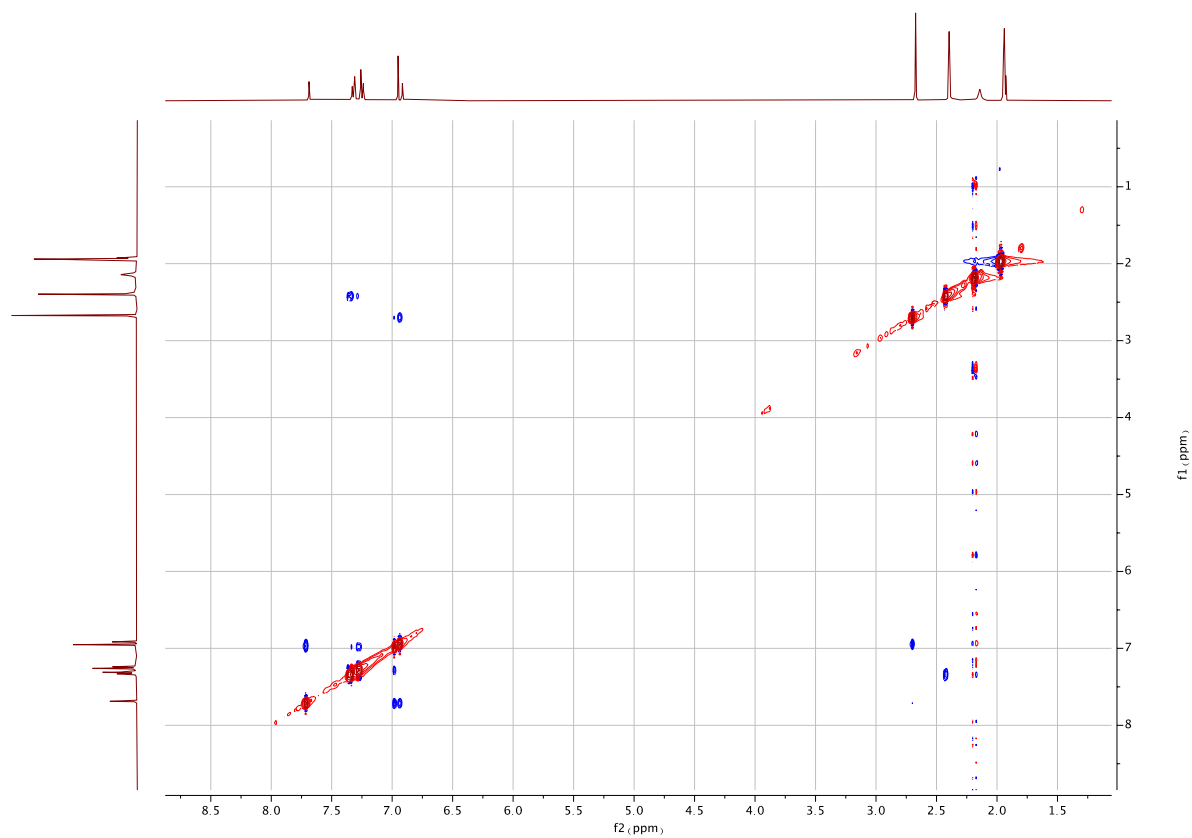


Figure S32. NOSEY NMR (CD_3CN) spectrum of bis(1,1'-(4-(di-*p*-tolylamino)pyridine-2,6-diyl)bis(3-methylimidazol-2-ylidene))iron(II) bis(hexafluorophosphate) ($[\text{Fe}(\text{dtapbmi})_2](\text{PF}_6)_2$).

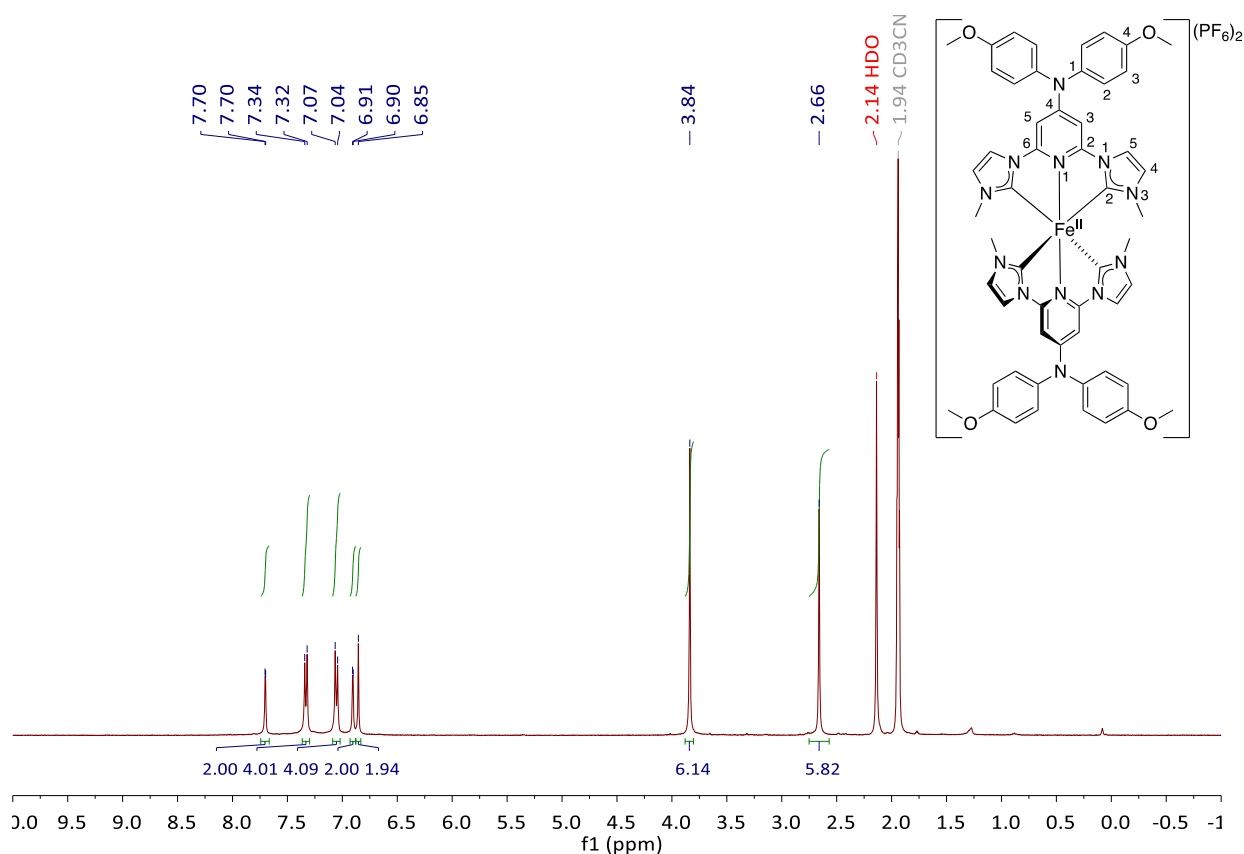


Figure S33. ^1H NMR (CD_3CN) spectrum of bis(1,1'-(4-(di-*p*-anisylamino)pyridine-2,6-diyl)bis(3-methylimidazol-2-ylidene))iron(II) bis(hexafluorophosphate) ($[\text{Fe}(\text{daapbmi})_2](\text{PF}_6)_2$).

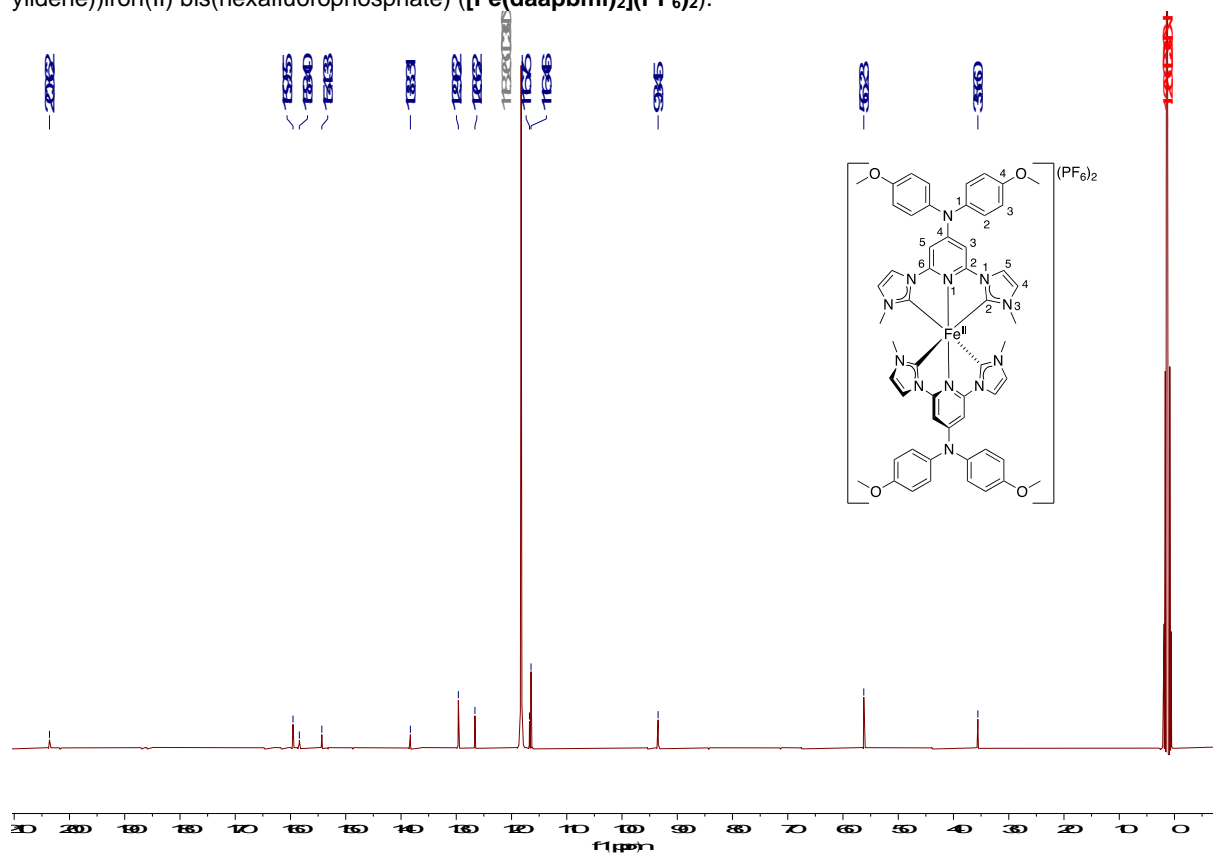


Figure S34. ^{13}C NMR (CD_3CN) spectrum of bis(1,1'-(4-(di-*p*-anisylamino)pyridine-2,6-diyl)bis(3-methylimidazol-2-ylidene))iron(II) bis(hexafluorophosphate) ($[\text{Fe}(\text{daapbmi})_2](\text{PF}_6)_2$).

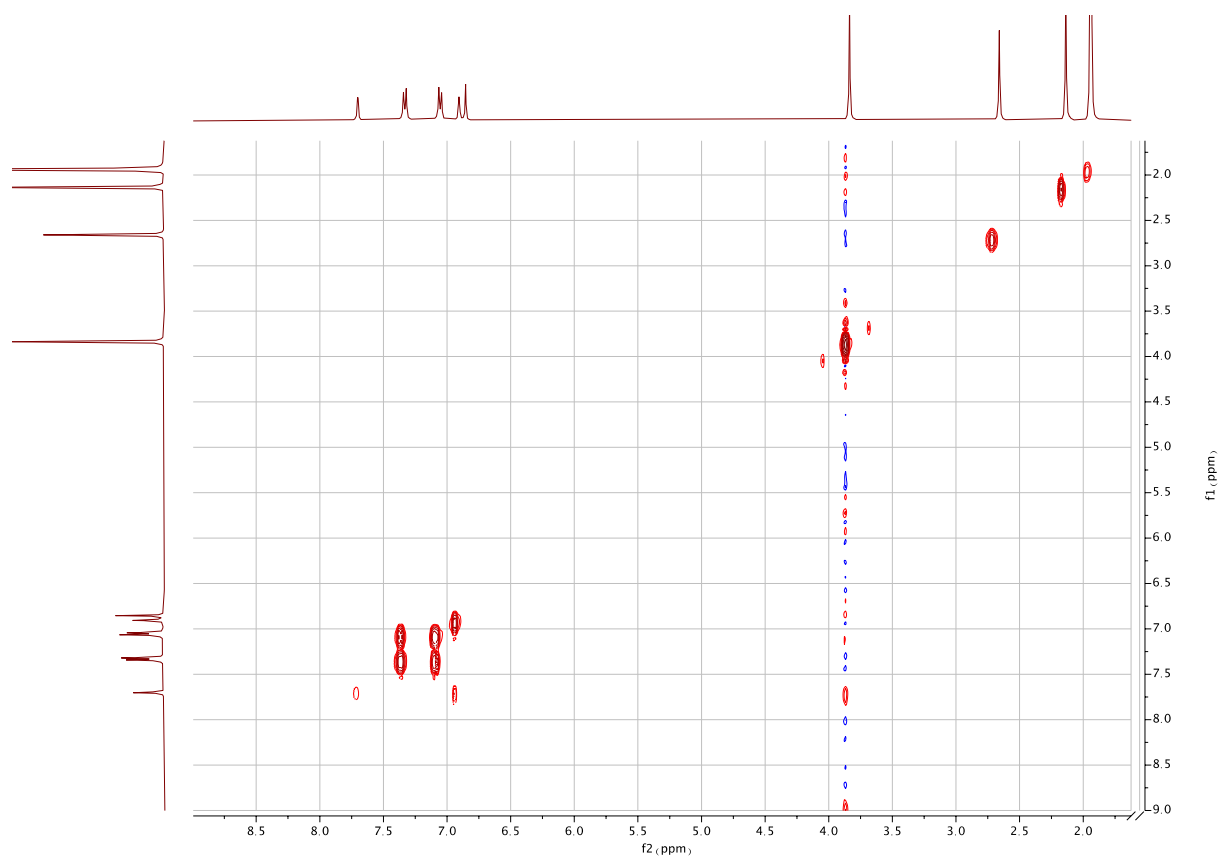


Figure S35. COSY NMR (CD_3CN) spectrum of bis(1,1'-(4-(di-*p*-anisylamino)pyridine-2,6-diyl)bis(3-methylimidazol-2-ylidene))iron(II) bis(hexafluorophosphate) ($[\text{Fe}(\text{daapbmi})_2](\text{PF}_6)_2$).

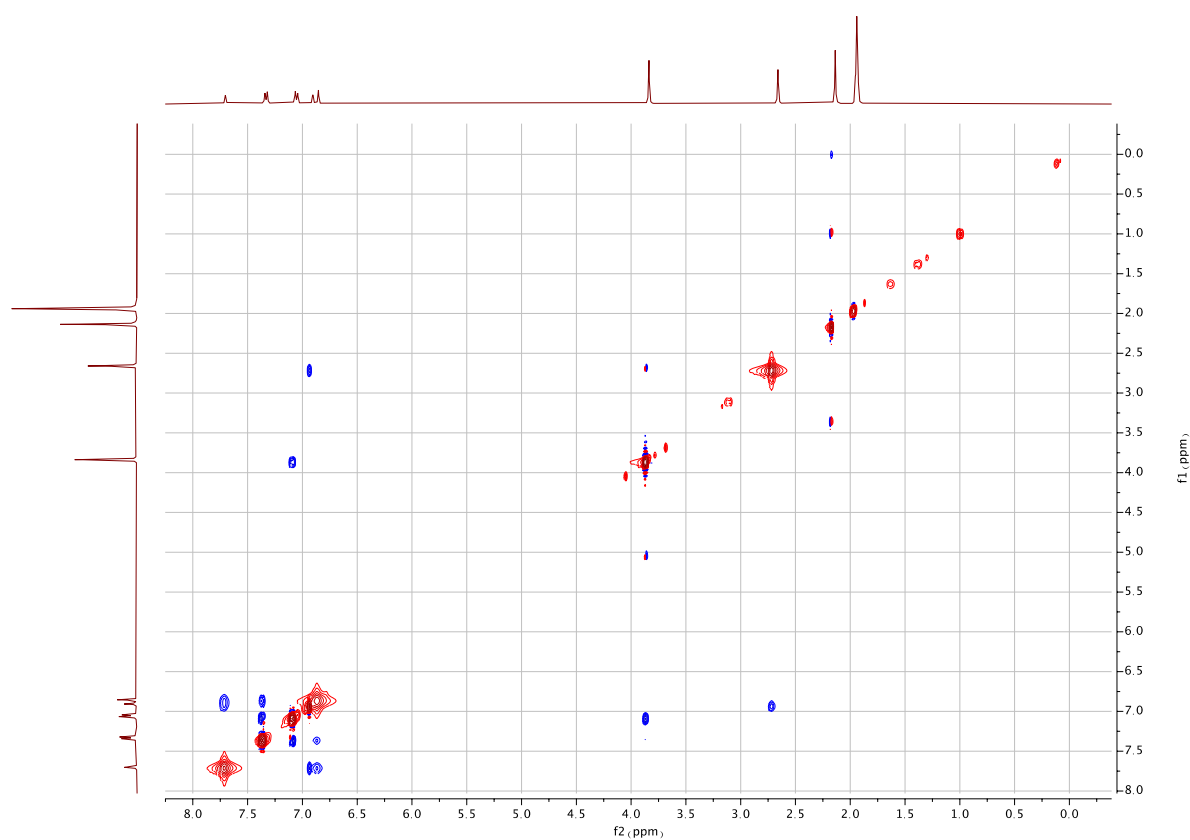


Figure S36. NOSEY NMR (CD_3CN) spectrum of bis(1,1'-(4-(di-*p*-anisylamino)pyridine-2,6-diyl)bis(3-methylimidazol-2-ylidene))iron(II) bis(hexafluorophosphate) ($[\text{Fe}(\text{daapbmi})_2](\text{PF}_6)_2$).

2. X-ray Diffraction Crystallography

All SC-XRD measurements were performed using graphite-monochromatized Mo K α radiation ($\lambda = 0.71073 \text{ \AA}$) using the Agilent Xcalibur Sapphire3 diffractometer high-brilliance I μ S radiation source. Data collections were performed at 295 K for [Fe^{II}(cpbmi)₂](PF₆)₂, [Fe^{II}(cpbmi)(dtapbmi)](PF₆)₂ and [Fe^{II}(daapbmi)₂](PF₆)₂, 150 K for [Fe^{II}(dtapbmi)₂](PF₆)₂ and [Fe^{II}(cpbmi)(daapbmi)](PF₆)₂, and 110 K for [Fe^{III}(daapbmi)₂](K(NO₃)₄). The structures were solved by direct methods and refined by full-matrix least-squares techniques against F² using all data (SHELXT, SHELXS).^[S3] All non-hydrogen atoms were refined with anisotropic displacement parameters if not stated otherwise. The [Fe^{II}(cpbmi)₂](PF₆)₂ crystal was twinned and twin law matrix was applied for the refinement by using OLEX2 software.^[S4] [Fe^{II}(cpbmi)(dtapbmi)](PF₆)₂ was partially twinned and a good solution could not be found. However, the connectivity of the atoms is reliable and resembles the other structures. The crystal structure contains 1.3 HCl, which most likely originates from the use of hydrochloric acid during the work up of the complex. The OLEX2 solvent masking was used to treat diffuse scattering in [Fe^{II}(cpbmi)₂](PF₆)₂. Non-hydrogen atoms were refined anisotropically. Molecular graphics were generated using the software Mercury.^[S5]

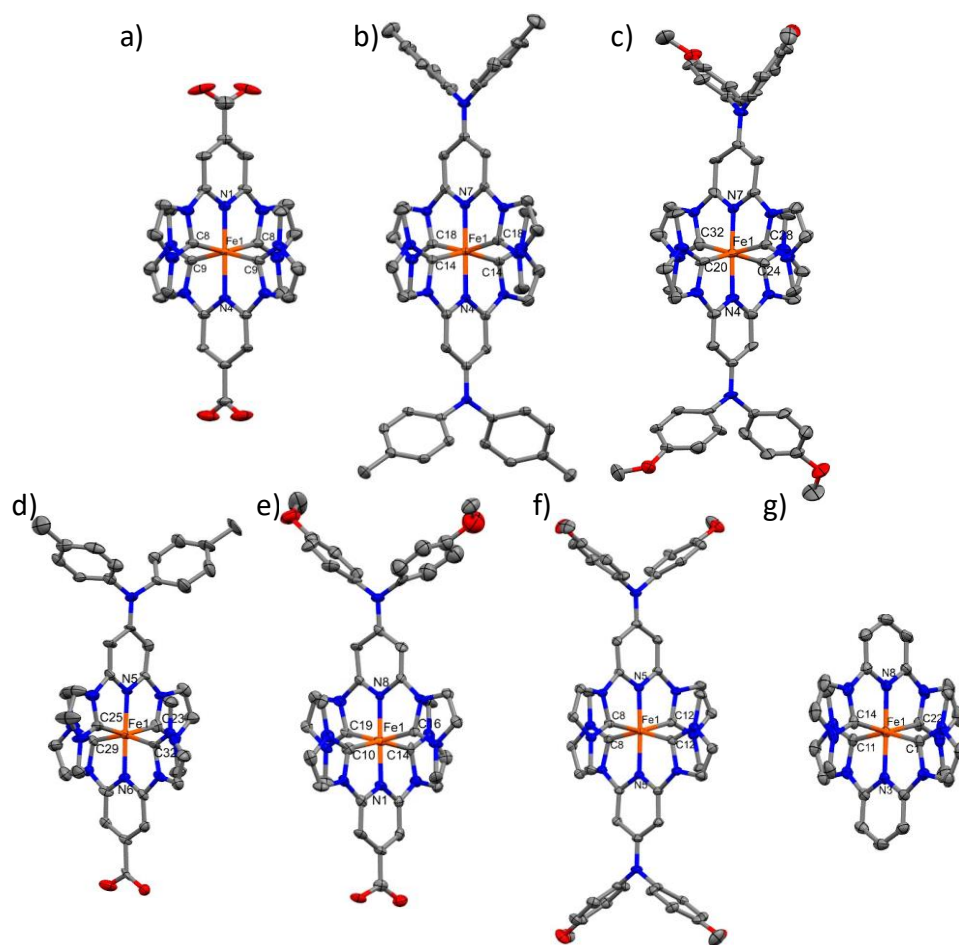


Figure S37. Molecular structure of a) [Fe^{II}(cpbmi)₂](PF₆)₂, b) [Fe^{II}(dtapbmi)₂](PF₆)₂, c) [Fe^{II}(daapbmi)₂](PF₆)₂, d) [Fe^{II}(cpbmi)(dtapbmi)](PF₆)₂, e) [Fe^{II}(cpbmi)(daapbmi)](PF₆)₂, f) [Fe^{III}(daapbmi)₂](K(NO₃)₄) and g) [Fe^{II}(pbmi)₂](PF₆)₂ (from CIF-file^[S6]) with anisotropic displacement ellipsoids at the 30% probability level. Hydrogen atoms, counterions and solvent molecules are omitted for clarity. Displayed atoms are Fe – orange, C – gray, N – blue, O – red.

Table S1. Crystal data and structure refinement for $[\text{Fe}^{\text{II}}(\text{cpbmi})_2](\text{PF}_6)_2$

Empirical formula	$\text{C}_{61}\text{H}_{72}\text{F}_{12}\text{Fe}_2\text{N}_{20}\text{O}_{12.50}\text{P}_2$	
Formula weight	1687.02	
Temperature	295.0 K	
Wavelength	0.71073 Å	
Crystal system	Orthorhombic	
Space group	$\text{C}222_1$	
Unit cell dimensions	$a = 15.2815(10)$ Å	$\alpha = 90^\circ$.
	$b = 16.2362(12)$ Å	$\beta = 90^\circ$.
	$c = 15.2815(10)$ Å	$\gamma = 90^\circ$.
Volume	$3791.5(4)$ Å ³	
Z	2	
Density (calculated)	1.478 Mg/m ³	
Absorption coefficient	0.526 mm ⁻¹	
F(000)	1736	
Crystal size	0.3 x 0.22 x 0.12 mm ³	
Theta range for data collection	3.662 to 24.989°.	
Index ranges	$-18 \leq h \leq 18, 0 \leq k \leq 19, 0 \leq l \leq 18$	
Reflections collected	3349	
Independent reflections	3349 [R(int) = -]	
Completeness to theta = 24.989°	99.6%	
Absorption correction	None	
Max. and min. transmission	1.00000 and 0.72827	
Refinement method	Full-matrix least-squares on F ²	
Data / restraints / parameters	3349 / 51 / 267	
Goodness-of-fit on F ²	1.069	
Final R indices [I > 2σ(I)]	R1 = 0.0702, wR2 = 0.1759	
R indices (all data)	R1 = 0.0844, wR2 = 0.1950	
Absolute structure parameter	-0.10(2)	
Extinction coefficient	n/a	
Largest diff. peak and hole	0.811 and -0.650 e.Å ⁻³	
CCDC nr.	2045349	

Table S2. Crystal data and structure refinement for $[\text{Fe}^{\text{II}}(\text{dtapbmi})_2](\text{PF}_6)_2$

Empirical formula	$\text{C}_{58}\text{H}_{60}\text{C}_{18}\text{F}_{12}\text{FeN}_{12}\text{P}_2$	
Formula weight	1554.57	
Temperature	150 K	
Wavelength	0.71073 Å	
Crystal system	Monoclinic	
Space group	$P 1 2/c 1$	
Unit cell dimensions	$a = 9.7153(5)$ Å	$\alpha = 90^\circ$.
	$b = 18.5782(7)$ Å	$\beta = 93.530(4)^\circ$.
	$c = 19.4324(8)$ Å	$\gamma = 90^\circ$.
Volume	$3500.8(3)$ Å ³	
Z	2	
Density (calculated)	1.475 Mg/m ³	
Absorption coefficient	0.645 mm ⁻¹	
F(000)	1584	
Crystal size	0.3 x 0.16 x 0.08 mm ³	
Theta range for data collection	3.453 to 25.000°.	
Index ranges	$-11 \leq h \leq 11, -22 \leq k \leq 22, -22 \leq l \leq 23$	
Reflections collected	34757	
Independent reflections	6154 [R(int) = 0.0377]	
Completeness to theta = 25.000°	99.7%	
Absorption correction	Semi-empirical from equivalents	
Max. and min. transmission	1.00000 and 0.73415	
Refinement method	Full-matrix least-squares on F ²	
Data / restraints / parameters	6154 / 6 / 482	
Goodness-of-fit on F ²	1.073	
Final R indices [I > 2σ(I)]	R1 = 0.0512, wR2 = 0.1208	
R indices (all data)	R1 = 0.0643, wR2 = 0.1282	
Extinction coefficient	n/a	
Largest diff. peak and hole	0.626 and -0.747 e.Å ⁻³	
CCDC nr.	2045350	

Table S3. Crystal data and structure refinement for $[\text{Fe}^{\text{II}}(\text{daapbmi})_2](\text{PF}_6)_2$

Empirical formula	$\text{C}_{54}\text{H}_{52}\text{F}_{12}\text{FeN}_{12}\text{O}_4\text{P}_2$	
Formula weight	1278.86	
Temperature	295 K	
Wavelength	0.71073 Å	
Crystal system	Triclinic	
Space group	P-1	
Unit cell dimensions	$a = 10.2362(18)$ Å	$\alpha = 117.066(14)^\circ$.
	$b = 17.768(3)$ Å	$\beta = 91.394(12)^\circ$.
	$c = 18.125(2)$ Å	$\gamma = 93.931(13)^\circ$.
Volume	$2922.9(8)$ Å ³	
Z	2	
Density (calculated)	1.453 Mg/m ³	
Absorption coefficient	0.407 mm ⁻¹	
F(000)	1312	
Crystal size	0.18 x 0.14 x 0.09 mm ³	
Theta range for data collection	3.320 to 25.000°.	
Index ranges	-12<=h<=12, -20<=k<=21, -21<=l<=20	
Reflections collected	28517	
Independent reflections	10261 [R(int) = 0.1881]	
Completeness to theta = 25.000°	99.7%	
Absorption correction	Semi-empirical from equivalents	
Max. and min. transmission	1.00000 and 0.52055	
Refinement method	Full-matrix least-squares on F ²	
Data / restraints / parameters	10261 / 0 / 774	
Goodness-of-fit on F ²	0.949	
Final R indices [I>2sigma(I)]	R1 = 0.1010, wR2 = 0.1958	
R indices (all data)	R1 = 0.2894, wR2 = 0.2891	
Extinction coefficient	n/a	
Largest diff. peak and hole	0.547 and -0.348 e.Å ⁻³	
CCDC nr.	2045879	

Table S4. Crystal data and structure refinement for $[\text{Fe}^{\text{II}}(\text{cpbmi})(\text{dtapbmi})](\text{PF}_6)_2$.

Empirical formula	$\text{C}_{41}\text{H}_{39}\text{F}_{12}\text{Fe}\text{N}_{11}\text{O}_2\text{P}_2$	
Formula weight	1107.93	
Temperature	295 K	
Wavelength	0.71073 Å	
Crystal system	Tetragonal	
Space group	P4/n	
Unit cell dimensions	$a = 23.6142(13)$ Å	$\alpha = 90^\circ$.
	$b = 23.6142(13)$ Å	$\beta = 90^\circ$.
	$c = 18.337(2)$ Å	$\gamma = 90^\circ$.
Volume	$10225.3(16)$ Å ³	
Z	8	
Density (calculated)	1.439 Mg/m ³	
Absorption coefficient	0.513 mm ⁻¹	
F(000)	4506	
Crystal size	0.28 x 0.2 x 0.14 mm ³	
Theta range for data collection	3.303 to 24.995°.	
Index ranges	-27<=h<=28, -25<=k<=24, -21<=l<=21	
Reflections collected	50975	
Independent reflections	8998 [R(int) = 0.2243]	
Completeness to theta = 24.995°	99.7%	
Absorption correction	Semi-empirical from equivalents	
Max. and min. transmission	1.00000 and 0.09467	
Refinement method	Full-matrix least-squares on F ²	
Data / restraints / parameters	8998 / 48 / 668	
Goodness-of-fit on F ²	1.039	
Final R indices [I>2sigma(I)]	R1 = 0.1417, wR2 = 0.2967	
R indices (all data)	R1 = 0.2442, wR2 = 0.3565	
Extinction coefficient	n/a	
Largest diff. peak and hole	0.562 and -0.508 e.Å ⁻³	
CCDC nr.	2050281	

Table S5. Crystal data and structure refinement for $[\text{Fe}^{\text{II}}(\text{cpbmi})(\text{daapbmi})](\text{PF}_6)_2$.

Empirical formula	C ₄₁ H ₃₉ F ₁₂ FeN ₁₁ O ₄ P ₂	
Formula weight	1095.62	
Temperature	150 K	
Wavelength	0.71073 Å	
Crystal system	Monoclinic	
Space group	P 1 21/n 1	
Unit cell dimensions	a = 10.9020(9) Å	a = 90°.
	b = 11.0376(8) Å	b = 94.190(8)°.
	c = 39.830(3) Å	g = 90°.
Volume	4780.1(7) Å ³	
Z	4	
Density (calculated)	1.522 Mg/m ³	
Absorption coefficient	0.483 mm ⁻¹	
F(000)	2232	
Crystal size	0.28 x 0.18 x 0.1 mm ³	
Theta range for data collection	3.250 to 24.998°.	
Index ranges	-12 ≤ h ≤ 12, -12 ≤ k ≤ 13, -47 ≤ l ≤ 46	
Reflections collected	52223	
Independent reflections	8387 [R(int) = 0.2107]	
Completeness to theta = 24.998°	99.8%	
Absorption correction	Semi-empirical from equivalents	
Max. and min. transmission	1.00000 and 0.72671	
Refinement method	Full-matrix least-squares on F ²	
Data / restraints / parameters	8387 / 79 / 647	
Goodness-of-fit on F ²	0.997	
Final R indices [I > 2σ(I)]	R1 = 0.1165, wR2 = 0.2807	
R indices (all data)	R1 = 0.2068, wR2 = 0.3436	
Extinction coefficient	n/a	
Largest diff. peak and hole	1.720 and -0.659 e.Å ⁻³	
CCDC		
2070990		

Table S6. Crystal data and structure refinement for $[\text{Fe}^{\text{III}}(\text{daapbmi})_2]\text{K}(\text{NO}_3)_4$

Empirical formula	$\text{C}_{54}\text{H}_{52}\text{FeKN}_{16}\text{O}_{16}$	
Formula weight	1276.06	
Temperature	110(2) K	
Wavelength	0.71073 Å	
Crystal system	Orthorhombic	
Space group	Pccn	
Unit cell dimensions	$a = 22.3522(4)$ Å	$\alpha = 90^\circ$.
	$b = 14.5810(3)$ Å	$\beta = 90^\circ$.
	$c = 18.1566(4)$ Å	$\gamma = 90^\circ$.
Volume	$5917.6(2)$ Å ³	
Z	4	
Density (calculated)	1.432 Mg/m ³	
Absorption coefficient	0.407 mm ⁻¹	
F(000)	2644	
Crystal size	0.1 x 0.1 x 0.05 mm ³	
Theta range for data collection	2.421 to 28.872°.	
Index ranges	-30<=h<=27, -18<=k<=19, -24<=l<=24	
Reflections collected	44581	
Independent reflections	7152 [R(int) = 0.0842]	
Completeness to theta = 25.000°	99.9%	
Absorption correction	Semi-empirical from equivalents	
Max. and min. transmission	1.00000 and 0.86566	
Refinement method	Full-matrix least-squares on F ²	
Data / restraints / parameters	7152 / 0 / 398	
Goodness-of-fit on F ²	1.071	
Final R indices [I>2sigma(I)]	R1 = 0.0678, wR2 = 0.1555	
R indices (all data)	R1 = 0.1097, wR2 = 0.1816	
Extinction coefficient	n/a	
Largest diff. peak and hole	1.008 and -0.666 e.Å ⁻³	
CCDC nr.	2034279	

Table S7. Bond lengths, bond angles and dihedral angles in complexes studied here. See Figure S38 for illustration of planes used to calculate dihedral angles.

Compound	Bond lengths (Å)	Bond angles (°)	Dihedral angles (°) ^a
[Fe^{II}(cpbmi)₂](PF₆)₂	C(8)-Fe(1): 1.961(10)	C(9)#1-Fe(1)-C(8)#1: 91.8(4)	(Ring N1)/(O1-C1- O1): 11.92
	C(9)-Fe(1): 1.925(10)	C(9)-Fe(1)-C(8): 91.8(4) C(9)#1-Fe(1)-C(8): 91.9(4)	(Ring N4)/(O2-C17- O2): 8.65
	Fe(1)-N(4): 1.918(7)	C(9)-Fe(1)-C(8)#1: 91.9(4)	
	Fe(1)-N(1): 1.891(8)	C(9)-Fe(1)-C(9)#1: 158.6(5) N(4)-Fe(1)-C(8)#1: 100.1(3) N(4)-Fe(1)-C(8): 100.1(3) N(4)-Fe(1)-C(9)#1: 79.3(3) N(4)-Fe(1)-C(9): 79.3(3) N(1)-Fe(1)-C(8): 79.9(3) N(1)-Fe(1)-C(8)#1: 79.9(3) N(1)-Fe(1)-C(9): 100.7(3) N(1)-Fe(1)-C(9)#1: 100.7(3) N(1)-Fe(1)-N(4): 180.0 C(14)-N(4)-Fe(1): 121.3(4) C(14)#1-N(4)-Fe(1): 121.3(4)	
[Fe^{II}(dtapbmi)₂](PF₆)₂	Fe(1)-N(7): 1.919(3)	C(19)-N(7)-Fe(1): 121.39(17)	(Ring N4)/N1: 16.07 (Ring N7)/N8: 6.62
	Fe(1)-N(4): 1.910(3)	C(19)#1-N(7)-Fe(1): 121.39(18)	(Ring N4)/(Ring C5): 60.53
	Fe(1)-C(18): 1.947(3)	N(7)-Fe(1)-C(18)#1: 78.77(9)	(Ring N7)/(Ring C22): 63.40
	Fe(1)-C(18)#1: 1.947(3)	N(7)-Fe(1)-C(18): 78.77(9)	
	Fe(1)-C(14):	N(7)-Fe(1)-C(14):	

	1.947(3) Fe(1)-C(14)#1: 1.947(3)	101.01(9) N(7)-Fe(1)-C(14)#1: 101.01(9) N(4)-Fe(1)-N(7): 180.0 N(4)-Fe(1)-C(18)#1: 101.23(9) N(4)-Fe(1)-C(18): 101.23(9) N(4)-Fe(1)-C(14)#1: 78.99(9) N(4)-Fe(1)-C(14): 78.99(9) C(18)-Fe(1)-C(18)#1: 157.54(17) C(14)#1-Fe(1)-C(18)#1: 91.71(13) C(14)-Fe(1)-C(18)#1: 92.56(13) C(14)-Fe(1)-C(18): 91.71(13) C(14)#1-Fe(1)-C(18): 92.55(13) C(14)-Fe(1)-C(14)#1: 157.98(17) C(5)-N(1)-C(5)#1: 117.51 C(5)-N(1)-C(8): 121.25 C(22)-N(8)-C(22)#1: 115.14 C(21)-N(8)-C(22): 122.43	
[Fe^{II}(daapbmi)₂](PF₆)₂	C(17)-N(4): 1.338(10) C(28)-Fe(1): 1.948(10) Fe(1)-N(4): 1.923(6) Fe(1)-N(7): 1.924(7)	N(2)-C(20)-Fe(1): 117.1(6) N(3)-C(20)-Fe(1): 142.9(7) N(5)-C(24)-Fe(1): 113.4(6) N(6)-C(24)-Fe(1): 142.6(7)	(Ring N7)/N1: 18.66 (Ring N7)/N12: 9.78 (Ring N7)/(Ring C48): 79.25 (Ring N7)/(Ring C41): 57.88 (Ring N4)/(Ring C8): 71.34

	C(32)-Fe(1): 1.931(10) C(24)-Fe(1): 1.949(9) C(20)-Fe(1): 1.895(10)	N(8)-C(28)-Fe(1): 115.0(7) N(11)-C(28)-Fe(1): 144.8(7) N(10)-C(32)-Fe(1): 144.6(8) C(20)-Fe(1)-C(24): 157.1(4) C(20)-Fe(1)-C(28): 94.4(4) C(20)-Fe(1)-C(32): 91.3(4) C(20)-Fe(1)-N(4): 78.0(3) C(20)-Fe(1)-N(7): 102.8(3) C(28)-Fe(1)-C(24): 88.8(4) C(32)-Fe(1)-C(24): 94.4(4) C(32)-Fe(1)-C(28): 157.4(4) N(4)-Fe(1)-C(24): 79.1(3) N(4)-Fe(1)-C(28): 99.3(4) N(4)-Fe(1)-C(32): 103.3(4) N(4)-Fe(1)-N(7): 177.6(4) N(7)-Fe(1)-C(24): 100.0(3) N(7)-Fe(1)-C(28): 78.4(4) N(7)-Fe(1)-C(32): 79.0(4) C(5)-N(1)-C(8): 117.61 C(5)-N(1)-C(15): 120.06 C(8)-N(1)-C(15): 122.24 C(41)-N(12)-C(48): 115.55 C(41)-N(12)-C(38):	(Ring N4)/(Ring C5): 68.68
--	--	--	-------------------------------

		123.08 C(38)-N(12)-C(48): 120.69	
[Fe^{II}(cpbmi)(dtapbmi)](PF₆)₂	C(23)-Fe(1): 1.978(11) C(25)-Fe(1): 1.905(12) C(29)-Fe(1): 1.944(10) C(32)-Fe(1): 1.948(12) Fe(1)-N(5): 1.913(7) Fe(1)-N(6): 1.892(8)	N(1)-C(23)-Fe(1): 112.8(8) N(2)-C(23)-Fe(1): 141.8(9) N(3)-C(25)-Fe(1): 116.6(8) N(4)-C(25)-Fe(1): 144.2(9) N(8)-C(29)-Fe(1): 113.5(8) N(9)-C(32)-Fe(1): 113.5(8) N(10)-C(32)-Fe(1): 141.6(8) C(25)-Fe(1)-C(23): 156.9(5) C(25)-Fe(1)-C(29): 93.1(5) C(25)-Fe(1)-C(32): 87.5(5) C(25)-Fe(1)-N(5): 79.1(4) C(29)-Fe(1)-C(23): 93.8(4) C(29)-Fe(1)-C(32): 158.1(4) C(32)-Fe(1)-C(23): 94.2(4) N(5)-Fe(1)-C(23): 78.0(4) N(5)-Fe(1)-C(29): 100.4(4) N(5)-Fe(1)-C(32): 101.2(4) N(6)-Fe(1)-C(23) 99.3(4) N(6)-Fe(1)-C(25):	(Ring N6)/(O1-C40- O2): 2.05 (Ring N5)/N11: 18.30 (Ring N5)/(Ring C5): 71.04 (Ring N5)/(Ring C9): 77.46

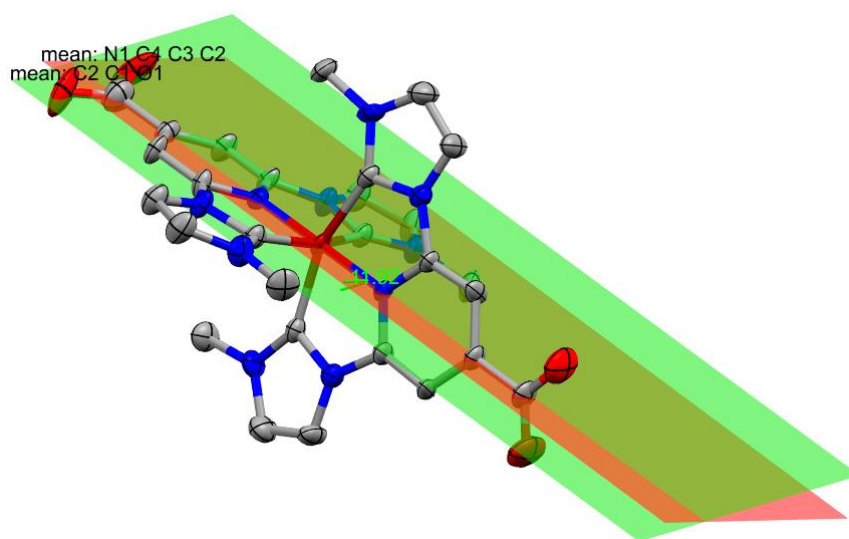
		103.6(4) N(6)-Fe(1)-C(29): 78.9(4) N(6)-Fe(1)-C(32): 79.7(4) N(6)-Fe(1)-N(5): 177.2(4) C(18)-N(5)-Fe(1): 122.9(7) C(19)-N(5)-Fe(1): 120.9(6) C(36)-N(6)-Fe(1): 121.2(7) C(37)-N(6)-Fe(1): 120.2(7) C(5)-N(11)-C(9): 113.88 C(5)-N(11)-C(16): 121.42 C(9)-N(11)-C(16): 124.51	
[Fe^{II}(cpbmi)(daapbmi)](PF₆)₂	Fe(1)-N(1): 1.899(7) Fe(1)-N(8): 1.920(7) Fe(1)-C(10): 1.940(10) Fe(1)-C(14): 1.958(9) Fe(1)-C(16): 1.975(9) Fe(1)-C(19): 1.951(8)	N(1)-Fe(1)-N(8): 178.7(3) N(1)-Fe(1)-C(10): 80.6(4) N(1)-Fe(1)-C(14): 79.5(4) N(1)-Fe(1)-C(16): 100.5(3) N(1)-Fe(1)-C(19): 101.6(3) N(8)-Fe(1)-C(10): 100.7(4) N(8)-Fe(1)-C(14): 99.2(4) N(8)-Fe(1)-C(16): 79.5(3) N(8)-Fe(1)-C(19): 78.4(3) C(10)-Fe(1)-C(14): 159.9(4) C(10)-Fe(1)-C(16): 96.0(4) C(10)-Fe(1)-C(19): 89.8(4) C(14)-Fe(1)-C(16): 90.0(3) C(19)-Fe(1)-C(14):	(Ring N1)/(O1-C1- O2): 9.21 (Ring N8)/N11: 5.53 (Ring N8)/(Ring C28): 76.89 (Ring N8)/(Ring C35): 89.86

		91.8(4) C(19)-Fe(1)-C(16): 157.8(4) C(4)-N(1)-Fe(1): 119.0(6) C(5)-N(1)-Fe(1): 121.4(6) C(23)-N(8)-Fe(1): 121.4(6) C(27)-N(8)-Fe(1): 121.9(6) N(2)-C(10)-Fe(1): 113.1(6) N(3)-C(10)-Fe(1): 146.1(8) N(4)-C(14)-Fe(1): 112.4(7) N(5)-C(14)-Fe(1): 142.6(8) N(6)-C(19)-Fe(1): 141.6(7) N(7)-C(19)-Fe(1): 114.3(6) C(25)-N(11)-C(28): 125.14 C(25)-N(11)-C(35): 118.68 C(28)-N(11)-C(35): 116.16	
[Fe^{III}(daapbmi)₂]K(NO₃)₄	C(8)-Fe(1): 1.963(3) C(12)-Fe(1): 1.947(3) C(13)-N(2): 1.478(4) N(5)-Fe(1): 1.935(3)	N(3)-C(8)-Fe(1): 142.5(2) N(4)-C(8)-Fe(1): 114.2(2) N(2)-C(12)-Fe(1): 142.7(3) N(1)#1-C(12)-Fe(1): 114.5(2) N(5)#1-Fe(1)-N(5): 177.56(16) N(5)#1-Fe(1)-C(12)#1:	(Ring N5)/N6: 3.82 (Ring N5)/(Ring 21): 78.89 (Ring N5)/(Ring 14): 71.15

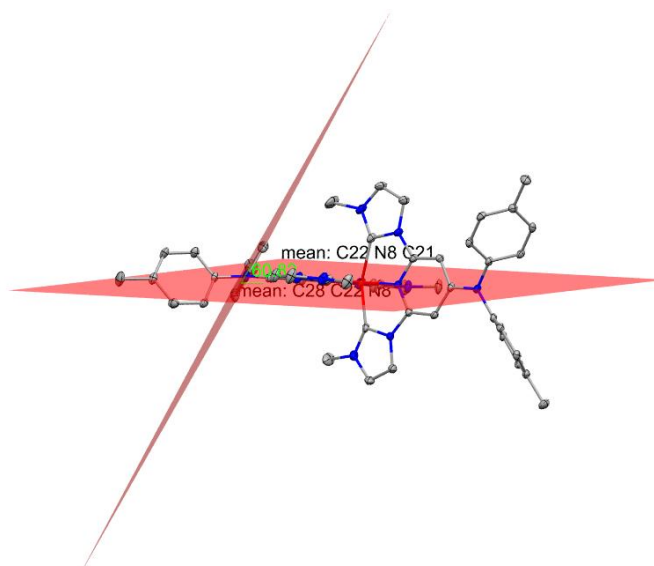
		102.77(12) N(5)-Fe(1)-C(12)#1: 79.03(12) N(5)#1-Fe(1)-C(12): 79.03(12) N(5)-Fe(1)-C(12): 102.77(12) C(12)#1-Fe(1)-C(12): 87.65(19) N(5)#1-Fe(1)-C(8): 99.31(12) N(5)-Fe(1)-C(8): 78.96(12) C(12)#1-Fe(1)-C(8): 157.85(13) C(12)-Fe(1)-C(8): 94.76(13) N(5)#1-Fe(1)-C(8)#1: 78.96(12) N(5)-Fe(1)-C(8)#1: 99.30(12) C(12)#1-Fe(1)-C(8)#1: 94.76(13) C(12)-Fe(1)-C(8)#1: 157.85(13) C(8)-Fe(1)-C(8)#1: 91.25(18) C(14)-N(6)-C(21): 116.64 C(3)-N(6)-C(14): 121.36 C(3)-N(6)-C(21): 121.68	
--	--	--	--

^a Dihedral angles were established by creating averaged planes over a number of atoms, using the function in the mercury program, and measuring the angle between the planes. Planes for aryl rings were created from all six atoms of each respective ring. Plane for carboxylic acid groups were created from the C and two O of the carboxylic acid groups. Planes for the para-substituted nitrogens were created from the nitrogen itself, as well as the three carbons to which it is bonded. See Figure S38 for example illustration of said planes.

a)



b)



c)

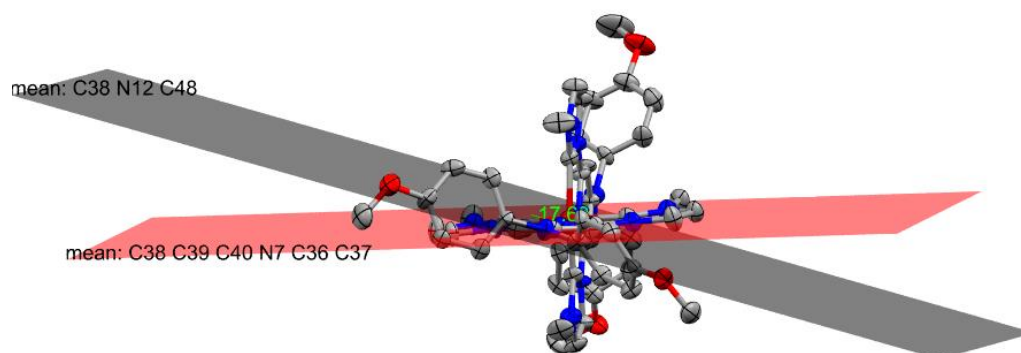


Figure S38. Illustration of planes used to calculate various dihedral angles in complexes, as reported in Table S7. a) angle between pyridine ring and carboxylic acid group, b) angle between pyridine ring and other aryl group on nitrogen, c) angle between pyridine ring and para-substituted nitrogen.

3. Steady-State Absorption Spectroscopy

Steady-state absorption measurements in the UV-VIS region were performed in a Perkin Elmer Lambda 1050 Spectrophotometer. For each complex, careful dilution series were carried out in acetonitrile and buffer (0.1 M TBA methanesulfonate and 0.1 M methanesulfonic acid in acetonitrile). All acetonitrile was collected from dry solvent dispenser (Innovative technology, PS-micro) and stored over 3 Å MS. The complexes were weighting to an accuracy of ~2 µg, then dissolved in the respective solvent system to a known concentration using volumetric flasks. All dilutions were diluted by a factor of 2 compared to the next more concentrated solution, using vollpipettes and volumetric flasks. For all dilution series a minimum of 5 different concentrations spanning at least one order of magnitude were used. Absorbance of all prepared concentrations was measured in a standard quartz-glass cuvette of path length 1 mm (Hellma – High Performance Quartz Glass). For reference the same cuvette with pure solvent was used for each dilution series. Extinction coefficients were evaluated where appropriate by performing a linear fit to the absorbance as a function of concentration for each wavelength, after the reference measurement had been subtracted. The pH-dependent steady-state absorption spectra were measured with a Probe Drum Lab-in-a-box system in connection with a Thermo Scientific Orion Star A211 pH meter. The pH meter was calibrated with two standard buffers (pH = 4.01 & 7.00) before the measurement.

Spectral changes due to protonation/deprotonation were investigated by titration series reported here. To confirm the observation of shifting absorption spectra, dilution series of complexes featuring carboxylic acid groups in “dry” acetonitrile (collected from dry solvent dispenser (Innovative technology, PS-micro) and stored over 3 Å MS) were performed. As seen in Figure S39, the dilution series clearly show the change in absorption wavelength and spectral shape when the concentration is changed. Initially it was assumed that the water content in the acetonitrile was negligible. However, Karl Fischer titration indicated that the acetonitrile contained water up to 175 ppm in mass, which equals to 7.6 mM. Thus, the hypothesis that water in acetonitrile acted as a base and deprotonated carboxyl groups was suggested based on previous observations reported for $[\text{Fe}(\text{cpbmi})_2](\text{PF}_6)_2$.^[S7]

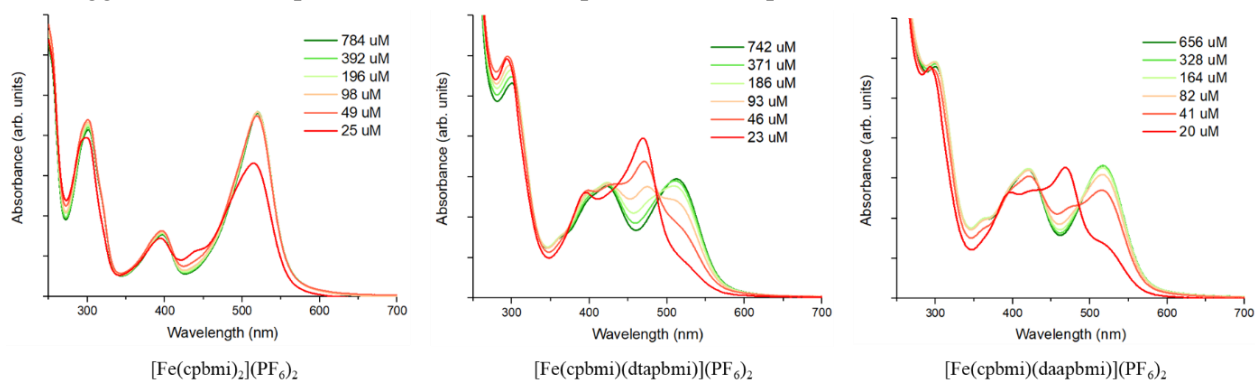


Figure S39: Dilution series of complexes featuring carboxylic acid groups in acetonitrile. For these complexes ($[\text{Fe}(\text{cpbmi})_2](\text{PF}_6)_2$, $[\text{Fe}(\text{cpbmi})(\text{dtapbmi})](\text{PF}_6)_2$ and $[\text{Fe}(\text{cpbmi})(\text{daapbmi})](\text{PF}_6)_2$) a clear shift in the shape of the absorption spectra are visible when going towards lower concentrations. All spectra are divided by the respective complex concentration to be able to compare the spectral shifts.

To prove the acidochromism hypothesis (the effect of absorption spectra changing with pH), a pH-titration of the complex yielding the largest shift in absorption spectrum, $[\text{Fe}(\text{cpbmi})(\text{dtapbmi})](\text{PF}_6)_2$, was performed. In Figure S40, the absorbance of this complex at different pH is shown. At low pH-values, where the complex would be protonated, the spectra resemble the absorption spectra measured for the same complex at high concentrations in pure acetonitrile (Figure S39, $[\text{Fe}(\text{cpbmi})(\text{dtapbmi})](\text{PF}_6)_2$). At high pH-values where the complex would be deprotonated, the spectra somewhat resemble the spectrum measured at the lowest concentration in Figure S39 ($[\text{Fe}(\text{cpbmi})(\text{dtapbmi})](\text{PF}_6)_2$). This behaviour indeed fit to the acidochromism hypothesis, since at

lower concentration the ratio of water molecules to complex will be higher which should yield a larger fraction of deprotonated complexes, as water acts as a base.

In Figure S40, the four isosbestic points (at 371 nm, 406 nm, 435 nm and 500 nm) indicate that the change in pH indeed makes the complex interconvert between two distinct species. Since the pKa of aromatic carboxylic acids vary between 2 to 5,^[S2] the two species are assigned as the complex in its acid form together with its corresponding base. Figure S39 ([Fe(cpbmi)(dtapbmi)](PF₆)₂) shows an equilibrium between these species, that based on the spectra in Figure S40 lies quite close to 100% protonated species at high [Fe(cpbmi)(dtapbmi)](PF₆)₂ concentration, but shifts towards a larger fraction of the deprotonated species as the concentration of [Fe(cpbmi)(dtapbmi)](PF₆)₂ is lower.

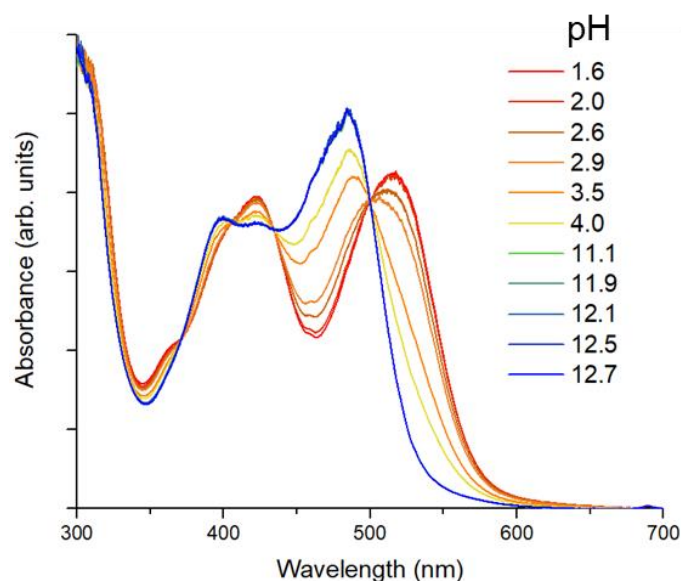


Figure S40. pH-titration of complex [Fe(cpbmi)(dtapbmi)](PF₆)₂ in a 1:1 acetonitrile-water-mixture. The titration was carried out by adding sodium hydroxide or trifluoroacetic acid at volumes small enough to neglect change in concentration of the complex. For each measured absorbance curve, the pH of the solution was measured.

By using a buffer system keeping the solution with excess amount of acid, the complexes will remain only in the protonated state in solution. Additionally, the use of a high concentration of salt (TBA methanesulphonate) in solution, compared to the measured species, allowed for a constant ionic strength ($I = 0.1$ M), as has been shown to be of importance when probing ionic species.^[S8] As a result, no change in absorption spectra was observed.

4. Electrochemistry and Spectroelectrochemistry

Cyclic voltammetry, differential pulse voltammetry and controlled-potential electrolysis were performed using an Autolab PGSTAT302 potentiostat with a GPES electrochemical interface (Eco Chemie). The working electrode was a glassy carbon disc (1.6 mm diameter) that was freshly polished with alumina paste prior to all measurements. A glassy carbon rod in a compartment separated from the bulk solution by a fritted disk was used as counter electrode. The reference electrode was a non-aqueous Ag⁺/Ag electrode (0.010 M AgNO₃ in acetonitrile) that was calibrated with reference to the ferrocenium ion/ferrocene couple (Fc⁺⁰). All solutions were prepared from dry acetonitrile (Sigma-Aldrich, spectroscopic grade, dried with MS 3 Å) with 0.1 M tetrabutylammonium hexafluorophosphate (Fluka, electrochemical grade) as supporting electrolyte that was dried in vacuo at 85 °C. During these measurement conditions all complexes are in their protonated form, verified by the shape of their respective absorption spectra.

UV-Vis spectroelectrochemical experiments were performed in a custom build quartz glass cell (1 mm optical path length) using a platinum mesh as the working electrode and the same counter and reference electrodes used for voltammetry. Spectra were recorded on an Agilent 8453 diode array spectrophotometer.

The cyclic voltammetry and spectroelectrochemistry data of $[\text{Fe}(\text{daapbmi})_2]^{2+}$ and $[\text{Fe}(\text{cpbmi})(\text{daapbmi})]^{2+}$ are shown in Figure S41 and S42 respectively.

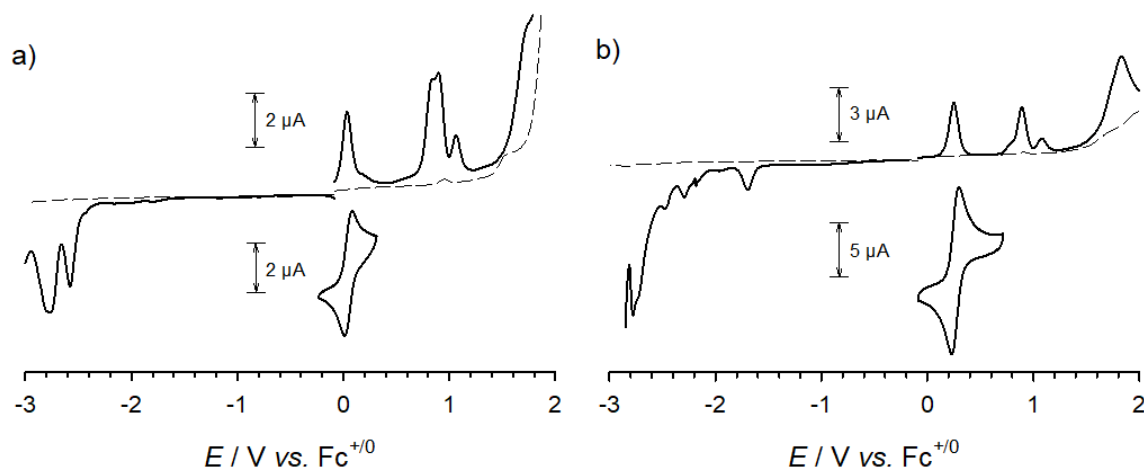


Figure S41. Differential pulse voltammograms and cyclic voltammograms (100 mVs^{-1} , reversible waves only) of a) $[\text{Fe}(\text{daapbmi})_2]^{2+}$ (0.75 mM) and b) $[\text{Fe}(\text{cpbmi})(\text{daapbmi})]^{2+}$ (1.45 mM) in acetonitrile with 0.1 M TBAPF₆.

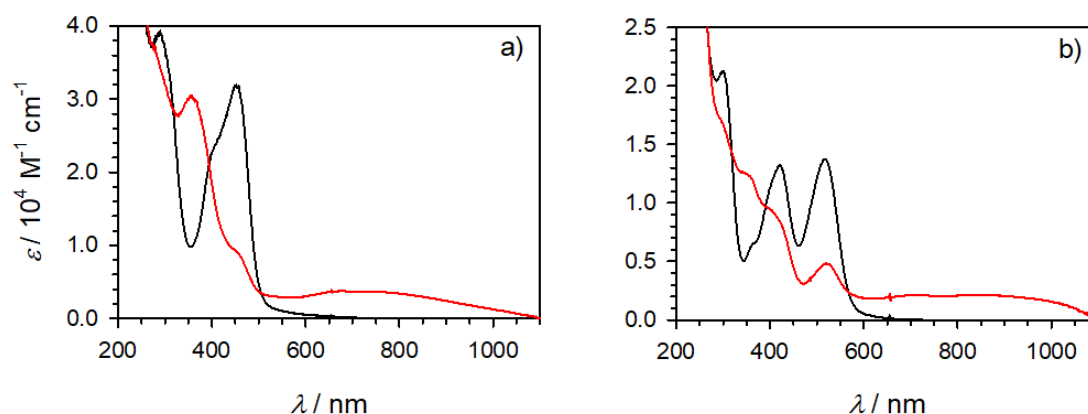


Figure S42. Spectroelectrochemistry in acetonitrile with 0.1 M TBAPF₆. a) $[\text{Fe}(\text{daapbmi})_2]^{2+}$ (—) and product spectrum after oxidation at 0.5 V (—). b) $[\text{Fe}(\text{cpbmi})(\text{daapbmi})]^{2+}$ (—) and product spectrum after oxidation at 0.75 V (—). MLCT features can be seen for the black spectra $\sim 460 \text{ nm}$ in a) and $\sim 520 \text{ nm}$ in b). LMCT features can be seen for the red spectra $\sim 700 \text{ nm}$ in a) and $\sim 800 \text{ nm}$ in b).

Also cyclic voltammetry were performed for dyes adsorbed on a TiO₂ film fabricated by using the exact same procedure as for the DSSC fabrication, see section SI.9. The electrolyte used in the experiment was 0.1 M TBAPF₆ in acetonitrile, the reference electrode was Ag⁺/AgNO₃ and the sweep rate was 20 mV s^{-1} . The result for $[\text{Fe}(\text{cpbmi})_2](\text{PF}_6)_2$, $[\text{Fe}(\text{cpbmi})(\text{dtapbmi})](\text{PF}_6)_2$ and $[\text{Fe}(\text{cpbmi})(\text{daapbmi})](\text{PF}_6)_2$ are shown in Figure S43. For all complexes, the oxidation potential is shifted compared to the value in solution. For $[\text{Fe}(\text{cpbmi})_2](\text{PF}_6)_2$ the oxidation potential shifted the most (0.45 V in solution compared to 0.22 V on film, both vs. Fc).

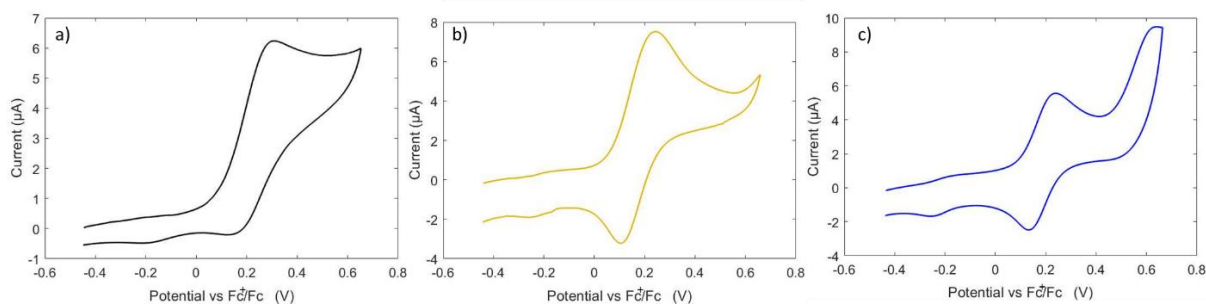


Figure S43. Cyclic voltammograms (using 20 mV s^{-1} sweep rate) of a) $[\text{Fe}(\text{cpbmi})_2]^{2+}$, b) $[\text{Fe}(\text{cpbmi})(\text{dtapbmi})]^{2+}$ and c) $[\text{Fe}(\text{cpbmi})(\text{daapbmi})]^{2+}$ adsorbed on TiO_2 films used for DSSC fabrication in acetonitrile with 0.1 M TBAPF_6 . The reference electrode used for the measurements was $\text{Ag}^+/\text{AgNO}_3$, but potentials are here reported vs. Fc.

The oxidized dye spectra of $[\text{Fe}(\text{cpbmi})(\text{dtapbmi})](\text{PF}_6)_2$ and $[\text{Fe}(\text{cpbmi})(\text{daapbmi})](\text{PF}_6)_2$ adsorbed on TiO_2 films were obtained by chemically oxidizing the complexes when adsorbed to the TiO_2 particles. The TiO_2 films were fabricated using the exact same procedure as for the DSSC fabrication, see section SI.9. The films were sensitized by immersing them in $\sim 0.1 \text{ mM}$ dye solution in acetonitrile over night. After rinsing with dry acetonitrile, the films were immersed in 10 ml of acetonitrile and to the solution was dropwise added a solution of NOPF_6 (0.33 M in acetonitrile) until clear change in colour to green was observed over the whole film (approximately 0.2 ml). The films were then rinsed again with acetonitrile and the steady state absorption spectra were measured on an Agilent 8453 UV-Visible Spectroscopy System. The obtained spectra are shown in Figure S44 together with the measured oxidized dye spectra from spectroelectrochemistry of the complexes in solution in order to compare the spectral features.

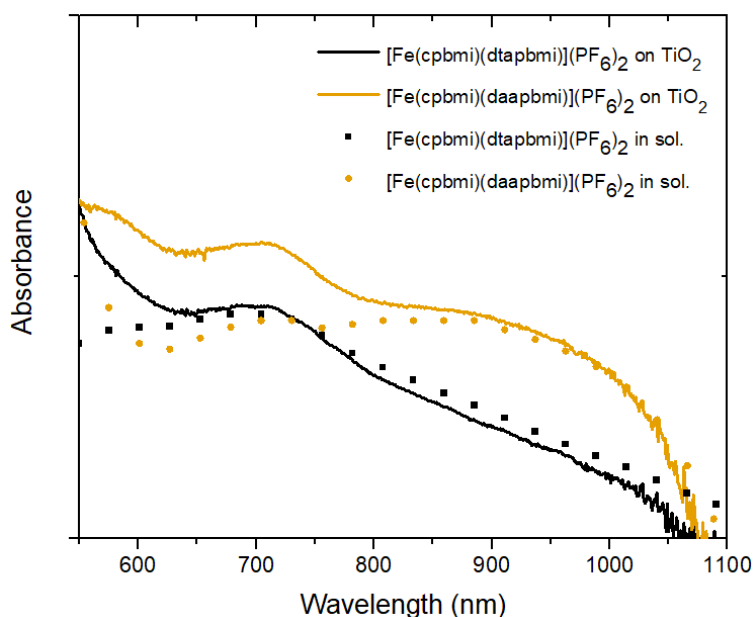


Figure S44. Steady state absorption spectra of the oxidized dyes $[\text{Fe}(\text{cpbmi})(\text{dtapbmi})]^{2+}$ and $[\text{Fe}(\text{cpbmi})(\text{daapbmi})]^{2+}$ adsorbed on TiO_2 . Films were prepared according to the procedure outlined in section SI.9, sensitized in 0.1 mM dye solution in acetonitrile over night and then chemically oxidized by NOPF_6 . From the oxidized dye spectra, the background of the TiO_2 film absorption have been subtracted. For comparison, the oxidized dye spectra obtained for the complexes in solution from spectroelectrochemistry are included.

In Figure S44 it is clearly seen that the absorption of the oxidized dyes on film and in solution are very similar. The small differences are attributed mainly to scattering from the TiO_2 film.

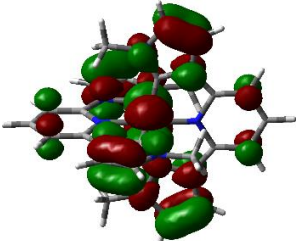
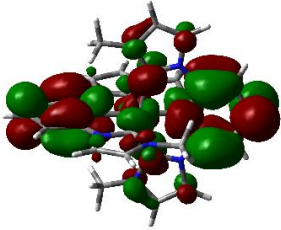
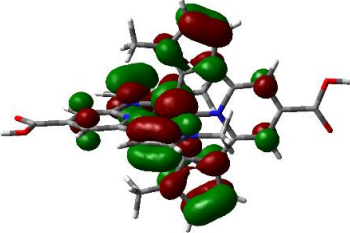
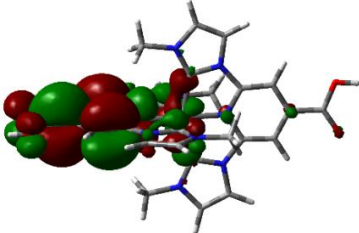
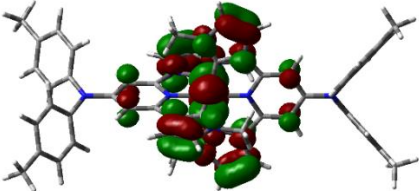
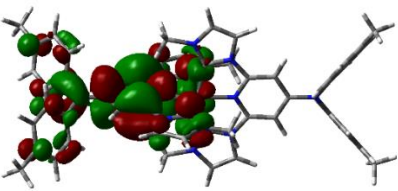
5. Quantum Chemical Calculations

Density functional theory calculations were performed by using the program Gaussian 09^[S9] at supercomputer Aurora in Lund. Molecular ground state structures were optimized by using the B3LYP*^[S10] level of theory with the basis set 6-311G(d, p)^[S11,S12], modelled in an empirical solvent model of acetonitrile. The vertical triplet states and optimized triplet states were calculated by unrestricted DFT from the optimized singlet ground state geometry, using the same functional, basis set and solvent model. Kohn-Sham orbitals and spin density contours were visualized in the program GaussView.

Table S8 shows a pictorial overview of the optimized ground state structures and frontier orbitals of all investigated complexes, from DFT calculations. For all complexes the HOMOs are similar: they all feature a mixing of the Fe t_{2g} orbital with a π^* -orbital on the imidazole moieties. Some mixing with the pyridine moiety can also be seen, but inclusion of orbitals coming from the substituents in the para-position on the pyridine ring is not observed. Due to the large Fe-centred orbital contributions, all HOMOs are considered metal-centred.

For the LUMOs, the orbital contribution from Fe t_{2g} is much less and these orbitals are considered ligand-centred. The LUMOs are π^* -orbitals with highest density on the pyridine ring. For the heteroleptic complexes ([Fe(cpbmi)(dtapbmi)]²⁺ and [Fe(cpbmi)(daapbmi)]²⁺), the LUMO is always centred on the ligand with the carboxylic acid group. For the homoleptic complex [Fe(cpbmi)₂]²⁺, as reported previously, the LUMO and LUMO+1 are degenerated, see Figure S45.^[S11] The orbitals extend to one ligand each, meaning that there is no preferential ligand of lower energy such as for the heteroleptic complexes.

Table S8. A compilation of the frontier molecular orbitals for all complexes in their respective optimized ground states. The calculations were performed on the B3LYP* level of theory with the 6-311G(d, p) basis set, modelled in an empirical solvent model of acetonitrile.

Molecule	HOMO	LUMO
[Fe(pbmi) ₂] ²⁺		
[Fe(cpbmi) ₂] ²⁺		
[Fe(dtapbmi) ₂] ²⁺		

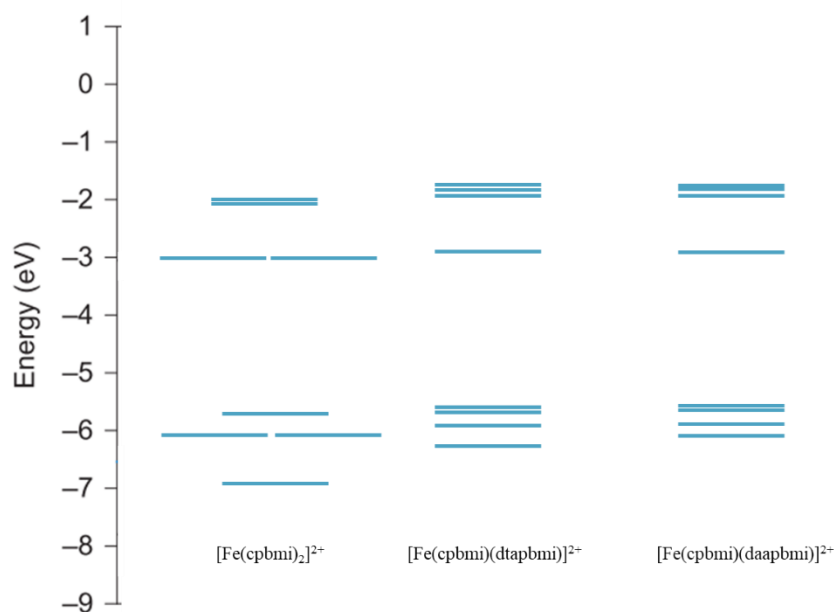
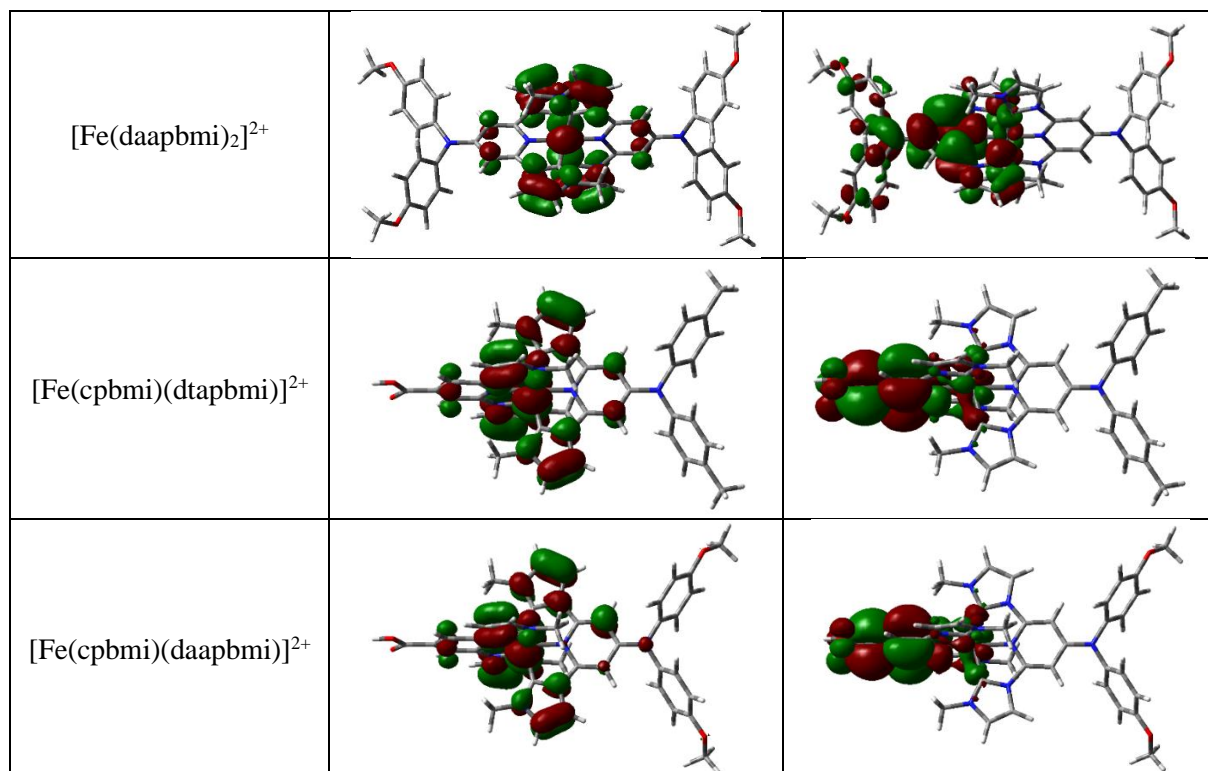


Figure S45. Orbital energies of the four highest occupied and four lowest unoccupied orbitals of complexes featuring carboxylic acid groups ($[\text{Fe}(\text{cpbmi})_2]^{2+}$, $[\text{Fe}(\text{cpbmi})(\text{dtapbmi})]^{2+}$ and $[\text{Fe}(\text{cpbmi})(\text{daapbmi})]^{2+}$) in their optimized ground states. The calculations were performed on the B3LYP* level of theory with the 6-311G(d, p) basis set, modelled in an empirical solvent model of acetonitrile.

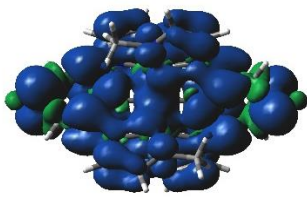
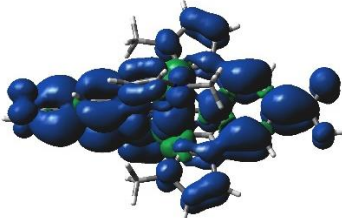
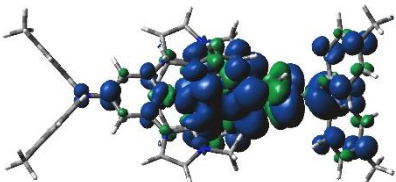
From the vertical calculated triplet states at the ground state geometry, the character of the lowest accessible triplet states were determined. This was judged mainly by looking at the Mulliken spin density on Fe (which for all were close to 1, see Table S9) and the spin density contour plots in Table S10. The distance in energy of the triplet states from the corresponding ground state are depicted in Table S9. These show a similar result of $[\text{Fe}(\text{cpbmi})(\text{dtapbmi})]^{2+}$ and $[\text{Fe}(\text{cpbmi})(\text{daapbmi})]^{2+}$ compared to $[\text{Fe}(\text{cpbmi})_2]^{2+}$. For the homoleptic complexes

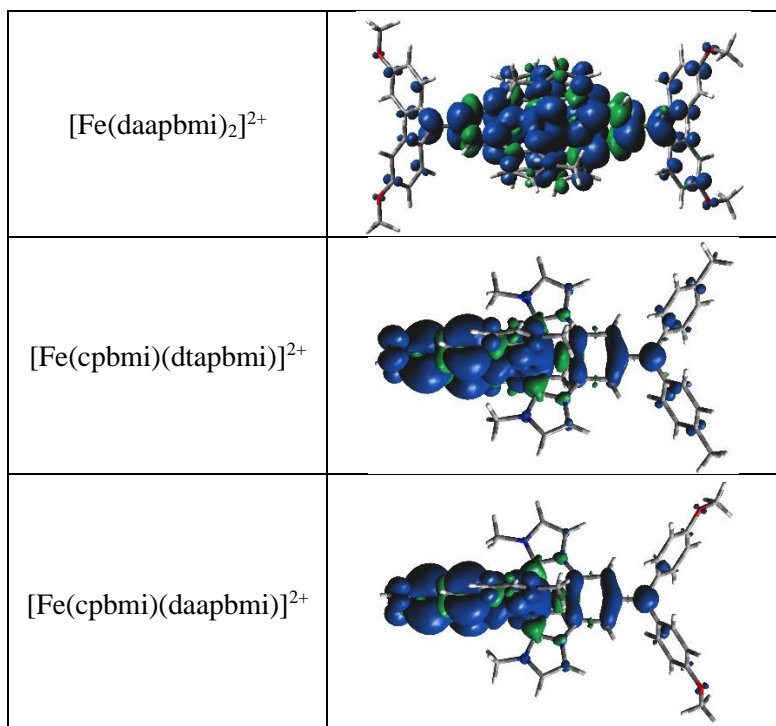
$[\text{Fe}(\text{dtapbmi})_2]^{2+}$ and $[\text{Fe}(\text{daapbmi})_2]^{2+}$, the vertical energy is larger also compared to parent complex $[\text{Fe}(\text{pbmi})_2]^{2+}$.

Table S9. Characteristics of the calculated lowest triplet state at same geometry as the optimized ground state. The calculations were performed on the B3LYP* level of theory with the 6-311G(d, p) basis set, modelled in an empirical solvent model of acetonitrile.

Molecule	Mulliken Spin Density on Fe	Character of State	Vertical Energy from ^1GS (eV)
$[\text{Fe}(\text{pbmi})_2]^{2+}$	0.989	MLCT	2.188
$[\text{Fe}(\text{cpbmi})_2]^{2+}$	0.997	MLCT	1.697
$[\text{Fe}(\text{dtapbmi})_2]^{2+}$	0.982	MLCT	2.354
$[\text{Fe}(\text{daapbmi})_2]^{2+}$	0.998	MLCT	2.407
$[\text{Fe}(\text{cpbmi})(\text{dtapbmi})]^{2+}$	1.054	MLCT	1.741
$[\text{Fe}(\text{cpbmi})(\text{daapbmi})]^{2+}$	1.055	MLCT	1.727

Table S10. Spin density contour plots for all complexes in their lowest energy triplet state at same geometry as the optimized ground state. The calculations were performed on the B3LYP* level of theory with the 6-311G(d, p) basis set, modelled in an empirical solvent model of acetonitrile.

Molecule	Triplet Spin Density
$[\text{Fe}(\text{pbmi})_2]^{2+}$	
$[\text{Fe}(\text{cpbmi})_2]^{2+}$	
$[\text{Fe}(\text{dtapbmi})_2]^{2+}$	



Even though the lowest accessible triplet at the ground state geometry is the $^3\text{MLCT}$ state, this is not the overall lowest triplet state. From the optimized triplet geometries presented in Table S11, we see that the optimized ^3MC is still ~ 0.2 eV lower in energy than the optimized $^3\text{MLCT}$ state. The character of the optimized triplet states were confirmed by looking at the Mulliken spin density on the Fe atom, which for the $^3\text{MLCT}$ state is close to 1 but for the ^3MC state is closer to 2.

Table S11. Optimized triplet geometries for the two new sensitizers for DSSC application, $[\text{Fe}(\text{cpbmi})(\text{dtapbmi})]^{2+}$ and $[\text{Fe}(\text{cpbmi})(\text{daapbmi})]^{2+}$. Both the $^3\text{MLCT}$ and ^3MC states were optimized, corroborated by the spin density on the Fe atom. Their relative energy alignment between the states are given in the table. The calculations were performed on the B3LYP* level of theory with the 6-311G(d, p) basis set, modelled in an empirical solvent model of acetonitrile.

Optimized state	$[\text{Fe}(\text{cpbmi})(\text{dtapbmi})]^{2+}$		$[\text{Fe}(\text{cpbmi})(\text{daapbmi})]^{2+}$	
	Mulliken spin density on Fe	Relative energy (eV)	Mulliken spin density on Fe	Relative energy (eV)
^1GS	0	0	0	0
^3MC	2.10	1.25	2.10	1.24
$^3\text{MLCT}$	1.06	1.45	1.06	1.44

6. fs-Transient Absorption Spectroscopy

Transient absorption (TA) spectroscopy was performed using an in-house built setup. The basis of this setup is a Spitfire Pro XP (Spectra Physics) laser amplifier system that produces ~ 80 fs pulses at a central wavelength of 796 nm at 1 kHz repetition rate. The amplifier output is divided into two parts that each pump a collinear optical parametric amplifier (TOPAS-C, Light Conversion). One of the TOPAS generates the pump beam (wavelength set to the absorption maximum of each sample), while the other one generates a NIR beam (1350 nm) that is focused onto a 5 mm CaF_2 crystal to generate a supercontinuum probe beam. The delay between pump and probe beams is introduced by a computer-controlled delay stage (Aerotech) placed in the probe beam's path. After supercontinuum generation the

probe pulses are split into two parts: the former being focused to $\sim 100 \mu\text{m}$ spot size and overlapping with the pump pulse in the sample volume, and the latter serving as a reference. After passing the sample the probe beam is collimated again and relayed onto the entrance aperture of a prism spectrograph. The reference beam is directly relayed on the spectrograph. Both beams are then dispersed onto a double photodiode array, each holding 512 elements (Pascher Instruments). The intensity of excitation pulses was set to 1 mW corresponding to $\sim 10^{14}$ photons per pulse per cm^2 and spot-size ratio of pump- and probe-pulse was $\sim 1:30$ in area. Mutual polarization between pump and probe beams was set to the magic angle (54.7°) by placing a Berek compensator in the pump beam. Time-resolution of the setup after dispersion correction is estimated to be 80-100 fs.

Sample solutions were filled in 1 mm optical path length cuvettes (Hellma – Optical Special Glass) and measurements were performed at room temperature. The solvents used were a buffer solution consisting of 0.1 M tert-butyl ammonium (TBA) methanesulfonate and 0.1 M methanesulfonic acid in dry acetonitrile, or only dry acetonitrile. The acetonitrile used in the experiments came from a dispenser where it is degassed with N_2 -gas and stored under an atmosphere of N_2 . Solvents were not further degassed after being dispensed. Film samples were prepared according to the procedure in section S.8. The measured samples were translated after each scan to avoid photodegradation. To check for stability of the sample, steady-state absorption spectra were measured before and after TA experiments. The result for $[\text{Fe}(\text{cpbmi})(\text{dtapbmi})](\text{PF}_6)_2$ is shown in Figure S53.

Before analysis the measured data were corrected for group velocity dispersion (GVD – “chirp”) using the in-house software KiMoPack or the software from Pascher Instruments. Data were fitted by global analysis where the signals at all wavelengths are fitted with the same sum of exponential decay components without assuming any model. For that, we used the in-house software KiMoPack or the software from Pascher Instruments. Decay associated spectra (DAS) are obtained from the wavelength dependent pre-exponential factor for each decay component given by the global analysis.

To further elaborate on the different decay components fitted to the systems on TiO_2 films in acetonitrile more details are given here. The datasets of $[\text{Fe}(\text{cpbmi})(\text{dtapbmi})](\text{PF}_6)_2$ and $[\text{Fe}(\text{cpbmi})(\text{daapbmi})](\text{PF}_6)_2$ adsorbed on TiO_2 films in acetonitrile were fitted by four components, out of which one is non-decaying (nd) within the timeframe of the experiment. In Figure S46 selected kinetics for $[\text{Fe}(\text{cpbmi})(\text{daapbmi})](\text{PF}_6)_2$ are shown together with the decay associated spectra (DAS) from the fit.

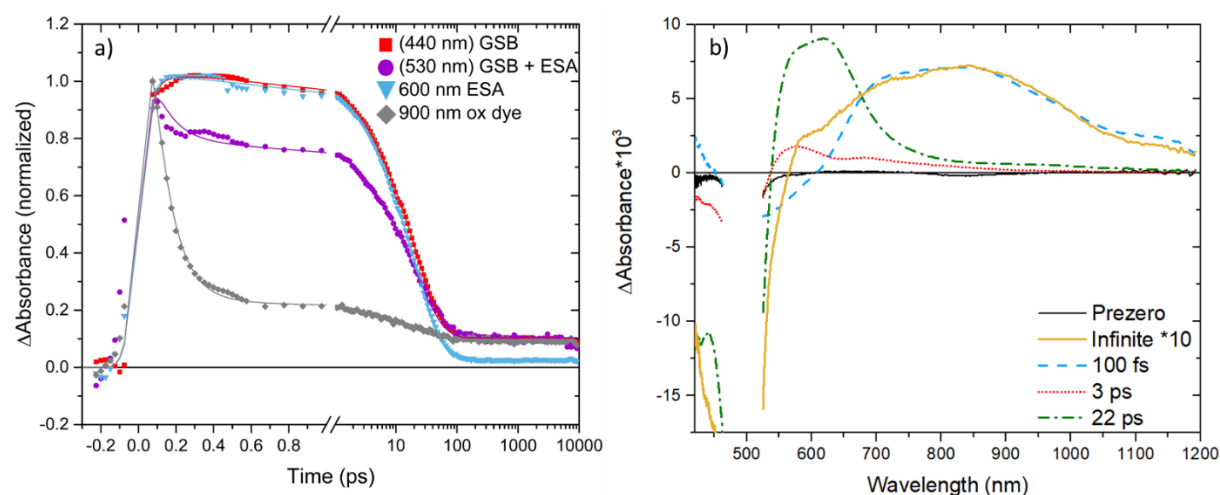


Figure S46. a) Selected TA kinetics of $[\text{Fe}(\text{cpbmi})(\text{daapbmi})](\text{PF}_6)_2$ adsorbed on meso-porous TiO_2 films in acetonitrile (excitation wavelength 480 nm). Kinetics are normalized and averaged, kinetics with a parenthesis in the legend have also been inverted. Symbols represent the measured data and solid lines are fits, resulting from the global fit to the data. b) Decay associated spectra from the global fit to the dataset of $[\text{Fe}(\text{cpbmi})(\text{daapbmi})](\text{PF}_6)_2$ adsorbed on meso-porous TiO_2 films in acetonitrile. The label of each component line refers to the fitted lifetime of that component. Data were chirp corrected, cut to remove scatter and an artefact region of ± 80 fs around time zero was omitted. Decay associated spectra are plotted to scale unless otherwise is noted in the legend. GSB – ground state bleach, ESA – excited state absorption.

The similarity of the excited state absorption when the complexes are adsorbed on TiO₂ in acetonitrile and when they are in solution can be seen in Figure S47. The similarity is the basis for assigning the excited state in the film data to ³MLCT.

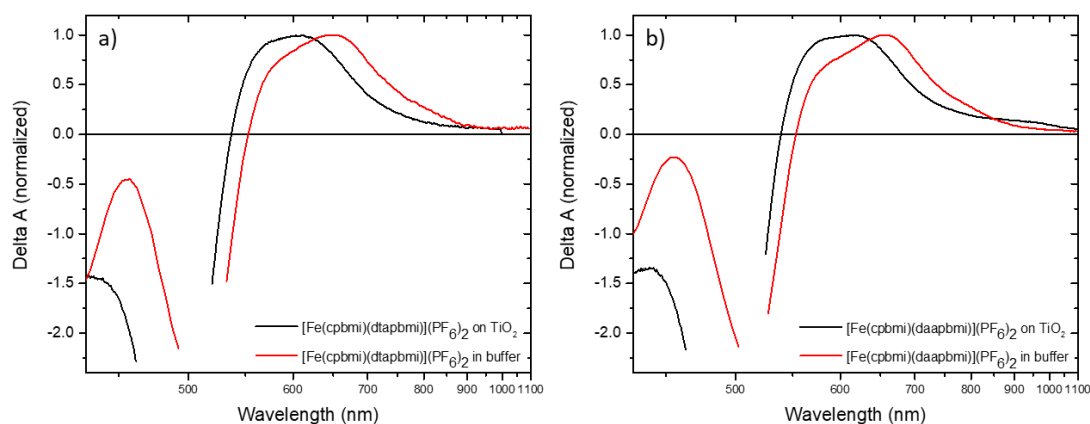


Figure S47. TA spectra comparing the excited state absorption region at 1 ps after excitation for a) [Fe(cpbbi)(dtapbbi)](PF₆)₂ and b) [Fe(cpbbi)(daapbbi)](PF₆)₂. The TA spectra have been normalized for easier comparison between the complex in buffer solution (0.1 M TBA methanesulfonate and 0.1 M methanesulfonic acid in acetonitrile) or adsorbed on a TiO₂ mesoporous film in acetonitrile. The excitation wavelengths were set to 515 nm for the measurements in buffer and 490/480 nm for the measurements on TiO₂ in acetonitrile. All spectra have been cut to remove excitation scatter, as well as chirp (group velocity dispersion) and background corrected.

In Figure S48 the decay associated spectra of the 100 fs and the non-decaying components for both complexes are plotted together with the oxidized dye spectrum from spectroelectrochemistry. All spectra are normalized for comparability. It is apparent that the positive spectral components all resemble one another, and are the spectral features of the respective oxidized dyes.

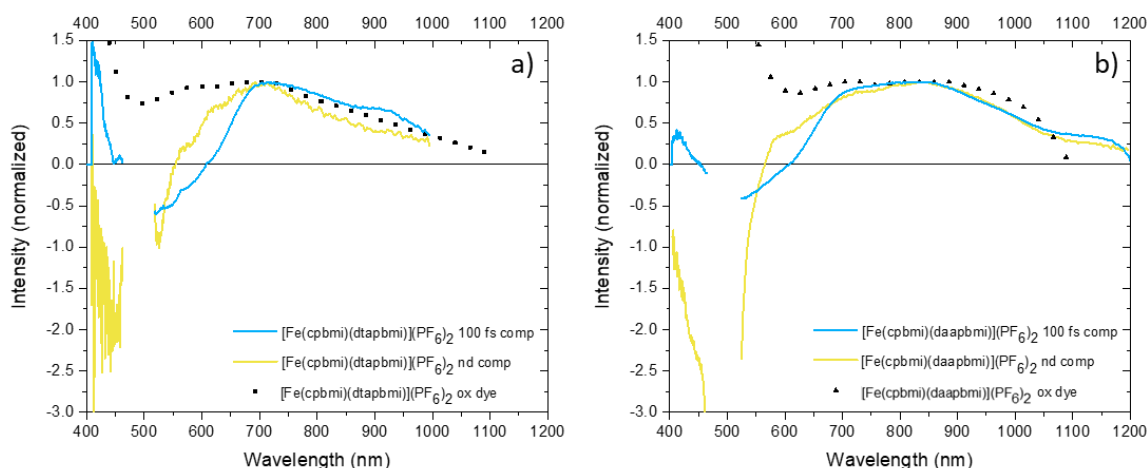


Figure S48. Decay associated spectra of the 100 fs component and the non-decaying component (normalized at respective maximum) from global fits of a) [Fe(cpbbi)(dtapbbi)](PF₆)₂ (excitation wavelength 490 nm) and b) [Fe(cpbbi)(daapbbi)](PF₆)₂ (excitation wavelength 480 nm) adsorbed on TiO₂ films in acetonitrile. All spectra have been cut to remove excitation scatter, as well as chirp (group velocity dispersion) and background corrected. Also included are spectra of the oxidized dyes obtained from spectroelectrochemistry, scaled for comparability.

As a proof that oxidized dye kinetics indeed can be tracked in the wavelength region around 900 nm, selected spectra at ultrafast times are shown in Figure S49 for the complexes [Fe(cpbbi)(dtapbbi)](PF₆)₂ and [Fe(cpbbi)(daapbbi)](PF₆)₂ adsorbed on reference Al₂O₃ films in acetonitrile. Here all positive spectral features must correspond to ESA since injection is not energetically feasible, and these features do not extend to a large extent into the wavelength range around 900 nm. Also shown is the dynamics of the samples that can be readily described by a single-exponential

decay function of lifetime 17-18 ps. The Al_2O_3 film introduces a significant amount of scattering into the data, which explains why a modelling of the background is used in the fit as well as no further significant components were found.

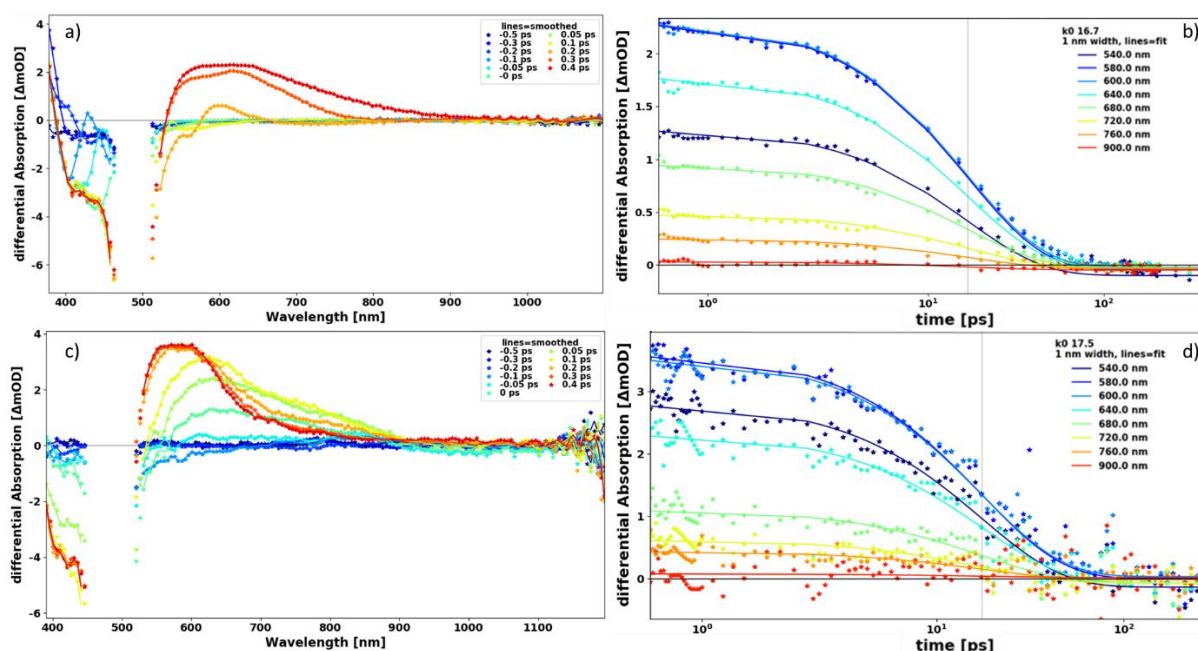


Figure S49. Early TA spectra of a) $[\text{Fe}(\text{cpbmi})(\text{dtapbmi})](\text{PF}_6)_2$ (excitation wavelength 490 nm) and c) $[\text{Fe}(\text{cpbmi})(\text{daapbmi})](\text{PF}_6)_2$ (excitation wavelength 480 nm) adsorbed on Al_2O_3 mesoporous films in acetonitrile. All spectra have been cut to remove excitation scatter, as well as chirp (group velocity dispersion) and background corrected. The shape of the excited state absorption band (~550-800 nm) should be compared with the positive TA signal in Figure S50. TA kinetics are plotted at selected wavelengths of b) $[\text{Fe}(\text{cpbmi})(\text{dtapbmi})](\text{PF}_6)_2$ and d) $[\text{Fe}(\text{cpbmi})(\text{daapbmi})](\text{PF}_6)_2$ adsorbed on Al_2O_3 mesoporous films in acetonitrile. The kinetics were fitted from 0.5 ps to 10 ns with a single-exponential fit however also including a modelling of the background since the Al_2O_3 films create a lot of scattering resulting in noisy data. Symbols represent the measured data and solid lines are the fits from global analysis.

In Figure S50 selected TA spectra at ultrafast times are plotted for the two complexes on TiO_2 in acetonitrile. Unfortunately the timesteps in a) are not as fine as in b) where the clear evolution of the oxidized dye signal around 800-1100 nm and the ESA feature around 600 nm can be seen. This evolution visualizes the process of ultrafast recombination already at the sub-ps timescale. The intersystem crossing from $^1\text{MLCT}$ to $^3\text{MLCT}$ competes with the injection, both are processes not resolved in our experiment. At ~0.5 ps in the timescale shown here the TA spectra have turned mainly into the feature of ESA from the $^3\text{MLCT}$ state and GSB.

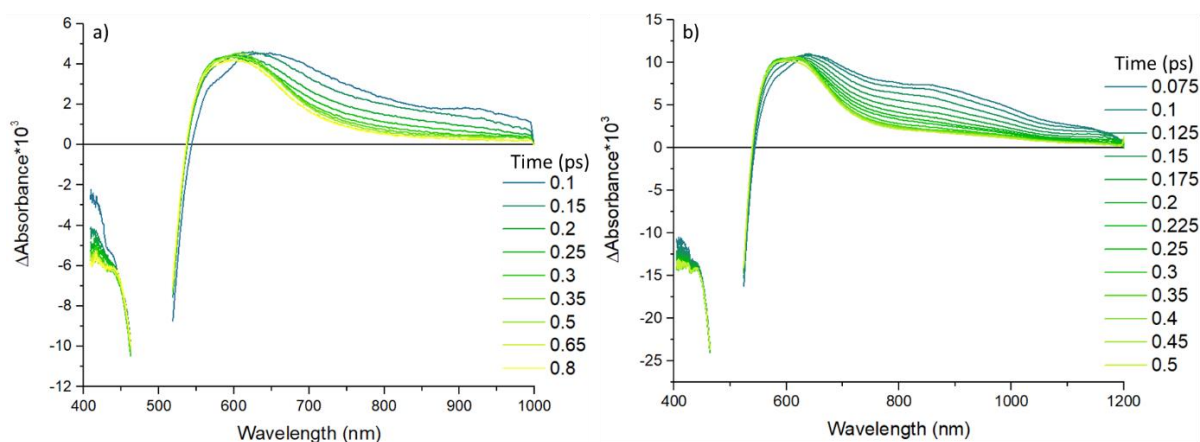


Figure S50. Early TA spectra of a) $[\text{Fe}(\text{cpbmi})(\text{dtapbmi})](\text{PF}_6)_2$ (excitation wavelength 490 nm) and b) $[\text{Fe}(\text{cpbmi})(\text{daapbmi})](\text{PF}_6)_2$ (excitation wavelength 480 nm) adsorbed on TiO_2 mesoporous films in acetonitrile. All spectra have been cut to remove excitation scatter, as well as chirp (group velocity dispersion) and background corrected. Here, the ultrafast evolution of the oxidized dye component (~800-1100 nm) as well as ESA (~550-800

nm) can be seen. The positive TA signal found here should be compared with the excited state absorption band (~550-800 nm) in Figure S49.

As a compliment to the earlier plotted kinetics, kinetics from the ESA and oxidized dye regions are plotted for a closer comparison of the >1 ps timescale. By shifting the signal at 300 ps to zero and then normalizing, it is possible to compare the decay of different spectral features. If the data is fitted globally, the modelling is dominated by the dynamics of the ESA at 600nm, which results in an insufficient description of several regions and un-physical confidence intervals of the parameters. Figure S51 are showing this fit for a) [Fe(cpbmi)(dtapbmi)](PF₆)₂ and b) [Fe(cpbmi)(daapbmi)](PF₆)₂. During the fit a 95% confidence interval is calculated for each parameter separately and shown for the 900 nm kinetic plots. A better modelling can be achieved if the 600nm and 900nm regions are fitted independently with two exponential decays. The results are presented in Figure S51 c) and d). During the analysis the confidence intervals for both parameters were estimated and a kinetic based on the extremes of the intervals calculated. In Table S12 the best fitting parameters from this type of fitting as well as the 95% confidence interval borders of the same parameters are given. Note that for [Fe(cpbmi)(daapbmi)](PF₆)₂ there is a significant and non-overlapping difference for the dominating of the two components (k1) in each spectral region. Again for each of the modelling the 95% confidence interval borders are given and plotted. From this difference can be concluded that the dynamics at 900nm are significantly different from the dynamics at 600 nm, and that one or multiple additional processes have to be assumed. For [Fe(cpbmi)(dtapbmi)](PF₆)₂ the signal to noise is worse but follow the same trend, suggesting in analogy with [Fe(cpbmi)(daapbmi)](PF₆)₂ one or multiple additional processes.

Figure S51. TA kinetics with fits and confidence intervals (in Table S12) from >1 ps of a) and c) [Fe(cpbmi)(dtapbmi)](PF₆)₂ and b) and d) [Fe(cpbmi)(daapbmi)](PF₆)₂ on TiO₂ in acetonitrile where the decay between ESA (600 nm) and oxidized dye (900 nm) spectral regions are compared. The kinetics have been moved to 0 at long times and were then normalized. Also included is the 95 % confidence intervals of the fits. Note the significantly better representation of the data in images by the separated models in c) and d) and the non-overlapping bands of kinetics. The confidence intervals for the 600 nm bands were omitted for clarity.

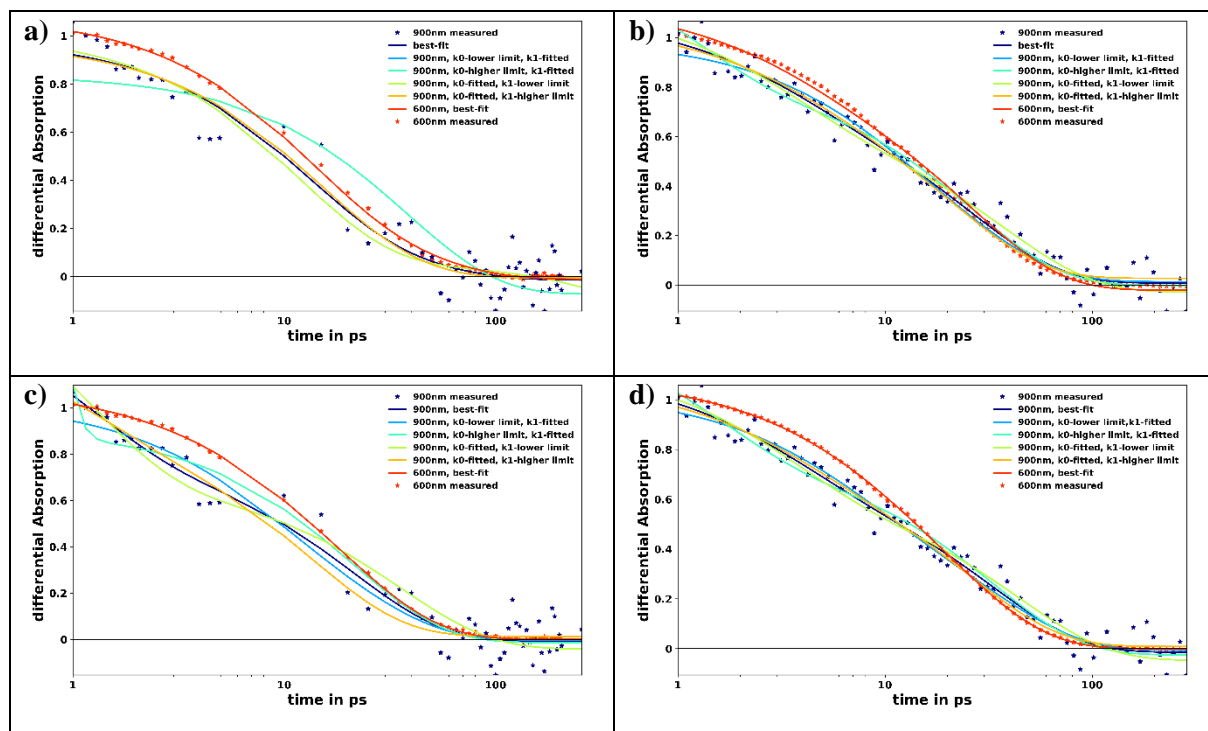


Table S12. Fitting of TA data of $[\text{Fe}(\text{cpbmi})(\text{dtapbmi})](\text{PF}_6)_2$ and $[\text{Fe}(\text{cpbmi})(\text{daapbmi})](\text{PF}_6)_2$ on TiO_2 films in acetonitrile in regions around 600 nm and 900 nm. The 95 % confidence interval for each fitting parameter is given in parenthesis.

$[\text{Fe}(\text{cpbmi})(\text{dtapbmi})](\text{PF}_6)_2$	600 nm	900 nm
k0	5 (2-11) ps	1.1 (0.1-6) ps
k1	20 (19-23) ps	21 (14-35) ps
$[\text{Fe}(\text{cpbmi})(\text{daapbmi})](\text{PF}_6)_2$	600 nm	900 nm
k0	6 (5-7) ps	3 (2-6) ps
k1	23 (22-24) ps	33 (26-44) ps

To check for the possible influence of the Stark effect on the film datasets, caused by the electric field built up in the TiO_2 film from injection, Figure S52 compare the TA spectra at 1 ps with the steady state absorption. In the figure it is clear that the ground state bleach resemble the inverted steady state absorption (in the figure called bleach contribution), there is no sign of shifting. A well pronounced Stark effect would lead to TA spectra looking more like the derivatives with respect to energy of the steady state absorption.^[S13] The derivatives (also included in Figure S52 and scaled for clarity) do however not match the TA spectra and thus the Stark effect is only affecting the TA data to a negligible level.

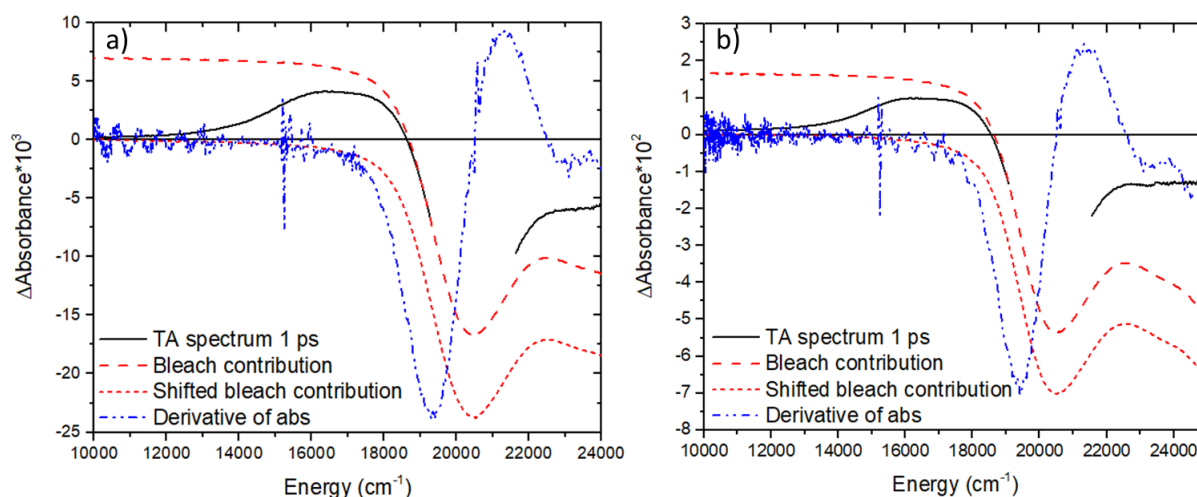


Figure S52. The inverted steady-state absorption spectra (called bleach contribution) and its derivative is here compared to the TA spectra at 1 ps after excitation of a) $[\text{Fe}(\text{cpbmi})(\text{dtapbmi})](\text{PF}_6)_2$ (excitation wavelength 490 nm) and b) $[\text{Fe}(\text{cpbmi})(\text{daapbmi})](\text{PF}_6)_2$ (excitation wavelength 480 nm) adsorbed on TiO_2 films in acetonitrile. The TiO_2 films used for both the steady-state and time resolved absorption measurements were fabricated by the same procedure, as outlined in section SI.8. The TA spectra have been cut to remove excitation scatter, as well as chirp (group velocity dispersion) and background corrected.

In this section we will argue why the dynamics of the TA film in acetonitrile data indeed arise from the processes they are assigned to and not due to side reactions. A side reaction could happen with either the excited or the oxidized state. As for the excited state, we can compare to the data on Al_2O_3 films in acetonitrile since the excited state is the same for the two cases. The characteristic fast TA dynamics on TiO_2 in acetonitrile are not observed on Al_2O_3 in acetonitrile which suggests that these dynamics should not be assigned to a side reaction with the excited state. The films of TiO_2 and Al_2O_3 are prepared in the same way (just using two different commercial pastes) so it is unrealistic that there are impurities causing side reactions present in one film and not the other. Furthermore, the ultrafast component in the TiO_2 in acetonitrile data does not lead to a ground state bleach recovery, as it should have done if this was a side reaction quenching the excited state.

Accepting the fact that the oxidized complex is formed ultrafast, the quenching of this state might not be recombination but side reactions. However for the oxidized dye to react with a contaminant on a 100 fs timescale is very unlikely. Such a fast rate requires direct contact of the quencher since diffusion is too slow. To realise this, the quencher needs to either have very high concentration (which should not be possible) or form a complex with the dye molecule already in the ground state (which was not observed as any change of the steady-state absorption). Both these options seem unlikely since ~10 % of the oxidized dyes are actually left for longer timescales, and none of the suggested side reaction conditions should lead to a discrimination of a small fraction of the complexes. Furthermore, a standard reducing quencher should return the oxidized dyes to ground state, which was not observed in the experiment.

Finally, any sign of degradation was ruled out by comparing the steady state absorption spectra of the films before and after TA measurement. In Figure S53 the steady-state absorption spectra of $[\text{Fe}(\text{cpbmi})(\text{dtapbmi})](\text{PF}_6)_2$ and $[\text{Fe}(\text{cpbmi})(\text{daapbmi})](\text{PF}_6)_2$ adsorbed on TiO_2 films are shown. These films were used in the half-cells (a way to keep the films in acetonitrile by encapsulating them with another glass slide, see section SI.8) investigated in TA spectroscopy. The spectrum on film is similar to the absorption spectrum of the deprotonated complex, see Figure S40. The steady-state absorption spectrum of the half cell with $[\text{Fe}(\text{cpbmi})(\text{dtapbmi})](\text{PF}_6)_2$ before and after TA are also compared in the figure. No differences between these two spectra suggests that no degradation happened during the experiment. The slight shift in the spectra between the sensitized film (in air) and the half cell (film in acetonitrile) is attributed to the fact that the added acetonitrile changes the environment of the complexes.

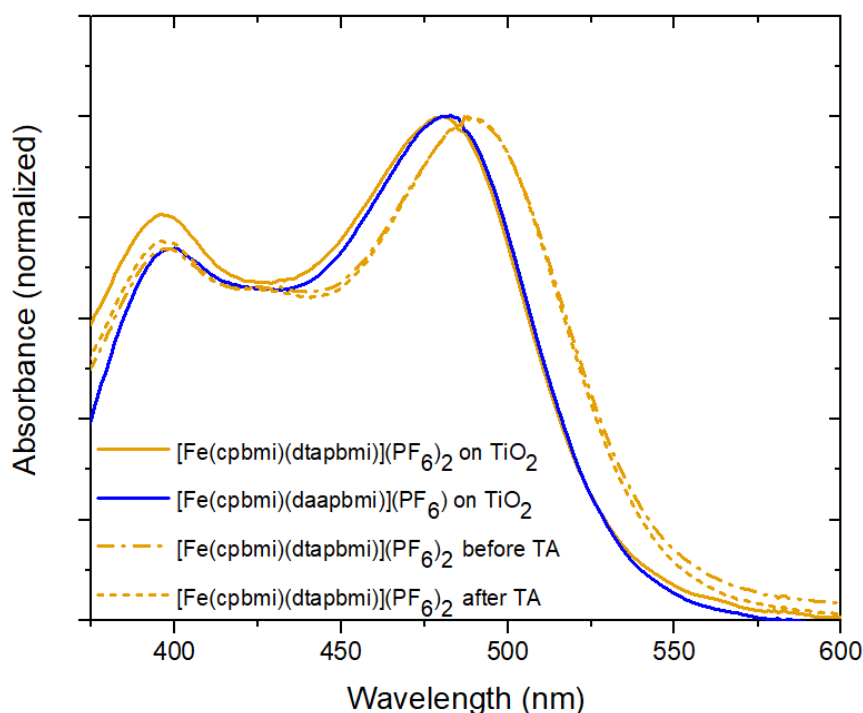


Figure S53. Steady-state absorption spectra of $[\text{Fe}(\text{cpbmi})(\text{dtapbmi})](\text{PF}_6)_2$ and $[\text{Fe}(\text{cpbmi})(\text{daapbmi})](\text{PF}_6)_2$ adsorbed on TiO_2 films. For one of the films the absorption of the half cell (a way to keep the films in acetonitrile by encapsulating them with another glass slide, see section SI.8) before and after TA measurement is shown. For fabrication of the samples, see section SI.8.

7. ns-Transient Absorption Spectroscopy

Nanosecond laser spectroscopy was performed using a frequency tripled Nd:YAG laser (Continuum Surelight II) combined with an OPO (Continuum Surelight) for excitation and an Edinburgh Instrument LP920 spectrometer. Laser pulses at 505 nm with ca. 2 mJ cm^{-2} per pulse were used for excitation. Continuous wave xenon white light filtered through 455 nm cut off filter was used as probe

light to record kinetic traces at 470 nm, which were averaged 480×. The inert electrolyte contained: 0.5 M NaClO₄ and 0.5 M 4-*tert*-butylpyridine (TBP) in acetonitrile. The iodide/triiodide redox electrolyte contained 0.5 M dimethylpropylimidazolium iodide, 0.1 LiClO₄, 0.05 M I₂, and 0.5 M TBP in acetonitrile.

In Figure S54 the regeneration and recombination dynamics of [Fe(cpbmi)(dtapbmi)](PF₆)₂ and [Fe(cpbmi)(daapbmi)](PF₆)₂ are plotted by comparing the transient absorption signal when an electrolyte was added to the film versus an inert electrolyte. Films for these measurements were prepared according to the procedure described in SI.8.

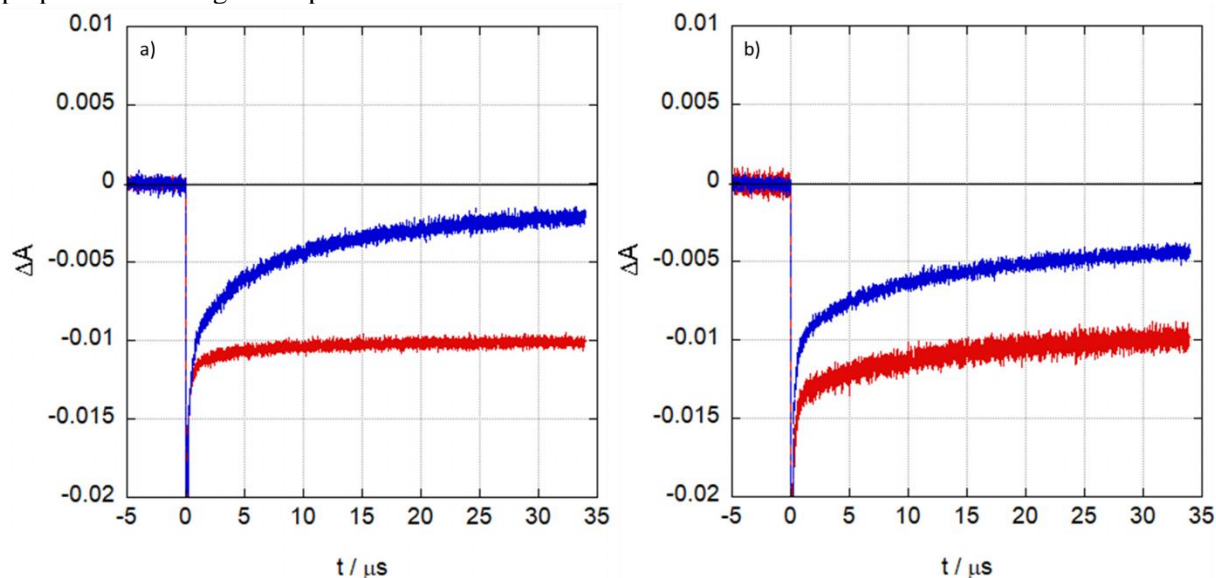


Figure S54. ns-transient absorption measurements of a) [Fe(cpbmi)(dtapbmi)](PF₆)₂ and b) [Fe(cpbmi)(daapbmi)](PF₆)₂ (excitation wavelength 505 nm) comparing the inert electrolyte dynamics (red) to the dynamics with iodide/triiodide electrolyte (blue). The inert electrolyte contained 0.5 M NaClO₄ and 0.5 M 4-*tert*-butylpyridine (TBP) in acetonitrile. The iodide/triiodide redox electrolyte contained 0.5 M dimethylpropylimidazolium iodide, 0.1 LiClO₄, 0.05 M I₂, and 0.5 M TBP in acetonitrile.

8. Half-Cell Fabrication

For transient absorption spectroscopy measurements, “half-cells” consisting of a glass slide with either sensitized TiO₂ or Al₂O₃ film encapsulated with another glass slide and acetonitrile inbetween, were fabricated in-house. The TiO₂ paste (Solaronix Ti-Nanoxide) or Al₂O₃ paste (Solaronix Al-Nanoxide) was doctor-bladed on glass microscope slides (one scotch tape layer thick) and dried in air. Prepared slides were baked in the oven following the temperature sequency 10 min at 150 °C and then 30 min at 450 °C. After controlled cooling overnight to room temperature, the TiO₂ or Al₂O₃ films were immersed into a 0.1 mM sensitization bath of the dye in acetonitrile for at least 24 h at room temperature. Shortly before the measurement, films were removed from the bath, rinsed with acetonitrile several times and dried under a stream of nitrogen gas. A spacer of parafilm was placed on the sensitized film to allow filling with acetonitrile and encapsulating with a second glass slide. Before and after measurement the stability of the sample was tested by measuring steady-state absorption spectra.

9. Solar Cell Fabrication

Unless otherwise noted, chemicals were purchased from Sigma-Aldrich and used without further purification. Generally, the fabrication of solar cells followed procedures as described in previous reports.^[S14] On cleaned (Hellmanex III solution, water, ethanol, UV-ozone) Nippon sheet glass (Pilkington, St. Helens, UK), 8 Ω sheet resistance, a dense TiO₂ layer was deposited via spray pyrolysis at 450 ° C from a 0.2 M titanium diisopropoxide bis(acetylacetonate)solution in isopropanol. Subsequently, 7 mm diameter TiO₂ photoanodes were screen-printed (Seritec Services SA, Corseaux, Switzerland) from DSL 18 NR-T (Dyesol/GreatCellSolar, Queanbeyan, Australia) colloidal (18 nm) TiO₂ paste (32 μ m). The full mesoporous layer thickness was screen-printed as 6 consecutive layers, with an annealing step at 450 °C after each deposited layer. Subsequently, a scattering layer (Dyesol/GreatCellSolar WER2-O, 400 nm) was screen-printed onto of the mesoporous film (4 μ m), followed by gradual heating towards a 30 min sintering step at 450 ° C. The substrates were post-treated with a 40 mM aqueous TiCl₄ solution for 30 min at 70 ° C and then sintered again at 450 ° C for 30 min. After cooling, the titania films were immersed sequentially into two different solutions, each overnight. The first solution contained 0.2 mM of each sensitizer in acetonitrile, while the second contained 0.5 mM chenodeoxycholic acid in acetonitrile. Platinized counter electrodes were fabricated through dropcasting of a 5 mM solution of isopropilic H₂PtCl₆ onto predrilled TEC7 glass followed by 30 minutes of sintering at 400 ° C.^[S15] The redox electrolyte solution contained 0.1 M LiI, 0.05 M I₂ and 0.6 M 1,2-dimethyl-3-propylimidazolium iodide in 3-methoxypropionitrile as proposed in reference.^[S16] The tested Co(bpy)₃ redox electrolyte solution contained 0.22 M Co(II)(bpy)₃(PF₆)₂, 0.05 M Co(III)(bpy)₃(PF₆)₃, 0.2 M *tert*-butyl pyridine and 0.1 M Li(I)(bis(trifluoromethanesulfonyl)imide). The cells were assembled using a 60 μ m thermoplastic Surlyn frame (Meltonix, Solaronix, Switzerland) melted between the two electrodes with a heated press (DN-HM01, Dyename, Sweden). The electrolyte was vacuum-injected through a hole in the counter electrode which was then sealed with a thermoplastic film and a glass cover slip.

10. Solar Cell Characterisation

Current-Voltage measurements were carried out in ambient air under AM 1.5G illumination using a HelioSim-CL60 solar simulator (Voss electronics, Kirchheim-Heimstetten, Germany). An X2000 source meter (Ossila, Sheffield, UK) was used to assess solar cell performance (50 mV s⁻¹). After calibration with a certified silicon reference cell (Fraunhofer ISE, Munich, Germany), a mask was employed to confine the active solar cell area to 0.19625 cm².

IPCE spectra were recorded with an ASB-XE-175 xenon light source (10 mW cm⁻²) (Spectral Products, Putnam, CT, USA) and a CM110 monochromator (Spectral Products, Putnam, CT, USA). The photocurrent was measured with a U6 digital acquisition board (Lab Jack, Lakewood, CO, USA). The setup was calibrated with a certified silicon reference cell (Fraunhofer ISE, Munich, Germany). Photocurrents were integrated based on the spectral distribution of sunlight.^[S17]

Electron lifetimes were investigated with a 1 W white LED (Luxeon Star, Lethbridge, Canada). Kinetics in the solar cell were probed by applying square-wave modulations to the light intensity. The solar cell response was tracked by a digital acquisition board (National Instruments, Austin, Texas) and fitted with first-order kinetic models.

The dye desorption experiment was carried out using a standard protocol within the field.^[S18] Sensitized photoanodes were immersed in a 0.9 M solution of KOH in MeOH and allowed to react for 3 h before taking the UV-Vis spectrum (using a UV-1800 Shimadzu) of the resulting solution.

Hysteresis measurement of the best fabricated solar cell of all complexes are shown in Figure S55. Electron lifetime measurements of solar cells fabricated with all different complexes are shown in Figure S56.

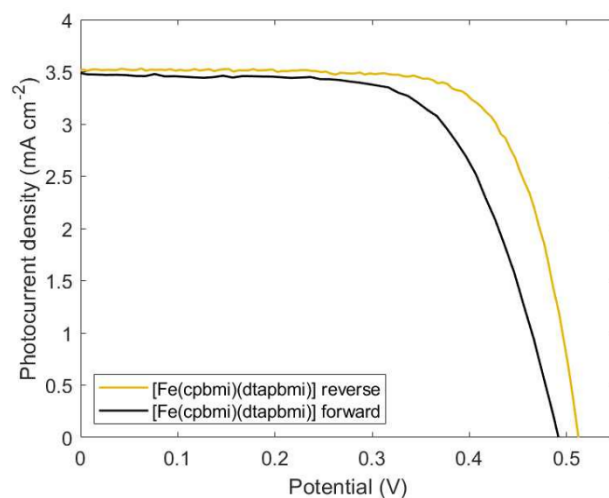


Figure S55. Hysteresis sweep of the champion solar cell with $[\text{Fe}(\text{cpbmi})(\text{dtapbmi})](\text{PF}_6)_2$ as sensitizer. This measurement was done following the outlined procedure above using AM1.5G illumination and a sweep rate of 50 mV s^{-1} .

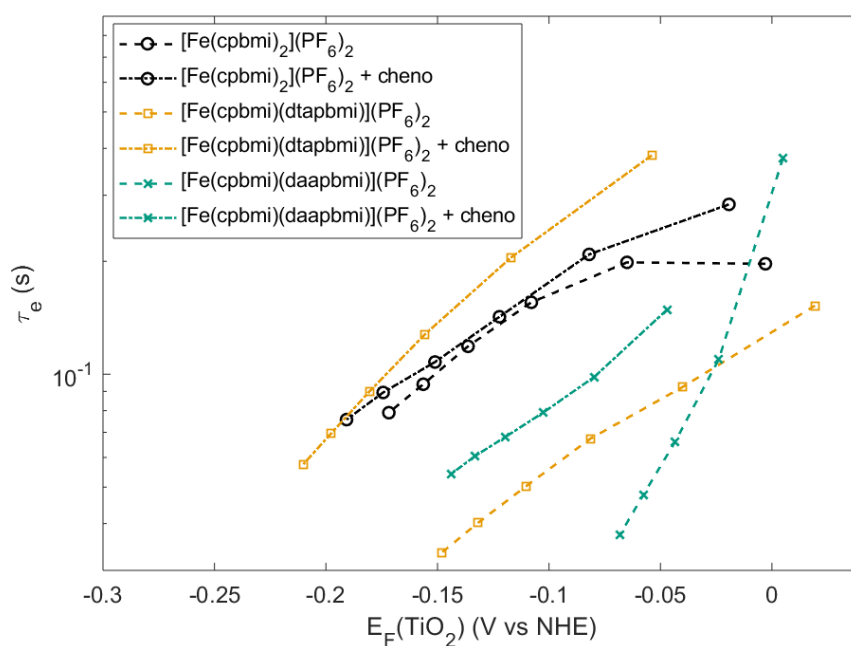


Figure S56. Electron lifetime measurements for solar cells fabricated with $[\text{Fe}(\text{cpbmi})_2](\text{PF}_6)_2$, $[\text{Fe}(\text{cpbmi})(\text{dtapbmi})](\text{PF}_6)_2$ and $[\text{Fe}(\text{cpbmi})(\text{daapbmi})](\text{PF}_6)_2$ as the sensitizers, with and without the co-sensitizer chenodeoxycholic acid, mixed into a 0.5 mM sensitizer bath as follows: 0.4 mM , 0.7 mM and 1 mM for $[\text{Fe}(\text{cpbmi})_2](\text{PF}_6)_2$, $[\text{Fe}(\text{cpbmi})(\text{dtapbmi})](\text{PF}_6)_2$, and $[\text{Fe}(\text{cpbmi})(\text{daapbmi})](\text{PF}_6)_2$ respectively.

Finally, further optimization of the solar cells with another redox mediation ($\text{Co}(\text{bpy})_3$) was attempted. This did however not yield better characteristics, which is seen in Figure S57 for sensitizer $[\text{Fe}(\text{cpbmi})_2](\text{PF}_6)_2$.

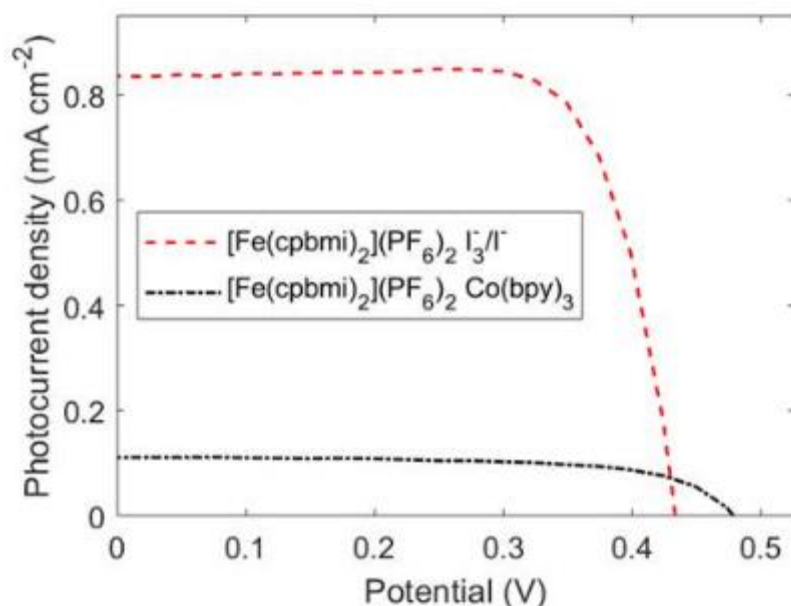


Figure S57. JV-scans comparing solar cells sensitized with $[\text{Fe}(\text{cpbmi})_2](\text{PF}_6)_2$, but with the electrolyte I_3^-/I^- or $\text{Co}(\text{bpy})_3$. This measurement was done following the outlined procedure above using AM1.5G illumination and a sweep rate of 50 mV s^{-1} .

References

- S1: T.C.B Harlang, Y. Liu, O. Gordivska, L.A. Fredin, C.S. Ponseca Jr, P. Huang, P. Chábera, K.S. Kjaer, H. Mateos, J. Uhlig, R. Lomoth, R. Wallenberg, S. Styring, P. Persson, V. Sundström, K. Wärnmark, *Nature Chemistry*, 2015, 7, 11, 883-889.
- S2: W.M. Haynes, *CRC Handbook in chemistry and Physics 97th ed.* 2016, CRC Press.
- S3: G. Sheldrick, *Acta Crystallogr. Sect. C: Cryst. Struct. Commun.*, 2015, 71, 3-8; (b) G. Sheldrick, *Acta Crystallogr., Sect. A: Found. Crystallogr.*, 2008, A64, 112-122.
- S4: O. V. Dolomanov, L. J. Bourhis, R. J. Gildea, J. A. K. Howard, H. Puschmann, *J. Appl. Crystallogr.* 2009, 42, 339-341.
- S5: C. F. Macrae, I. Sovago, S. J. Cottrell, P. T. A. Galek, P. McCabe, E. Pidcock, M. Platings, G. P. Shields, J. S. Stevens, M. Towler and P. A. Wood, *J. Appl. Cryst.* 2020, 53, 226-235.
- S6: Y. Liu, T. Harlang, S. E. Canton, P. Chabera, K. Suarez-Alcantara, A. Fleckhaus, D. A. Vithanage, E. Goransson, A. Corani, R. Lomoth, V. Sundström, K. Wärnmark, *Chem. Commun.*, 2013, 49, 6412-6414.
- S7: L. Liu, T. Duchanois, A. Monari, M. Beley, X. Assfeld, S. Haacke, P. Gros, *Phys. Chem. Chem. Phys.*, 2016, 18, 12550-12556.
- S8: M. Erdelyis, *J. Org. Chem.*, 2018, 83, 18, 10881–10886.
- S9: M.J. Frisch, G.W Trucks, H.B Schlegel, G.E Scuseria, M.A Robb, J.R Cheeseman, G. Scalmani, V. Barone, B. Mennucci, G.A Petersson, et al. Gaussian 09, revision C.01; Gaussian, Inc.: Wallingford, CT, 2009.
- S10: M. Reiher, O. Salomon, B. Artur Hess, *Theor. Chem. Accounts Theory, Comput. Model. (Theoretica Chim. Acta)* 2001, 107, 1, 48–55.
- S11: R. Krishnan, J.S Binkley, R. Seeger, J.A. Pople, *J. Chem. Phys.* 1980, 72, 1, 650–654.
- S12: A.D. McLean, G.S Chandler, *J. Chem. Phys.* 1980, 72, 10, 5639–5648.

S13: U.B. Cappel, S.M. Feldt, J. Schöneboom, A. Hagfeldt, G. Boschloo, *J. Am. Chem. Soc.*, 2010, 132, 9096-9101.

S14: H. Michaels, I. Benesperi, T. Edvinsson, A.B. Muñoz-Garcia, M. Pavone, G. Boschloo, M. Freitag, *Inorganics* 2018, 6, 53.

S15: S.M. Feldt, E.A. Gibson, G. Wang, G. Fabregat, G. Boschloo, A. Hagfeldt, *Polyhedron*, 2014, 82, 154-157.

S16: M. Karpacheva, C.E Housecroft, E.C Constable, *Beilstein J. Nanotechnol.* 2018, 9, 3069–3078.

S17: <http://rredc.nrel.gov/solar/spectra/am1.5/>, accessed 28 March 2018.

S18: P.J. Holliman, K.J. Al-Salihi, A. Connell, M.L. Davies, E.W. Jones, D.A. Worsley, *RSC Advances*, 2014, 4, 2515-2522.